الجمهورية الجزائرية الديمقراطية الشعبية
People's Democratic Republic of Algeria
وزارة التعليم العالي و البحث العلمي
Ministry of Higher Education and Scientific Research
جامعة عبد الحميد بن باديس – مستغانم
Abdelhamid Ibn Badis University – Mostaganem
كلية العلوم و التكنولوجيا
Faculty of Sciences and Technology

THÈSE DE DOCTORAT

TROISIEME CYCLE

Filière : Electronique

Spécialité : Electronique des Systèmes de Télécommunications

Laboratoire : Signaux et Systèmes (LSS)

Thème

Readability enhancement of time-frequency distributions based on kernels with compact support by image processing of TF diagrams: Application to feature extraction and signal classification

Présentée par

ADOUL Mohammed Amin

Master en Systèmes des Télécommunications, Département de Génie Electrique, UMAB

Soutenue publiquement le ..... **devant le jury :**

Président :	YAGOUBI Benabdellah	Professeur	Université de Mostaganem (UMAB)
	DAHMANI Mohamed	Professeur	USTO, Oran
Examinateurs :	MERAH Mostefa	Professeur	Université de Mostaganem (UMAB)
	OULD ALI Abdelaziz	MCA	Université de Mostaganem (UMAB)
Encadrant :	ABED Mansour	MCA	Université de Mostaganem (UMAB)

Année universitaire 2022/2023

UNIVERSITY ABDEL HAMID IBN BADIS OF MOSTAGANEM

DOCTORAL THESIS

Readability enhancement of time-frequency distributions based on kernels with compact support by image processing of TF diagrams: Application to feature extraction and signal classification

Author:
Mohammed Amin ADOUL

Supervisor:
Dr. Mansour ABED

in the

Electrical Engineering Department/LSS lab.

4 June 2023

Declaration of Authorship

I, Mohammed Amin ADOUL, declare that this thesis titled, "Readability enhancement of time-frequency distributions based on kernels with compact support by image processing of TF diagrams: Application to feature extraction and signal classification" and the work presented in it are my own. I confirm that:

- This work was done wholly or mainly while in candidature for a research degree at this University.
- Where any part of this thesis has previously been submitted for a degree or any other qualification at this University or any other institution, this has been clearly stated.
- Where I have quoted from the work of others, the source is always given. With the exception of such quotations, this thesis is entirely my own work.

"All praise and thanks are due to Allah. "

UNIVERSITY ABDEL HAMID IBN BADIS OF MOSTAGANEM

Abstract

Faculty of sciences and technology
Electrical Engineering Department/LSS lab.

PhD

Readability enhancement of time-frequency distributions based on kernels with compact support by image processing of TF diagrams: Application to feature extraction and signal classification

by Mohammed Amin ADOUL

Time-frequency distributions (TFDs) based on time-lag kernels with compact support (KCS) have proved their high performance in terms of resolution and crossterms suppression. However, as for all kernel-based quadratic TFDs, these distributions suffer from spreading out signal terms. This is due to the unavoidable smoothing effects of the kernel in the ambiguity domain. The main objective of this manuscript is to improve concentration, interference rejection and so time-frequency readability of this representation class. The latter has the advantage of being tuned using a single parameter while external windows are no longer needed. The KCS-TFDs, referred to as KCSDs, are first optimized using objective performance measures used in the literature. Important signal features are extracted as well through analysis of time slice plots. The obtained TF diagrams are then enhanced using a specific method that includes two-dimensional Wiener filter, automatic binarization and morphological image processing techniques. The enhanced plots are compared to those obtained from the original TFDs using several tests on real-life and multicomponent frequency modulated (FM) signals including the noise effects. Moreover, a comparative study involving a selection of the best-performing reassignment time-frequency distributions is provided. The obtained results show a significant improvement of concentration, time-frequency localization of the autoterms as well as interference and noise suppression. As viable applications, the proposed approach is used first to instantaneous frequency (IF) estimation of several synthetic and real-life M-ary frequency shift keying (MFSK) signals. It is shown that the IF estimator from the enhanced plots performs better than smoothed pseudo Wigner-Ville distribution (SPWVD) and reassignment post-processing-based TFDs in terms of mainlobe width (MLW) and variance, respectively, even at low signal-to-noise ratio (SNR). On the other hand, time-frequency characterization of continuous wave linear frequency modulation (CW-LFM) and pulse linear FM (PLFM) radar signals are also investigated.

الملخص

لقد أثبتت توزيعات الزمن-التردد المشتقة من الأنوية ذات الامتداد المحدود أداءها العالي من حيث التمركز الجيد للمكونات الخاصة بالإشارة و الإزالة الفعالة للعناصر المتداخلة. لكن، كما هو الحال بالنسبة لجميع التوزيعات التربيعية المولدة باستخدام أنوية، فإن هذه الأخيرة تعاني من توسع لمجال امتداد العناصر المكونة للإشارة في الزمن و التردد معا مما ينتج عنه أخطاء في تحديد بداية و نهاية كل حدث ترددي و ما يتبعه من استخراج غير دقيق للترددات اللحظية المميزة للإشارة قيد التحليل. يرجع ذلك في الأساس إلى التأثيرات غير المرغوب فيها والتي لا يمكن تفاديها لعملية التنعيم التي تقوم بها الدالة النواة في مجال الغموض.

تهدف هذه الأطروحة إذن إلى تحسين تمركز المكونات الخالصة للإشارة و إزالة التداخل بينها و بالتالي تحسين مقروئية مخططات الزمن-التردد لهذه الفئة الخاصة من التوزيعات التي تتميز بإمكانية تعديلها من خلال ضبط عنصر متغير وحيد و دونما حاجة إلى نوافذ خارجية إضافية. في بداية المعالجة، كان من الضروري تحسين توزيعات KCS-TFDs ، المشار إليها باسم KCSDs ، باستخدام مقاييس الأداء الموضوعية الأكثر فعالية في الأبحاث المنشورة في أدبيات الاختصاص. بالموازاة مع ذلك، يتم استخراج ميزات الإشارة المهمة أيضا من خلال تحليل المخططات الزمنية لأجل قيمة تردد معلوم. إثر ذلك، نقوم بتحسين مخططات الزمن-التردد التي تم الحصول عليها باستخدام طريقة معالجة صورة مبتكرة تتضمن مرشح وينر Wiener-Filter- ثنائي الأبعاد ، تحويل الصورة إلى صورة ثنائية تأخذ القيمتين ٠ أو ١، متبوعين بتقنيات مورفولوجية محددة للحصول أخيرا على القناع الأمثل الذي يحفظ خصائص الإشارة المعالجة بينما يحذف و يمسح المكونات المتداخلة و يحد من تأثير الضوضاء حتى عندما تكون طاقتها أكبر من طاقة الإشارة المفيدة. تظهر النتائج التي تم التحصل عليها تحسنا ملحوظا في تمركز العناصر الفعلية للإشارة و في تحديد أفضل و أدق لتموقع هذه المكونات في مجال الزمن-التردد بالإضافة إلى إزالة أفضل و أكثر فعالية للتداخل و الضوضاء. فيما يتعلق بالتطبيقات العملية للطريقة المقترحة، تم تقدير التردد الآني للإشارات الرقمية المستعملة في مجال الاتصالات من نوع MFSK كما تم فحص و استنباط خصائص التردد-الزمن لمجموعة من إشارات الرادار ذات التردد الخطي للموجة المستمرة (CW-LFM) وإشارات الرادار الخطية النبضية (PLFM).

Résumé

Les distributions temps-fréquence (TFDs) à base de noyaux à support compact (KCS) ont prouvé leurs hautes performances en termes de résolution et de suppression des termes croisés. Cependant, comme pour tous les distributions quadratiques basés sur le noyau, ces distributions souffrent de l'étalement des termes de signal. Cela est dû aux inévitables effets de lissage du noyau dans le domaine de l'ambiguïté. L'objectif principal de ce manuscrit est d'améliorer la concentration, le rejet des interférences et donc la lisibilité temps-fréquence de cette classe de représentation. Ce dernier a l'avantage d'être réglé à l'aide d'un seul paramètre alors que les fenêtres externes ne sont plus nécessaires. Les KCS-TFDs sont d'abord optimisés à l'aide de mesures de performance objectives utilisées dans la littérature. Les caractéristiques importantes du signal sont également extraites grâce à l'analyse des tracés de tranches de temps. Les diagrammes TF obtenus sont ensuite améliorés à l'aide d'une méthode spécifique qui comprend un filtre de Wiener bidimensionnel, une binarisation automatique et des techniques de traitement d'images morphologiques. Les tracés améliorés sont comparés à ceux obtenus à partir des TFD d'origine à l'aide de plusieurs tests sur des signaux modulés en fréquence (FM) réels et multicomposants, y compris les effets de bruit. Par ailleurs, une étude comparative portant sur une sélection de les distributions temps-fréquence de réaffectation les plus performantes sont fournies. Les résultats obtenus montrent une amélioration significative de la concentration, de la localisation temps-fréquence des autotermes ainsi que de la suppression des interférences et du bruit. En tant qu'applications viables, l'approche proposée est d'abord utilisée pour l'estimation de fréquence instantanée (IF) de plusieurs signaux synthétiques et réels de modulation par déplacement de fréquence (MFSK). Il est démontré que l'estimateur IF des parcelles améliorées fonctionne mieux que la pseudo-distribution de Wigner-Ville lissée (SPWVD) et les distribution basée sur le post-traitement RTFDs en termes de largeur de lobe principal (MLW) et de variance, respectivement, même à faible rapport signal sur bruit (SNR). D'autre part, la caractérisation temps-fréquence des signaux radar à modulation de fréquence linéaire à onde continue (CW-LFM) et FM linéaire à impulsions (PLFM) est aussi étudiée.

Acknowledgements

We must thank Allah Almighty for all the will and courage He has given us to complete this work. I would like also to take this chance to express my gratitude to the people who helped me in my pursuit of a PhD degree.

A big thanks to my mother for her love, especially for her incessant prayers, her advice, and her unconditional support, both moral and economic, which allowed me to carry out the studies that I wanted and consequently this thesis.

I dedicate this work to my father. Praying ALLAH Almighty to have mercy on his soul and welcome him in his vast paradise. Amin!

I would also like to thank the President and the members of the jury who have done me the honor of carefully studying our work and who have deigned to sit for the defense of our thesis.

I would like to thank my supervisor, Dr. Mansour ABED, for his immeasurable advice, patience, and support throughout my Ph.D. as well as my graduation.

I would also like to thank my colleagues from the research team at the LSS laboratory for their help, support, and kindness.

I also wish to express my sincere gratitude to my family and friends who were patient and supportive throughout my life.

Contents

List of Figures

List of Tables

List of Abbreviations

TFSA	Time-frequency signal analysis
STFT	Short-time Fourier transform
WVD	Wigner–Ville distribution
TFD	Time-frequency distribution
QTFDs	Quadratic time-frequency distributions
KCS	Kernels with compact support
CB	Cheriet-Belouchrani
SCB	Separable Cheriet-Belouchrani
PCB	Polynomial Cheriet-Belouchrani
CBD	Cheriet-Belouchrani distribution
SCBD	Separable Cheriet-Belouchrani distribution
PCBD	Polynomial Cheriet-Belouchrani distribution
HT	Hilbert transform
FT	Fourier transform
2D	Two-dimensional
TFRs	Time-frequency representations
FMCW	Frequency-modulated continuous wave
SP	Spectrogram
WT	Wavelet transform
CWT	Continuous WT
DWT	Discrete WT
PWVD	Pseudo Wigner Ville distribution
SPWVD	Smoothed Pseudo Wigner Ville distribution
PMHD	Pseudo Margenau-Hill distribution
PD	Page distribution
PPD	Pseudo Page distribution
CWD	Choi–Williams distribution
BD	B-distribution
MBD	Modified B-distribution
EMBD	Extended Modified B-distribution
CKs	Compact kernels
CKD	Compact kernel distribution
T-F	Time-frequency
RSP	Reassigned spectrogram
RTFR	Reassigned Time-frequency representation
LFMs	Linear frequency modulations
IF	Instantaneous frequency

SST	Synchrosqueezing transform
WSST	Wavelet-based Synchrosqueezing transform
FSST	STFT-based Synchrosqueezing transform
RSD	Reassignment Stankovic distribution
RPWVD	Reassignment PWVD
RSPWVD	Reassignment SPWVD
RPPD	Reassignment PPD
RPMHD	Reassignment PMHD
MFSK	M-ary frequency shift keying
MLW	Mainlobe width
SKCS	Separable kernel with compact support
RN	Ratio of norms
RNSE	Rényi entropy normalized by signal energy
RNDV	Rényi entropy normalized by distribution volume
CM	Concentration measure
S	Stankovic measure
NIR	Normalized instantaneous resolution
RM	Reinhold measure
OKCSDs	Optimized KCS-TFDs
RTFDI	Resized TFD image
GTFDI	Grayscale TFD image
EKCSDs	Enhanced kernels with compact support distributions
ECBD	Enhanced Cheriet-Belouchrani distribution
ESCBD	Enhanced separable Cheriet-Belouchrani distribution
EPCBD	Enhanced polynomial Cheriet-Belouchrani distribution
AWGN	Additive white Gaussian noise
SNR	Signal-to-noise ratio
PW-WVD	Piece-wise spline Wigner-Ville distribution
LFM	Linear frequency modulated
MC	Monte Carlo
MSE	Mean-square error
CW-LFM	Continuous wave linear frequency modulation
PLFM	Pulse linear FM
FHSS	Frequency-hopping spread spectrum

Chapter 1

Introduction

Radar signal processing, underwater acoustics, biomedicine, oceanography, and seismology are only some of the possible interest fields for measurements of signals with time-varying spectra. Non-stationary signals, i.e. those signals with time-varying frequency contents in both time and frequency. However, in these fields, measuring the instantaneous characteristics of a particular non-stationary process is often an important task. Among all signal processing techniques, time-frequency signal analysis (TFSA) can reveal certain structures of signals that are not apparent in other techniques.

TFSA has been developed for non-stationary signals. In the literature, research on time-frequency has been divided into linear and nonlinear (or quadratic) methods. Linear representations are basically representations that satisfy linear properties of equations in statistical signal processing. The linear methods such as short-time Fourier transform (STFT), S-transform, wavelet transform, Gabor Representation, and so on, are easy to implement. However, due to the Heisenberg uncertainty principle, there is always a tradeoff between time and frequency resolutions. Besides the poor time-frequency localization, linear TFRs are recognized by their weak ability for noise elimination.

The nonlinear methods such as Wigner–Ville distribution (WVD) have received much attention because of their useful properties, as well as to its excellent concentration for mono-component signals. A monocomponent signal is described in the time-frequency domain by one single "ridge", corresponding to an elongated region of energy concentration. A multicomponent signal may be defined as the sum of two or more monocomponent signals. However, the presence of cross-terms in the basic is a classical problem when analyzing multi-component and/or nonlinear signals. Many other quadratic time-frequency distributions (QTFDs) have been developed, such that each QTFD can be written as a smoothed version of the WVD using a specific kernel filter. Kernels are designed as low-pass filters in the ambiguity domain to eliminate and suppress the cross-terms. The generalized kernel-based approach allows the definition of new distributions that are better adapted to particular signal types, using a simple procedure. However, the QTFDs represent the majority of traditional time-frequency TF methods used in practical applications that deal with non-stationary signals.

Recently, it was shown that kernels with compact support (KCS) derived from the Gaussian kernel allow the best tradeoff between a high cross-term rejection and a good auto-term resolution. The Gaussian kernel suffers from information loss due cut-off to compute the time-frequency distribution and the prohibitive processing time due to the mask's width which is increased to minimize the information loss. On the contrary, kernels with compact support are found to improve processing time and recover this information loss and at the same time retain the most important properties of the Gaussian kernel. Motivated by these interesting properties, three kernels with compact support derived from the Gaussian kernel are used for time-frequency analysis namely the Cheriet-Belouchrani (CB), the separable CB (SCB), and the polynomial CB (PCB). The induced distributions referred to as CB distribution (CBD), SCB distribution (SCBD), and PCB distribution (PCBD), respectively are generated following a specific method that uses first the Hilbert transform for producing analytical signals from real samples of the original signal. The use of the analytic associate rather than from the signal itself avoids spurious terms caused by interference between positive-frequency and negative-frequency components. However, then computes the convolutions of the proposed compact support kernels and the instantaneous autocorrelation functions and finally applies a Fourier transform to determine information related to the energy of the original signal with respect to time and frequency. These methods are devoted to suppressing the cross-terms and maintaining the concentration of the auto-terms from the Wigner-Ville distribution. To measure signal auto-term concentration and possibly automatically determine parameters for a TFR, objective performance measures are needed so that the performance of the generated distribution is optimized. In this manuscript, some often applied measures for quantifying the concentration and resolution are discussed. However, the KCS-based TFDs outperform other well-known classical distributions in terms of cross-term reduction while still achieving the best time-frequency resolution and then preserving high energy concentration around the components' instantaneous frequencies. Unfortunately, as all QTFDs, the KCS-based TFDs suffer from degradation in time-frequency localization. This is due to the smoothing effects of the Doppler-lag kernel that acts as a two-dimensional filter in the ambiguity domain.

Many proposed methods for readability enhancement of the TFRs are available today. Some of these are: reassignment method, synchrosqueezing transformation, multi-taper, high-order synchrosqueezing transform, s-method, time–frequency image de-blurring, and de-noising methods. These methods cannot be indifferently applied, owing to their specific fields of application, according to various utilization limits, such as time and frequency resolutions, noise levels, computing speed, original representations, and so on.

This justifies the need for new enhancement tools suitable for high-resolution TFDs such as the KCS-based TFDs. Otherwise, important signal

characteristics may be corrupted or become lost while the major challenge is to accurately estimate these characteristics whatever is the application: blind source separation, sound processing, telecommunications, seismic, interference rejection in spread spectrum communications systems, multicomponent target detection, and watermarking in multimedia, just to name a few. To address the readability enhancement issue, we propose a low-complexity post-processing that includes a 2D Wiener filter, automatic binarization, and morphological image processing techniques. The performances of KCS-based TFDs are significantly improved by the proposed method. The image post-processing is applied to the time-lag KCS distributions to overcome the smoothing effect of the compact support kernel in the ambiguity domain and eliminate interfering terms. The proposed method is used to generate the enhanced KCS-based distributions referred to as the ECBD, the ESCBD, and the EPCBD, respectively. The latter are compared to a selection best performing post-processing time-frequency analysis methods using performance evaluation measures. For practical application, the proposed method is used for the characteristics estimation of multicomponent nonstationary radar signals and radio communication HF signals embedded in noise.

In addition, the proposed enhancement of the time-lag compact support kernels provide four additional important advantages concerning optimization and implementation: 1) No external smoothing windows are needed to achieve high concentration and resolution in time or frequency since the kernel vanishes itself outside a compact set, 2) The proposed distributions are computed and their performance is optimized through the tuning of a single parameter that controls the kernel's bandwidth. In particular, the smoothing parameter of the PCB time-lag kernel is an integer, 3) The proposed enhancement post-processing method produces a sharper TF plot with low computational cost, and 4) No information about the analyzed signal is needed.

Chapter 2

Time-frequency signal analysis

2.1 Overview

In this chapter, theoretical background to time-frequency signal analysis is presented, and examples of basic and commonly used time-frequency representations (TFRs) are given. Due to the amount of literature published on the topic, only the most relevant work is described.

2.2 Signal analysis?

Engineering problems are analyzed and solved by asking relevant questions. It is quite common to find multiple plausible hypotheses to a problem when different questions are posed or when solutions are sought under different trains of thought. Signal analysis is no different, many transformations, methods, and generalizations have evolved to model the wide variety of signals that are encountered in various real-life problems such as communications, neurosciences, fault detection, radar, sonar, and acoustics. Signal analysis is the characterization and study of the basic properties of signals and was historically developed concurrently with the discovery of signals in nature such as the sound wave, electric voltages and currents. A signal is generally a function of many variables. For example, the electric field varies in both space and time. However, these models are used to retrieve a signal that undergoes dispersion, attenuation, and corruption with extraneous signals when it propagates through a canal.

2.3 Time domain

In the time domain signals are expressed as a function of time as illustrated in Figure 2.1. In general, when an analysis uses a unit of time such as seconds or one of its multiples (minutes or hours) as a unit of measurement then it is in the time domain. Time-domain methods work better for wideband signature studies, are provide better visual representations for understanding the field interactions, and better suited for parallel processing. For these reasons, most people are relatively comfortable with time-domain representations of

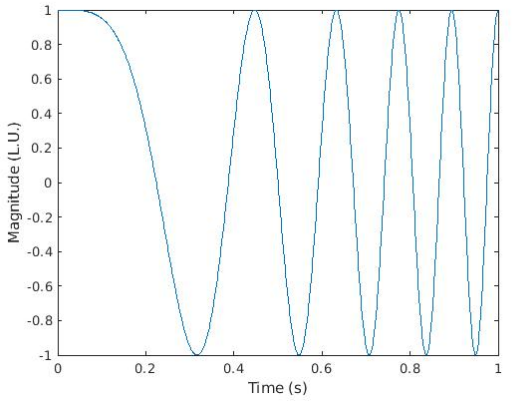

(a)

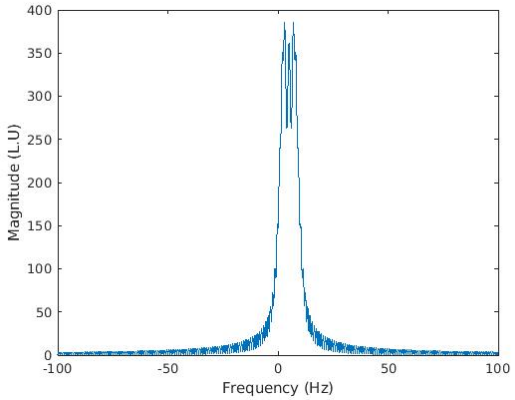

(b)

FIGURE 2.1: Frequency-modulated continuous wave radar (FMCW). (a) Time representation and (b) Frequency representation.

signals. However, the time-domain representation has limitations. It does not clearly show how the frequency varies with time. In other words, the time-domain representation tends to obscure information about frequency because it assumes that the two variables t and f are mutually exclusive.

2.4 Frequency domain: Fourier transform

Any practical signal can be represented in the frequency domain by its Fourier transform. The Fourier transformation occupies a privileged place in the signals theory and treatment. FT provides a representation easy to read and interpret, and to describe the content of a stationary signal without loss of information; we often talk about the spectrum of a signal to characterize it. The Fourier transform (FT) is complex; it magnitude is called the magnitude spectrum (Figure 2.1. Using fast Fourier transform). It shows

how the energy of the signal is distributed over the frequency domain.

The Fourier transform of a one-dimensional signal x(t) is given by [1]

$$X(f) = \int_{-\infty}^{\infty} x(t) e^{-i2\pi ft} dt \tag{2.1}$$

The inverse Fourier transform is a mathematical formula that converts a signal from the frequency domain f to one in the time domain t. It is given by [1]

$$x(t) = \int_{-\infty}^{\infty} X(f) e^{i2\pi ft} df \tag{2.2}$$

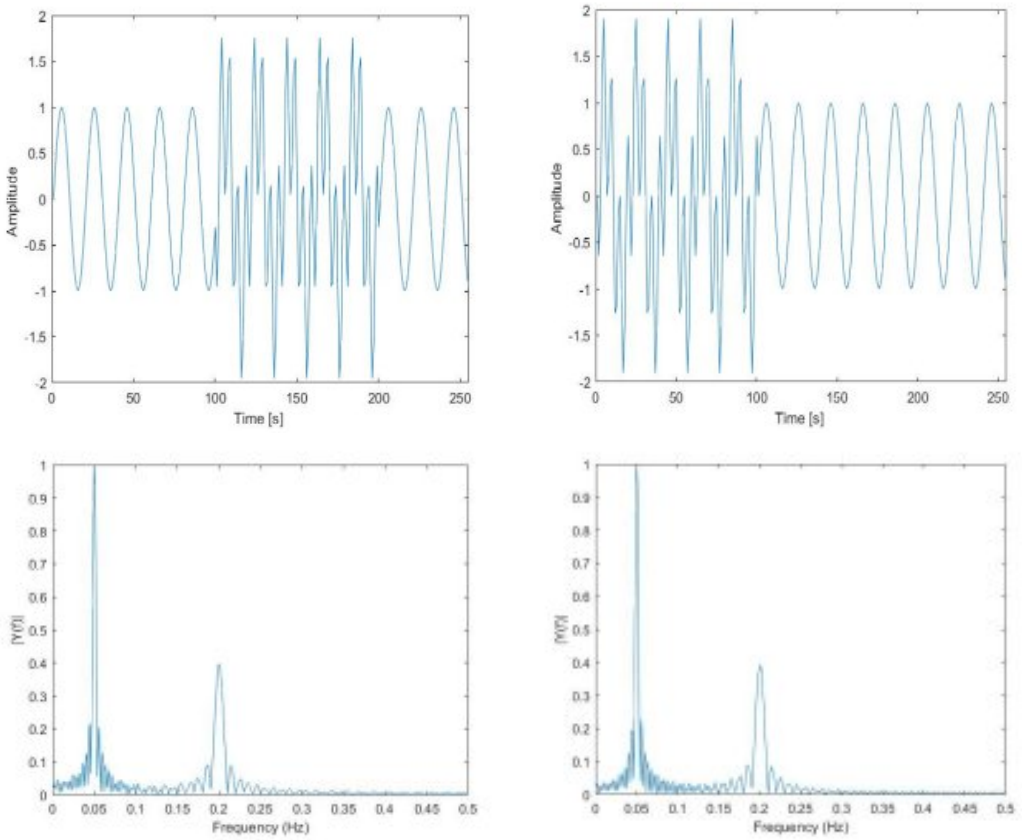

FIGURE 2.2: Time and frequency representations of two non-stationary signals. Time representations (top) and frequency representations (bottom).

Fourier analysis is a basic tool in signal processing, essential in many fields of research, but it quickly shows justified limits when one leaves the rigorous framework of its definition: the domain of stationary signals of finite energy. In Fourier analysis, all temporal aspects (beginning, end, and duration of an event), although present in the phase, become unreadable in the spectrum. If we want to know the spectral components of a signal using

the Fourier transformation, we then lose knowledge of the instantaneous occurrence of these components (Figure 2.2, two different signal have the same magnitude spectrum). This requires us to use other mixed time-frequency representations which make it possible to locate them or to locate these variations over time. A partial solution to this problem, the most intuitive, consists of the division of a nonstationary signal into a sequence of short-term Fourier transforms. A second solution, more satisfactory, consists in looking directly for a tool adapted to the study of non-stationary phenomena in the time-frequency representation.

2.5 Linear-based time-frequency representations

2.5.1 Short-time Fourier transform

The first solution, implemented intuitively in the middle of the century, corresponds to Fourier analysis with a sliding window or the short-time Fourier transform (STFT). The principle of the STFT is based on the application of a local Fourier spectral representation to segments of the signal sampled sequentially using a sliding window. The STFT of a signal x(t) can be given by the following equation [1]

$$STFT_x(t,f) = \int_{-\infty}^{\infty} x(\tau)h^*(\tau - t)e^{-i2\pi f\tau}d\tau \tag{2.3}$$

The spectrogram (Figure 2.3) being the square module of a short time Fourier transform, it represents the energy of the signal in time, according to the segment analyzed, and in frequency, according to the Fourier coefficient [1]

$$SP_x^h(t,f) = |STFT_x(t,f)|^2 = \left|\int_{-\infty}^{\infty} x(\tau)h^*(\tau - t)e^{-i2\pi f\tau}d\tau\right|^2 \tag{2.4}$$

A special case of the STFT is the Gabor transform (Figure 2.4). The latter is an STFT using a Gaussian window $h(t)$

$$h(t) = \left(\frac{\alpha}{\pi}\right)^{\frac{1}{4}} e^{-\frac{\alpha}{2}t^2} \tag{2.5}$$

The main drawback of STFT is its limited resolution. Indeed, it is impossible to have perfect localization both in time and frequency. In other words, the more support time of the sliding window is smaller the more the resolution in frequency is bad and conversely.

2.5.2 Wavelet transform

In 1982, Morlet opened the way leading to use wavelets transformations. This analysis, also called time-scale analysis, is used to detect phenomena

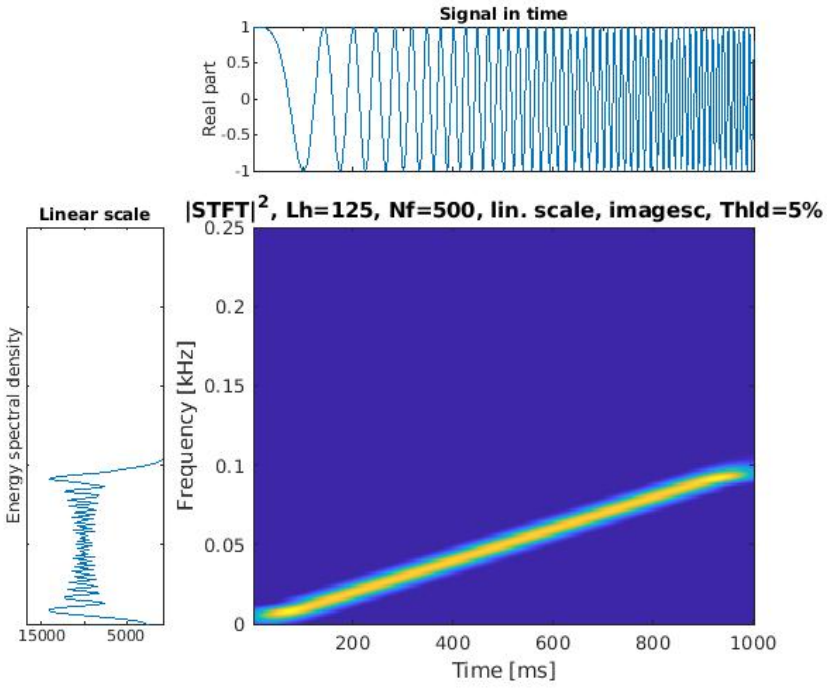

FIGURE 2.3: Spectrogram of FM signal.

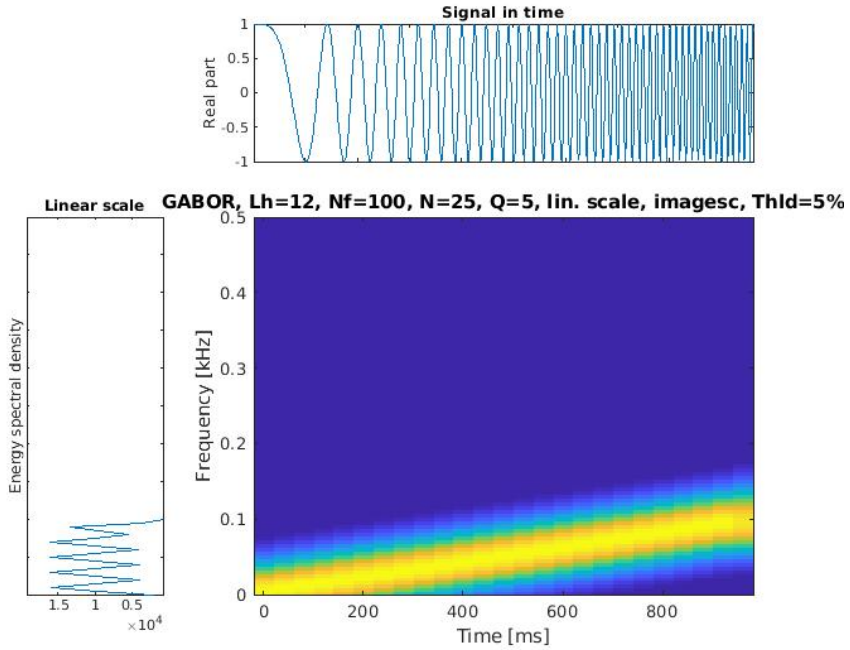

FIGURE 2.4: Gabor representation of FM signal.

that take place on different frequency scales encountered in a signal. The wavelet transform (WT) can be used to analyze signals in time-frequency space and retain the important components of the original signals. In the past 20 years, WT has become a very effective tool in signal and image processing. Figure 2.5 represent the scalogram (the squared modulus of the wavelet

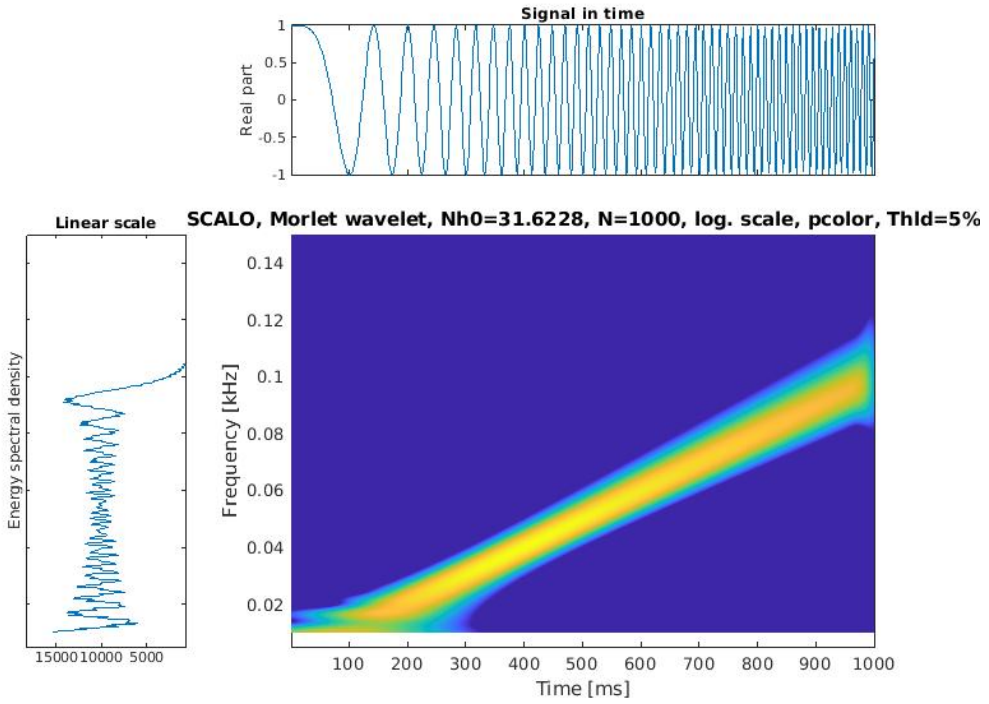

FIGURE 2.5: Scalogram of FM signal.

transform). Currently, WT is widely used in many practical applications. However, the fundamental idea of WT is to decompose the signal using analyzing functions, particularly ones constructed from an oscillating mother wavelet with zero mean [2, 3]. It is interpreted as a signal filtering process processed by a bandpass filter whose bandwidth is variable. His instantaneous response is not other than the analyzing wavelet for each scale, it is the scale factor "a" which fixes the filter bandwidth. WT is divided into continuous WT (CWT) and discrete WT (DWT). The continuous wavelet transform of a signal x(t) is defined by [4, 1]

$$CWT(b,a) = \int_{-\infty}^{+\infty} f(t)\psi_{(b,a)}(t)dt \tag{2.6}$$

and

$$\psi_{(a,b)}(t) = \frac{1}{\sqrt{a}}\psi * \left(\frac{t-b}{a}\right) \tag{2.7}$$

where a and b are the scales and time shifts of a reference wavelet ψ, respectively, $\psi*$ is the complex conjugate of the reference wavelet, t is time, and

$WT(a, b)$ is the time-scale representation of the signal.

The mother wavelet ψ indicates that the duration of function is very limited, hence the local characteristics of non-stationary signal can be accurately captured by wavelet analysis.

The main difference between the continuous wavelet system and the discrete wavelet system is that the dilation and translations parameters (b, a) for the CWT are varying over all of $RxR*$, and in the case of DWT, the dilation parameter a and the translation parameter b take only discrete values [5].

As the same for STFT, the continuous wavelet transform thus suffers from finite localization as well as reduced readability due to spectral smoothing [6, 7, 3].

2.6 Belinear-based time-frequency representation

2.6.1 Wigner-Ville distribution

A particularly interesting time-frequency energy distribution is the Wigner-Ville distribution (WVD) which provides a time-frequency representation without any restriction on the time and frequency resolutions. It is quite suitable for the analysis of non-stationary signals since it does not require any assumptions about the signal itself. The Wigner-Ville distribution of a continuous input signal $x(t)$ is defined by

$$W_x(t, f) = \int_{-\infty}^{\infty} x_a\left(t + \frac{\tau}{2}\right) x_a^*\left(t - \frac{\tau}{2}\right) e^{-i2\pi f\tau} d\tau. \tag{2.8}$$

where $x_a(t)$ is the analytic signal associated with the real signal $x(t)$ using the Hilbert transform. The purpose of the analytic signal is to consider the positive frequencies only in the representation.

For the linear chirp signal (see Figure 2.6), the mono-component complex-valued sinusoid and impulse, the WVD give exactly the instantaneous frequencies, i.e. perfectly localized time-frequency representations. For these kinds of signals, the time-frequency resolution of the WVD is unbeatable. Beside of its excellent concentration for mono-component signals, the Wigner–Ville distribution (WVD) has received much attention because of its mathematical properties. However, the presence of cross-terms (as we can see in Figure 2.7) in the WVD is a classical problem when analyzing multi-component and/or nonlinear signals. Many others quadratic time-frequency distributions (QTFDs) have been developed, such that each QTFD can be written as a smoothed version of the WVD using a specific kernel filter [1].

2.6.2 Pseudo Wigner-Ville distribution

The Wigner-Ville distribution can be improved by filtering. Pseudo Wigner-Ville distribution (PWVD) is nothing else but a frequency filtered WVD. The

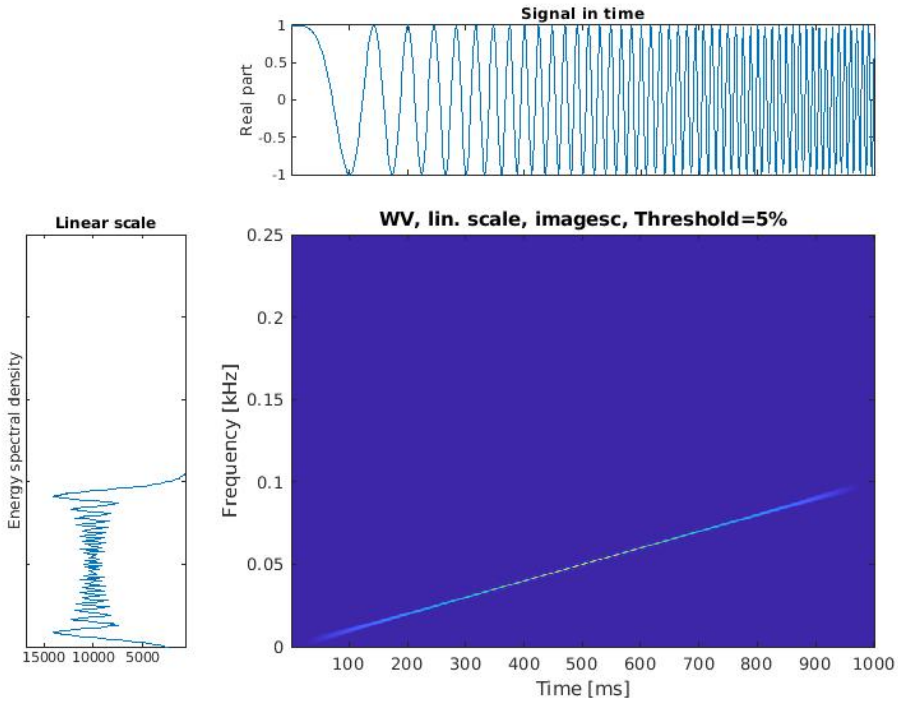

FIGURE 2.6: WVD of FM signal.

distribution was thus obtained while keeping the spirit of the Wigner-Ville distribution. Is an analysis through a short-term sliding window with a fixed and a finite duration, which makes it a close neighbor of the spectrogram. However, the PWVD is a prominent member of the class quadratic time–frequency representations [8]. It satisfies a large number of desirable mathematical properties, such as high resolution, and the time–frequency marginal property.

The pseudo Wigner-Ville distribution is given by [8, 1]

$$PWVD_x(t,f) = \int_{-\infty}^{+\infty} h(\tau) x_a\left(t+\frac{\tau}{2}\right) x_a^*\left(t-\frac{\tau}{2}\right) e^{-j2\pi f\tau} \mathrm{d}\tau \qquad (2.9)$$

Nevertheless, the quadratic nature of the pseudo-Wigner–Ville distribution also produces a great number of spurious values (cross-terms) between the auto-terms (see Figure 2.8) when it is applied over multiple-component signals [8]. These interference's are called inter-cross-terms that restrict the application fields of the PWVD in valid analysis, interpretation, and parameters extraction from signals. Thus, suppressing cross-terms and improving the PWVD is always an active domain of time–frequency analysis.

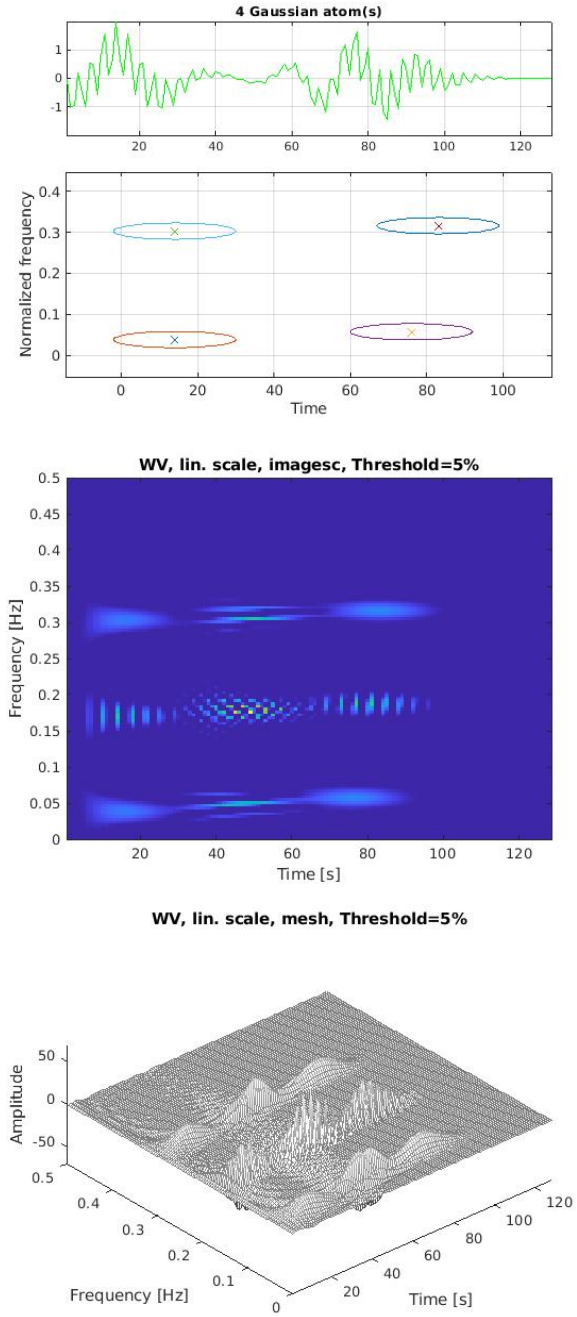

FIGURE 2.7: Sum of four atoms signal. From top to bottom are: Time representation, ideal T-F, WVD (2D plot), and WVD (mesh plot).

2.6.3 Smooth-pseudo Wigner-Ville distribution

Though the PWVD successfully removes the intra-cross-terms, it fails to remove the inter-cross-terms. To overcome this limitation, another method called smoothed pseudo-WVD (SPWVD) was proposed [9, 10]. Figure 2.9

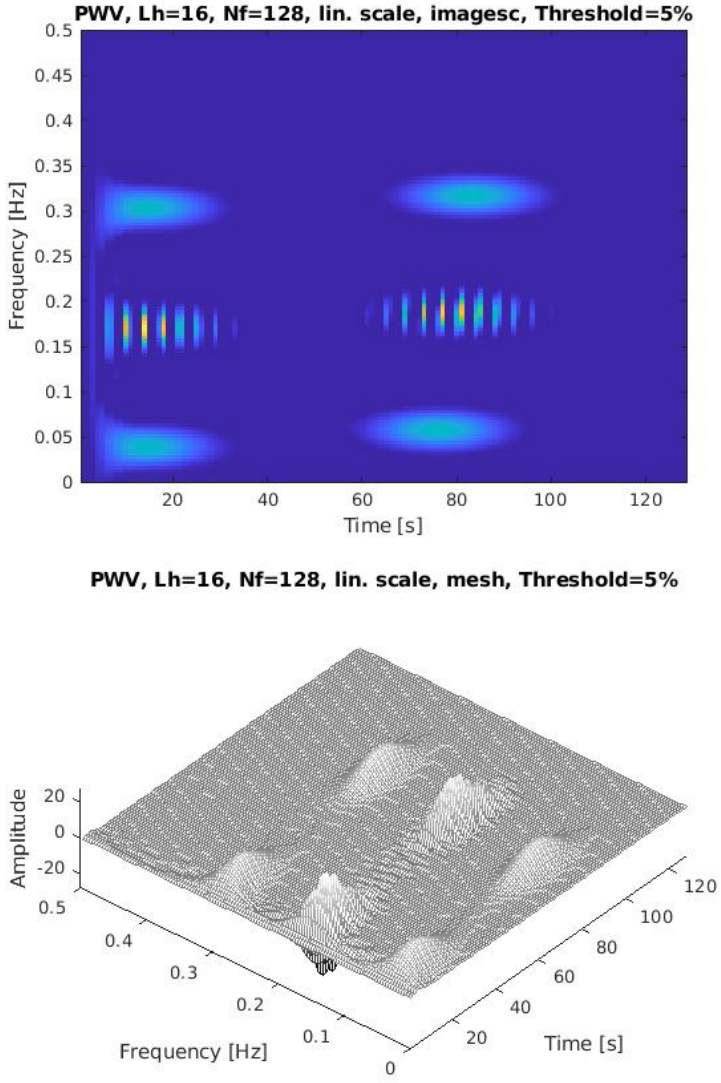

FIGURE 2.8: PWVD of four atoms signal. 2D plot (top) and mesh plot (bottom).

show the SPWVD of the previous signal. We can observe that the SPWVD is cross-terms free. However, the SPWVD uses sliding windows in time and

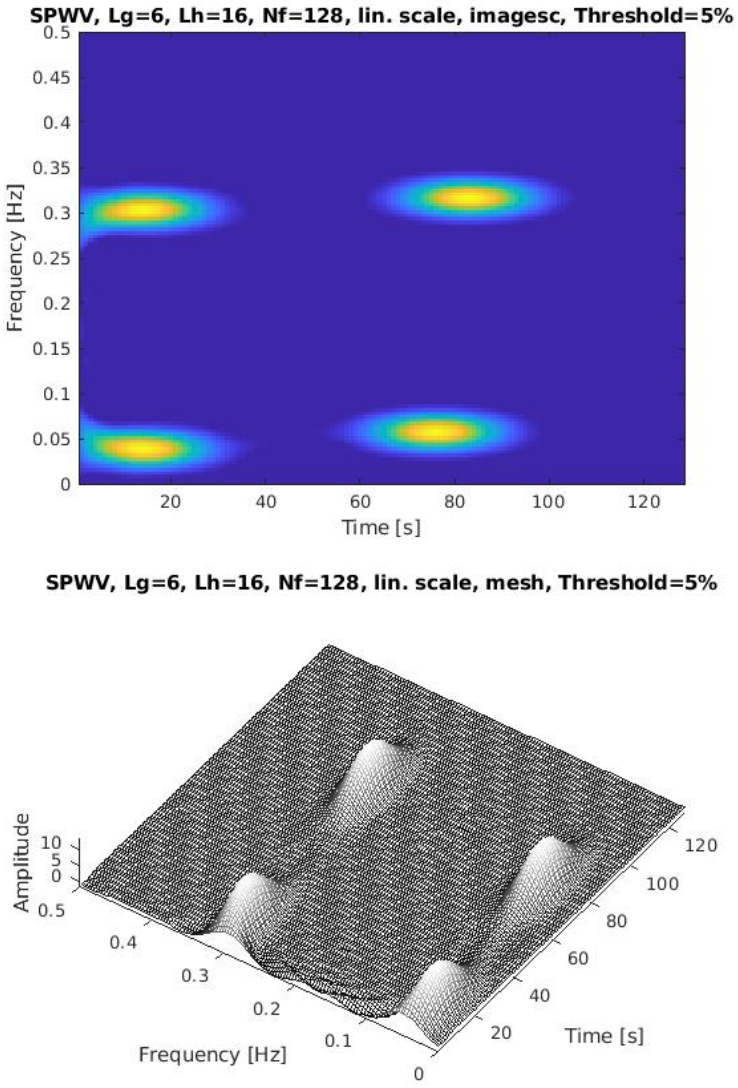

FIGURE 2.9: SPWVD of four atoms signal. 2D plot (top) and mesh plot (bottom).

frequency to capture the frequency characteristics as functions of time. A particularly interesting of smoothing implements a time and frequency separable kernel, as a product of a temporal window and spectral window, which are controlled arbitrarily and independently.

$$SPWVD_x(t,f) = \int_{-\infty}^{+\infty} h(\tau) \int_{-\infty}^{+\infty} g(s-t) x_a \left(s + \frac{\tau}{2}\right) x_a^* \left(s - \frac{\tau}{2}\right) \mathrm{d}s \, e^{-j2\pi f \tau} \mathrm{d}\tau \tag{2.10}$$

It is one of the best performing TFDs when no information on the signal parameters is available or when analyzing signals with high number of components and non-linear IF laws [11]. The main drawback of filtering operation is the degradation of time-frequency concentration and resolution (as we can see in Figure 2.10, SPWVD fail to solve two components).

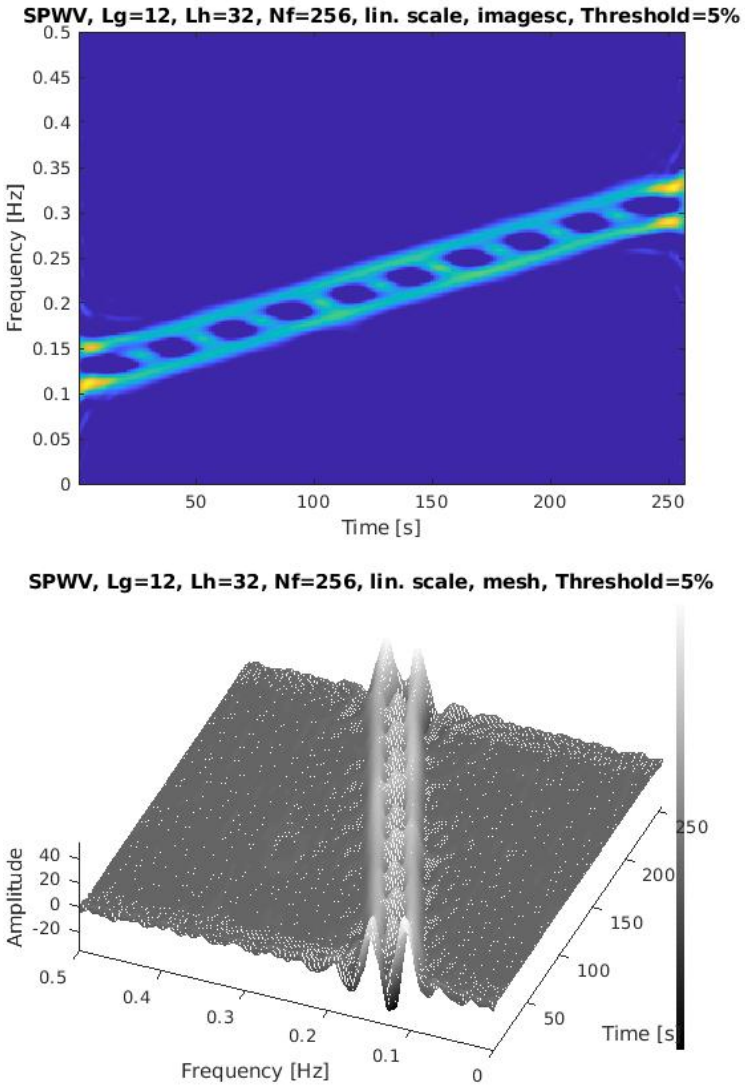

FIGURE 2.10: SPWVD of two closely spaced parallel linear FM.
2D plot (top) and mesh plot (bottom).

2.6.4 Pseudo Margenau-Hill distribution

The Margenau-Hill is the most general expression of a Cohen's class member deduced from linear time-frequency representations. It takes the form of a product of two short-time Fourier transforms, and also amounts to a separable time and frequency filtering of the Rihaczek distribution, just like

the smoothed pseudo Wigner-Ville distribution does for the Wigner-Ville distribution. Margenau-Hill distribution can extract the instantaneous frequency to characterize the temporal variation of low-frequency electromechanical oscillations [12]. Furthermore, Margenau Hill distribution also has been applied to intra-pulse modulation classification and oscillometric pressure waveforms [12]. For Margenau-Hill would bring the serious interference by cross term, it paid attention to Pseudo Margenau-Hill distribution (PMHD).The PMHD is the smoothed version of Margenau-Hill, wich can defind as [13]

$$PMHD_x(t,f) = \frac{1}{2}\int_{-\infty}^{+\infty} h(\tau)\left[x(t+\tau)x^*(t) + x(t)x^*(t-\tau)\right]e^{-j2\pi f\tau}d\tau \tag{2.11}$$

Good cross-term and interference's rejection characteristics can be obtained using the pseudo Margenau–Hill distribution (PMHD), which depends on a smoothing window.

The use of the Margenau-Hill distribution for a multi signal components are at the same positions in time or frequency is not recommended, due to the superposition of these terms on the useful signal. Figure 2.11 shows the smoothed distribution of Margenau-Hill for a four atoms signal. We can see that the cross terms are better reduced but the concentration and resolution are affected.

2.6.5 Pseudo Page distribution

Motivated by the development of a causal energy density, Page proposed the following distribution (the Page distribution) [14, 15, 16]

$$\begin{aligned} PD_x(t,f) &= \frac{d}{dt}\left\{\left|\int_{-\infty}^{t} x(u)e^{-j2\pi fu}du\right|^2\right\} \\ &= 2\Re\left\{x(t)\left(\int_{-\infty}^{t} x(u)e^{-j2\pi fu}du\right)^* e^{-j2\pi ft}\right\} \end{aligned} \tag{2.12}$$

The proposed causal energy density is calculated at each time instant through the overall duration of the signal.

Page distribution is the only distribution of Cohen's class that is unitary, simultaneously causal, compatible with modulations, and preserves time-support. On the other hand, it verifies most properties of the WVD, except for group delay and compatibility with filterings. The frequency-smoothed version of the Page distribution is named the pseudo Page distribution (PPD). The PPD allows suppressing the interferences between signal components.

Unfortunately, although PPD reduces interferences, concentration performance is systematically degraded (Figure 2.12). The situation becomes more complex for noisy signals.

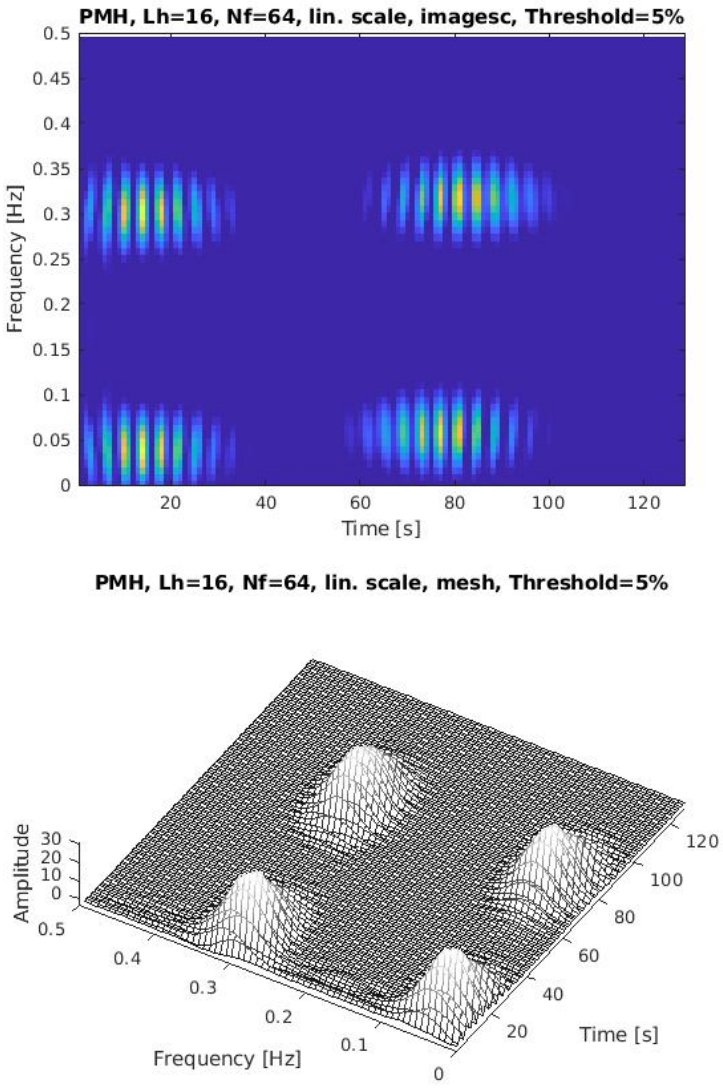

FIGURE 2.11: PMHD of four atoms signal. 2D plot (top) and mesh plot (bottom).

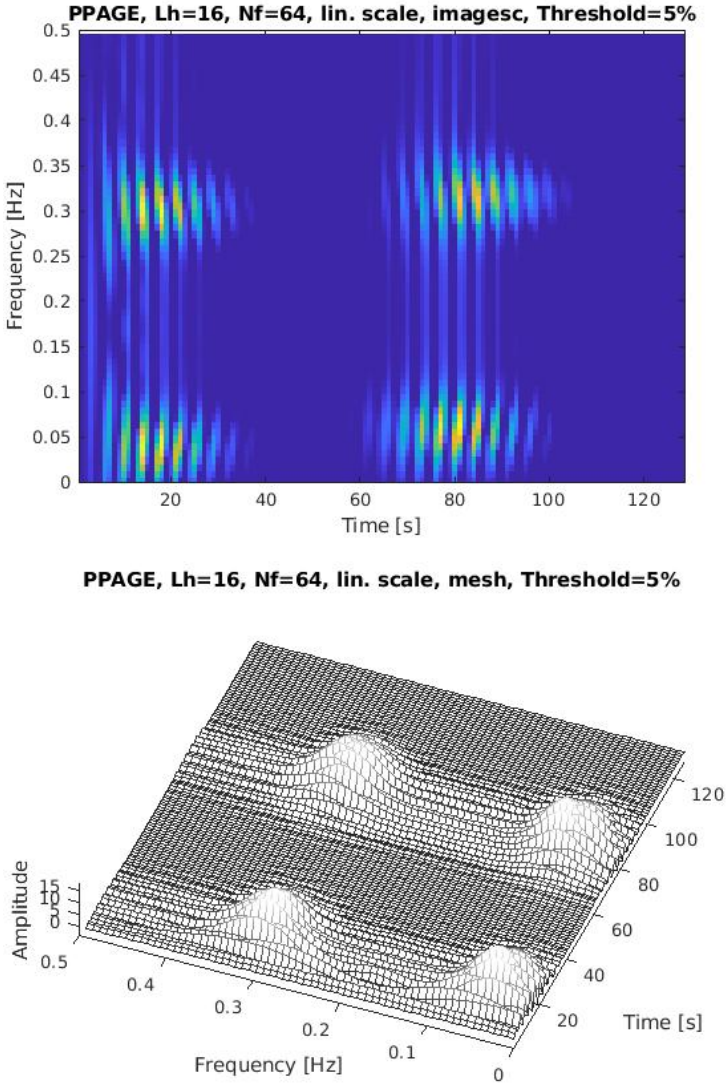

FIGURE 2.12: PPD of four atoms signal. 2D plot (top) and mesh plot (bottom).

2.6.6 Choi–Williams distribution

The Choi–Williams distribution (CWD) seeks to reduce the interference terms of WVD while maintaining many of its properties. For this purpose, it is considered an energy representation belonging to the Cohen class. It is defined using a Gaussian kernel as [1]

$$CWD_x(t,f) = \iint \frac{\sqrt{\pi\sigma}}{|\tau|} e^{\frac{-\pi^2\sigma(t-u)^2}{\tau^2}} x\left(u+\frac{\tau}{2}\right) x^*\left(u-\frac{\tau}{2}\right) e^{-j2\pi f\tau} du d\tau \quad (2.13)$$

Where σ represents the kernel width, which controls the interference's rejection in the time-frequency plane; If σ is very large, the function is relatively flat and cross-term suppression is not achieved and the Choi–Williams dis-

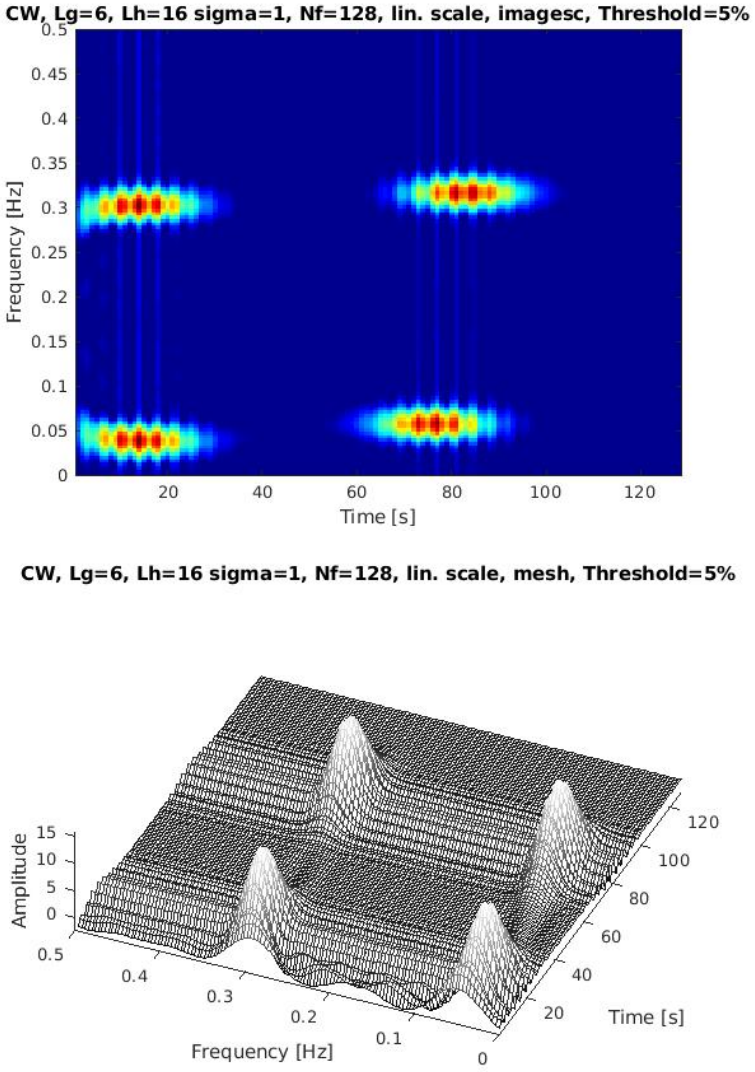

FIGURE 2.13: CWD of four atoms signal. 2D plot (top) and mesh plot (bottom).

tribution turns into a WVD. For small values of σ, the function is peaked at the origin, is one along the axis, and falls off away from the axis. Therefore this kernel satisfies the cross term minimization (best interference smoothing can be obtained, see Figure 2.13) property. The benefits of CWD lie in the satisfaction of many WVD properties, in particular concerning temporal and frequency marginal, and the interference terms reduction. Also, the CWD shows no interferences within the time–frequency plane since the components do not share the same time and frequency supports. Conversely, its disadvantages result from the non-conservation of the temporal and frequency supports. On the other hand, the kernel of the CWD is interfering for regions localized at the same frequency or time regions over the time–frequency plane. Therefore, the effectiveness of the Choi–Williams depends enormously on the content of the analyzed signals.

2.6.7 B-distribution, modified B-distribution and the extended modified B-distribution

There are several attempts in introducing a new kernel function that effectively reduces cross-terms while preserving time–frequency resolution. This class of distribution is called reduced interference TFD. B-distribution (BD), modified B-distribution (MBD), and extended modified B-distribution kernels' are belong to this class [17, 18, 1].

The B-distribution satisfies most of the desirable properties sought for a time-frequency distribution [18, 19]. Authors in [18, 19], show that the B-distribution is real, time and frequency shift invariant and its first moment with respect to the frequency yields the instantaneous frequency of the signal. They applied the method of cross-terms filtering in the ambiguity domain to the design of a low-pass filter-type kernel with a sharp cut-off, essential to ensure the clear separation of the auto-terms from the cross-terms. The equation for the B-distribution may be written in the following form [17, 18, 1]

$$BD_x(t,f) = \iint \frac{|\tau|^{\beta}}{\cosh^{2\beta}(t-u)} x_a\left(u+\frac{\tau}{2}\right) x_a^*\left(u-\frac{\tau}{2}\right) e^{-j2\pi f\tau} \mathrm{d}u\, \mathrm{d}\tau \quad (2.14)$$

Where β is the kernel parameter. However, the BD kernel has a sharp cut-off edge around the origin of the Doppler-lag plane. The volume of the kernel is controlled by its parameter. When $\beta = 0$, the B-distribution kernel becomes null at the origin in the ambiguity domain where more signal auto-terms are present in this plane [1]. To address this issue, an improved version of B-distribution based kernel namely Modified B-distribution was introduced [20, 1].

MBD removes the cross-term interference and retains a high time–frequency resolution [1]. It also provides superior performance in

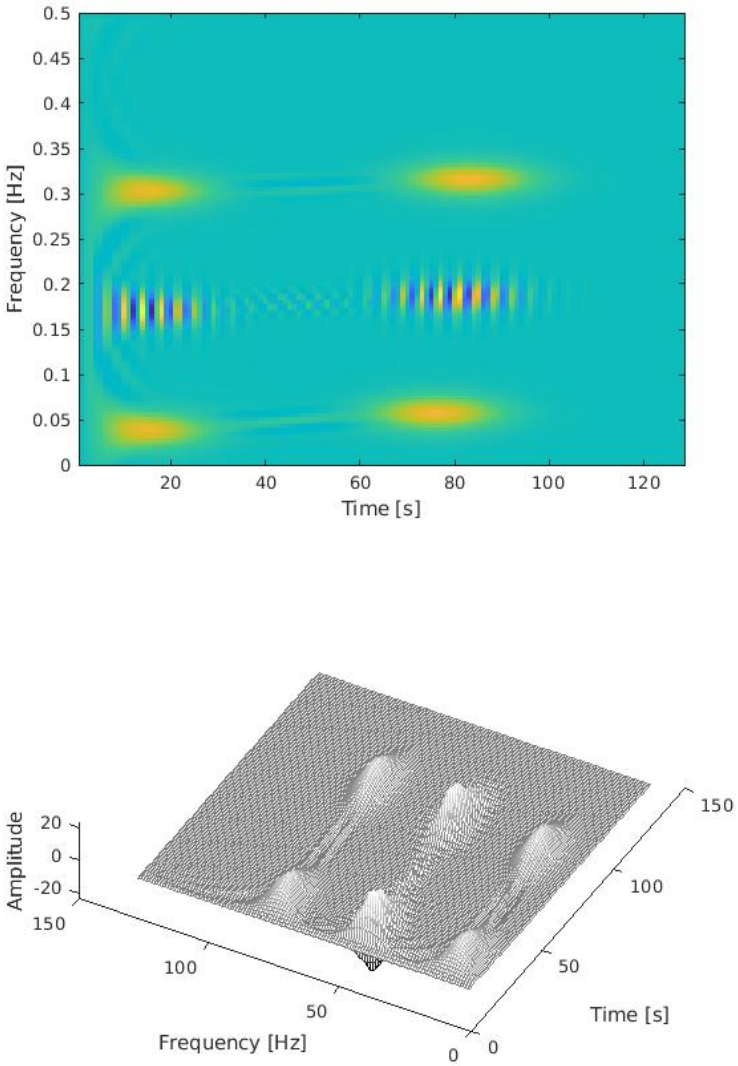

FIGURE 2.14: BD of four atoms signal. 2D plot (top), and mesh plot (bottom).

strengthening closely spaced auto-terms. The MBD is expressed as [1]

$$MBD_x(t,f) = \iint \frac{\cosh^{-2\beta}(t-u)}{\int \cosh^{-2\beta}\xi \mathrm{d}\xi} x_a\left(u+\frac{\tau}{2}\right) x_a^*\left(u-\frac{\tau}{2}\right) e^{-j2\pi f\tau} \mathrm{d}u\ \mathrm{d}\tau \tag{2.15}$$

The MBD does not have any parameters to adapt a specific direction of the smoothing window in the TF domain. Therefore, this method cannot achieve an optimal energy concentration for frequency modulated signals that follow a certain direction in the TF plane.

The Extended Modified B Distribution (EMBD) is an improvement of the MBD obtained by adding an identical kernel function in the lag direction in the ambiguity domain [1]. This modification allows the EMBD to include smoothing over both time and frequency axes (the MBD performs smoothing only over the time axis) [1]. It is essentially cross-terms free and has high resolution in the time-frequency domain. However, the extended version of the modified B-distribution is given by [1]

$$\begin{aligned} EMBD_x(t,f) = \iint & \frac{|\Gamma(\alpha+j\pi\tau)|^2 \cosh^{-2\beta}(t-u)}{\Gamma^2(\alpha)\int \cosh^{-2\beta}\xi \mathrm{d}\xi} \\ & \times x_a\left(u+\frac{\tau}{2}\right) x_a^*\left(u-\frac{\tau}{2}\right) e^{-j2\pi f\tau} \mathrm{d}u\ \mathrm{d}\tau \end{aligned} \tag{2.16}$$

Where α and β are kernel parameters. This TFD use these two parameters to control the kernel bandwidth in the ambiguity domain.

2.6.8 Compact kernel distribution

The choice of the two-dimensional kernel is crucial in the definition of a quadratic TF distributions and it determines the properties of the generated distribution e.g. instantaneous frequency (IF), marginal conditions, real-valued, as well as its overall performance in terms of energy concentration and resolution. The general purpose of the two-dimensional kernel is to reduce the interference terms in the time-frequency distribution. One of the best useful kernels proposed for this goal, are compact kernels (CKs). Compact kernel distributions are proposed to vanish outside a given range in the ambiguity plane; unlike Gaussian windows, they do not have infinite length, so there is no need to truncate the kernel using rectangular windows that may cause loss of information and the processing time [1]. These TFDs have been shown to outperform many other fixed kernel-based methods in terms of their ability to eliminate cross-terms while preserving the resolution of auto-terms in some cases [1]. Such high-resolution performance (Figure 2.16) is attained by these kernels by combining their compact support with a flexibility to adjust both size and shape of the kernel independently, as expressed

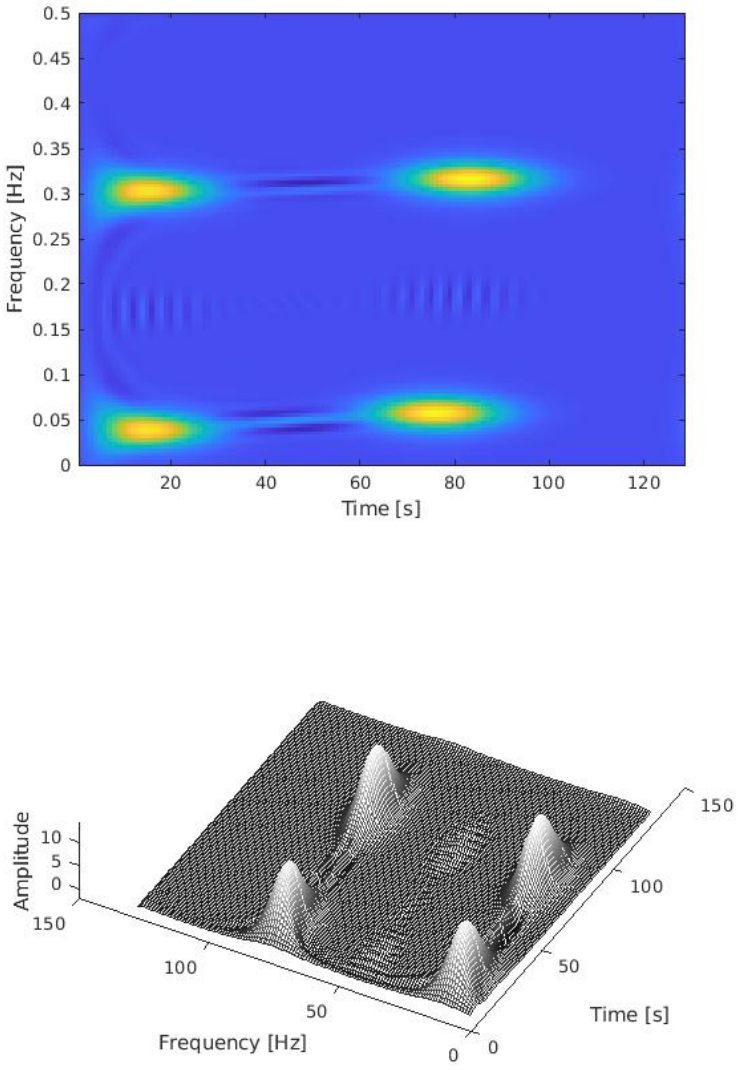

FIGURE 2.15: EMBD of four atoms signal. 2D plot (top) and mesh plot (bottom).

below [1]

$$g(\nu,\tau) = G_1(\nu)g_2(\tau) = \begin{cases} e^{2c}e^{\frac{cD^2}{\nu^2-D^2}+\frac{CE^2}{\tau^2-E^2}} & |\nu| < D, \quad |\tau| < E, \\ 0 & \text{otherwise.} \end{cases} \tag{2.17}$$

where c, D, and E are the smoothing parameters. Where $G_1(\nu)g_2(\tau)$ is separable the kernel in Doppler-lag domain, ν is Doppler and τ is time lag.

The general form of the quadratic time-frequency distribution is given by [1]

$$TFD_x(t,f) = \iiint g(\nu,\tau)x_a\left(u+\frac{\tau}{2}\right)x_a^*\left(u-\frac{\tau}{2}\right)e^{j2\pi(\nu t-\nu u-f\tau)}\mathrm{d}u\ \mathrm{d}\nu\ \mathrm{d}\tau \tag{2.18}$$

The above equations show that both Duppler ν and lag τ windows are determined, respectively, by the parameters D and E. While parameter c controls their shape [1]. Moreover, the kernel width in the Duppler-lag domain can be explicitly determined by prior knowledge of the signal components [1]. However, the compact kernel distribution-based are designed to have an extra degree of freedom to adjust both the length and shape of the Duppler-lag filter so that they can achieve the best energy concentration for auto-terms with significant reduction of cross-terms.

2.7 Conclusion

The need for defining time-frequency tools when dealing with nonstationary signals and the main aspects of TFRs have been reviewed in this chapter in the context of the current study. An attempt was made to provide a comparison between the most relevant TFRs and a clear basis for choice. The criterion of choice is based on one's intuition of how a TFR should perform for suitable analysis. The review concentrated around T-F belonging to the linear and non-linear TFRs class.

The limitation of the WVD with regard to cross-terms was addressed. Alternatively, a smoothing procedure will reduce their effect, at the expense of decreased resolution and affects localizing the signal within the time–frequency plane. Therefore, a trade-off between interference attenuation and time–frequency localization should be respected.

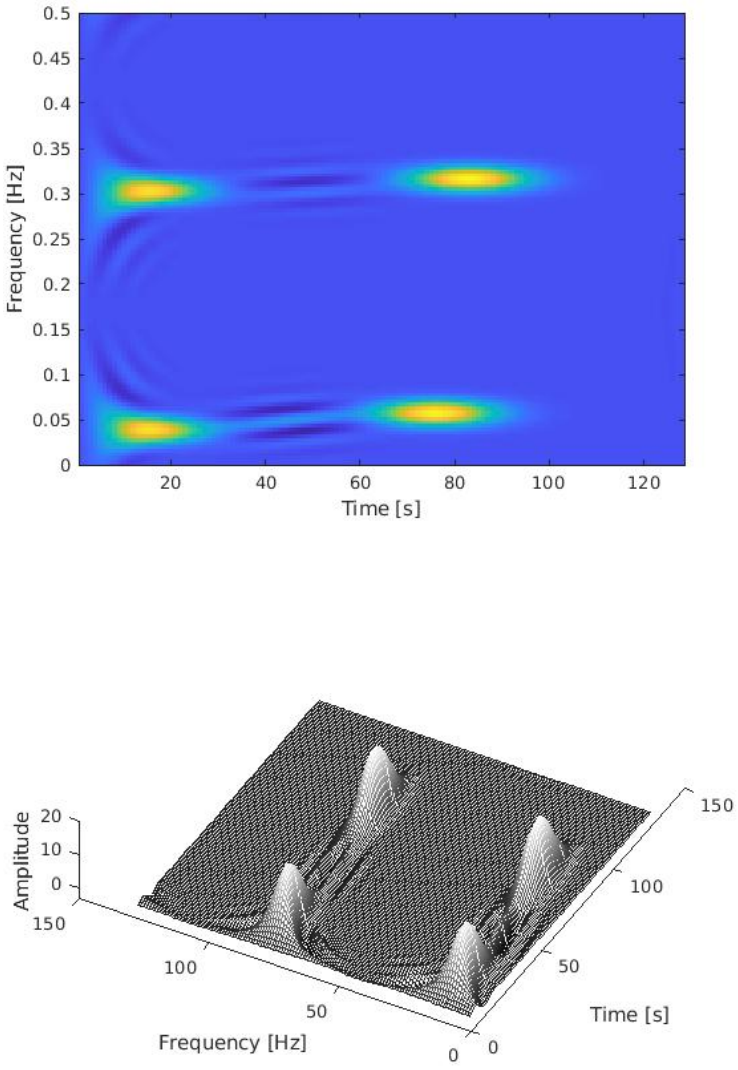

FIGURE 2.16: CKD of four atoms signal. 2D plot (top) and mesh plot (bottom).

Chapter 3

Readability enhancement of TFRs: Methods and performance comparison

3.1 Introduction

As discussed in Chapter 2, time-frequency representations aim to extract relevant characteristics of the signal by representing it over a two- dimensional plane. These methods have been extensively studied in the last decade, resulting today in many useful analysis T-F methods. Among them, the linear TFRs and the quadratic TFRs are probably the most widely used. The linear methods are easy to implement. However, according to the uncertainty principle, these methods cannot achieve the best time resolution and frequency resolution simultaneously. Bilinear or quadratic TFRs originating from the Wigner-Ville distribution are powerful tools for analyzing non-stationary signals. However, the trade-off between concentration and cross-terms removal is a classical problem when dealing with these methods. These shortcomings must be overcome in order to obtain time-frequency representation that can be both easily read and easily included in a signal processing application. This is exactly what the enhancement methods have been devised for. In this chapter, the theoretical background to enhancement time-frequency signal analysis is presented and examples of basic and commonly used methods are given.

3.2 Reassignment method

A general procedure for enhancing the time-frequency resolution and readability of TFDs is the reassignment principle. The reassignment idea was introduced in 1976. It was applied to the spectrogram by Kodera [21] then reintroduced and generalized by Auger and Flandrin as a post-processing technique to any time-frequency distribution [22, 23]. The reassignment method has been successfully applied to the best-known TFDs such as pseudo WV distribution (PWVD), smoothed pseudo WV distribution (SPWVD), pseudo Page distribution (PPD), pseudo Margenau-Hill distribution (PMHD), just to

name a few. The authors in [24] propose a reassignment process that uses the second order derivatives of the phase of the short-time Fourier transform (STFT), and provides the user with a setting parameter. The latter allows producing either a weaker or a stronger localization of the signal components in the time-frequency plane.

3.2.1 Principle

The reassignment method has been proposed as a way to improve the concentration of time-frequency representations by assigning the values of a TFR to a center of gravity of the considered time-frequency region [1, 25]

$$\hat{t}_x(t,f) = \frac{1}{SP_x^h(t,f)} \iint uWVD_x(u,v)WVD_h(t-u,f-v)\mathrm{d}u\ \mathrm{d}v \tag{3.1}$$

$$\hat{f}_x(t,f) = \frac{1}{SP_x^h(t,f)} \iint vWVD_x(u,v)WVD_h(t-u,f-v)\mathrm{d}u\ \mathrm{d}v \tag{3.2}$$

where $\hat{t}$, $\hat{f}$, SP_x^h, and WVD are new time and frequency points, spectrogram of signal $x(t)$ using window h, and Wigner-Ville distribution, respectively. The spectrogram value SP_x^h is moved from (t,f) to $(\hat{t},\hat{f})$, leading to define the reassigned spectrogram as [1]

$$RSP_x^h(t,f) = \iint SP_x^h(u,v)\delta\left(t-\hat{t}_x(u,v)\right)\delta\left(f-\hat{f}_x(u,v)\right)\mathrm{d}u\ \mathrm{d}v \tag{3.3}$$

where δ is Dirac function.

The reassignment principle has been used with a large number of distributions, which can be defined as [1, 25]

$$\mathrm{RTFR}_x\left(t',f'\right) = \int_{-\infty}^{+\infty}\int_{-\infty}^{+\infty} \mathrm{TFR}_x(t,f)\delta\left[t'-\widehat{t}(t,f)\right]\delta\left[f'-\widehat{f}(t,f)\right]\mathrm{d}t\ \mathrm{d}f, \tag{3.4}$$

where

$$\widehat{t}(t,f) = t - \frac{\int_{-\infty}^{+\infty}\int_{-\infty}^{+\infty}\tau\phi(\tau,v)\mathrm{WVD}_x(t-\tau,f-v)\mathrm{d}\tau\mathrm{d}v}{\int_{-\infty}^{+\infty}\int_{-\infty}^{+\infty}\phi(\tau,v)\mathrm{WVD}_x(t-\tau,f-v)\mathrm{d}\tau\mathrm{d}v} \tag{3.5}$$

$$\widehat{f}(t,f) = f - \frac{\int_{-\infty}^{+\infty}\int_{-\infty}^{+\infty}v\phi(\tau,v)\mathrm{WVD}_x(t-\tau,f-v)\mathrm{d}\tau\mathrm{d}v}{\int_{-\infty}^{+\infty}\int_{-\infty}^{+\infty}\phi(\tau,v)\mathrm{WVD}_x(t-\tau,f-v)\mathrm{d}\tau\mathrm{d}v} \tag{3.6}$$

where $\phi(\tau,v)$ is the smoothing kernel.

The reassignment is often understood as the "squeezing" after the "smoothing", that is the refocusing of the signal terms after their spreading

caused by the WVD smoothing in time and frequency. It performs well only when the signal components are not too close in the time-frequency plane and the signal is embedded in moderate level of noise. However, one of the most powerful properties of the reassignment method is that the application of the reassignment process to any distribution of Cohen's class yields perfectly localized distributions for chirp signals and frequency tones [1].

3.2.2 Reassigned time-frequency representations: performance analysis

In this section, some reassigned time-frequency representations performance are analyzed. More information and practical details about the implementation of the method can be found in [26, 23, 27, 28, 29].

3.2.2.1 Reassigned spectrogram and reassigned scalogram

A typical example corresponding to a sum of two crossing linear frequency modulations (LFMs) and one non-crossing FM is analyzed. The display of the spectrogram and its reassigned version is given in Figure 3.1. The representations obtained with the scalogram and its reassigned version for the signal are presented in Figure 3.2. In this study, we utilize a scalogram with the analytical Morlet wavelet for the analysis. However, the TF localization of these TFRs is dramatically increased by the reassignment method. For the reassigned scalogram a beating effect occurs and results in interference fringes (at the point of crossing). Other simulation results are presented in Figure 3.3 and Figure 3.4.

3.2.2.2 Reassigned smoothed pseudo WV distribution

As mentioned in Chapter 2, STFT or spectrogram suffer from a difficult trade-off between frequency and time resolutions, which makes them irrelevant for several real case applications. Hopefully, other powerful TF representations exist, which can also be reassigned. For instance, the smoothed pseudo-Wigner–Ville distribution is a very flexible tool, which allows an independent adjustment of the time and frequency smoothing. However, the reassigned SPWVD can be obtained as indicated in Section 3.2.1. The improvement brought by this kind of representation is clearly evidenced as we can see in Figure 3.5 and Figure 3.6 (same signal as Figure 3.1).

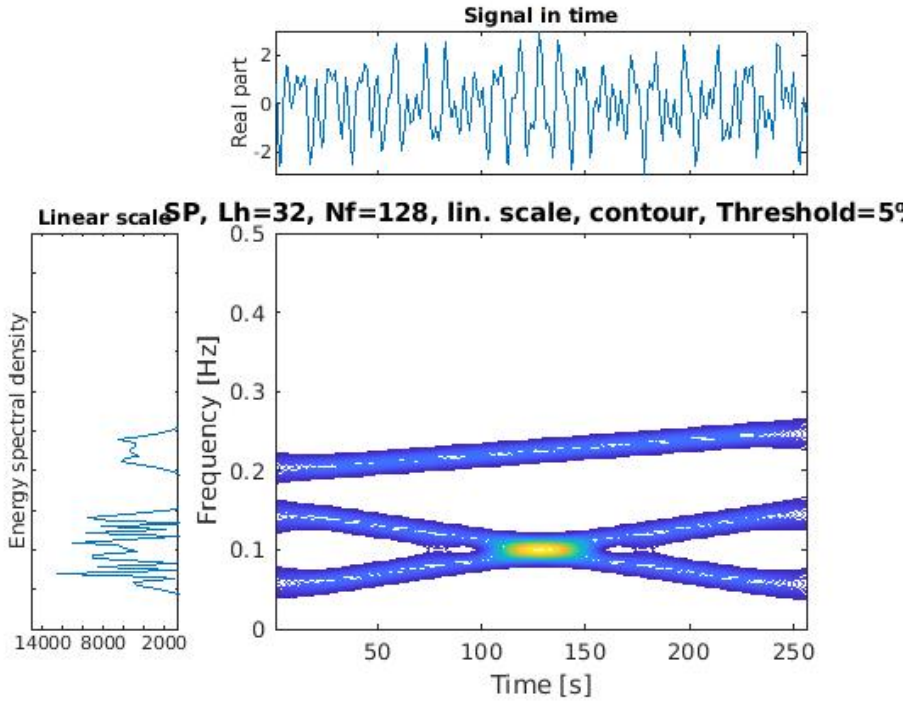

(a)

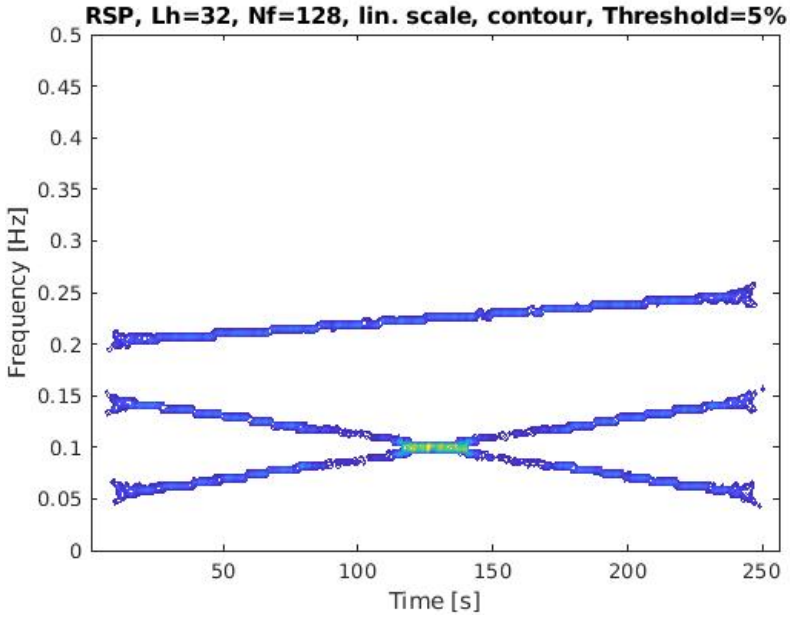

(b)

FIGURE 3.1: Time-frequency representations of sum of two crossing LFMs and one non-crossing FM . (a) Spectrogram and (b) Rassigned spectrogram.

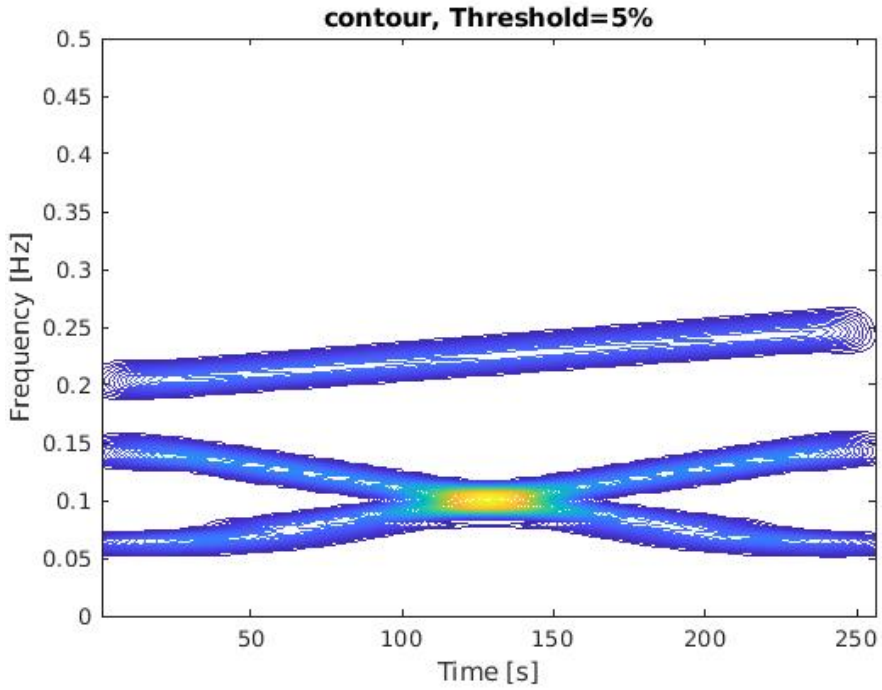

(a)

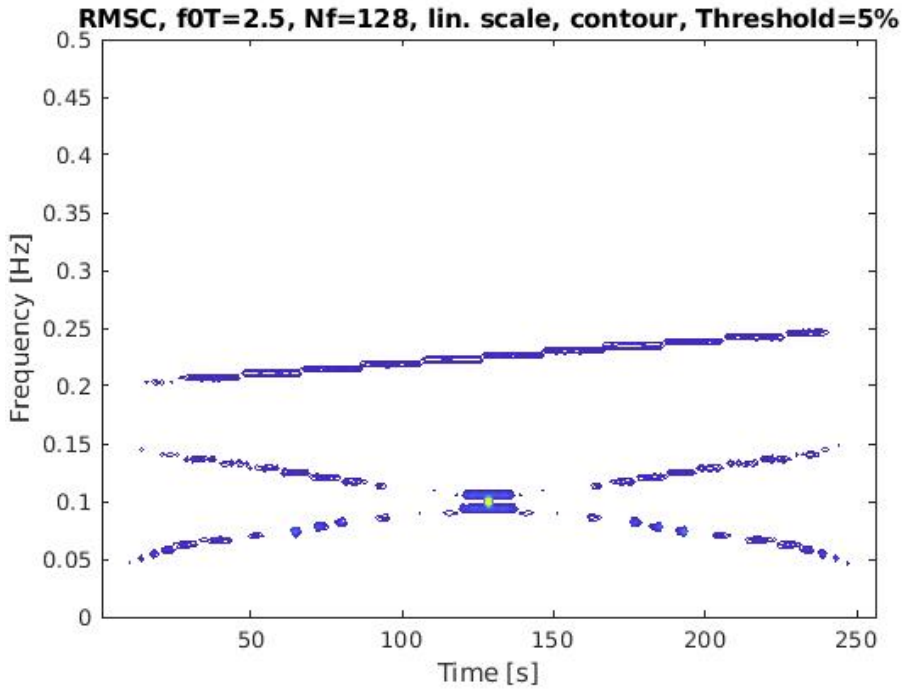

(b)

FIGURE 3.2: Time-frequency representations of sum of two crossing LFMs and one non-crossing FM . (a) Scalogram and (b) Rassigned scalogram.

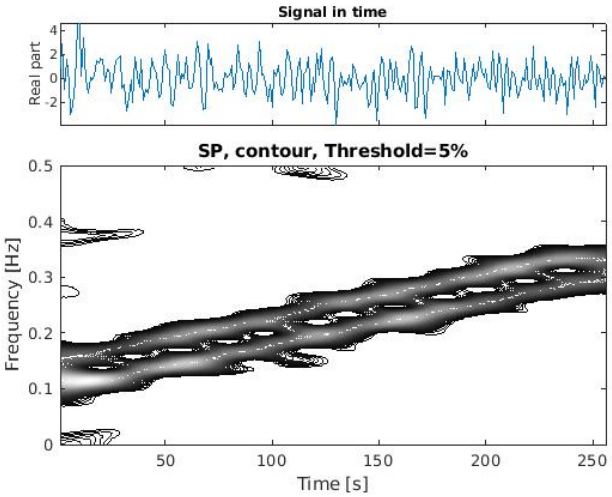

(a)

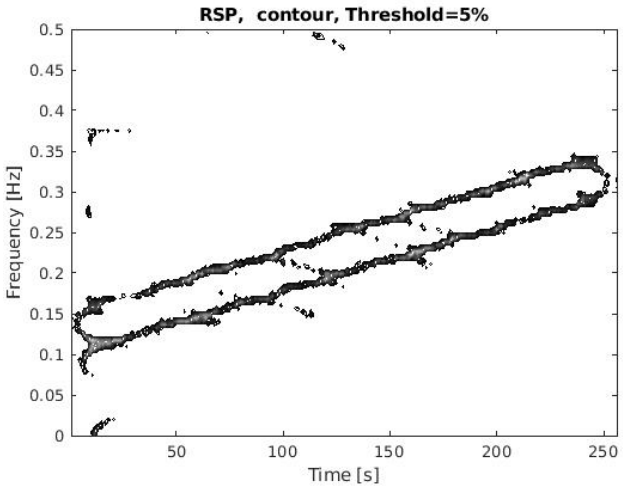

(b)

FIGURE 3.3: Time-frequency representations of parallel LFM embedded in additive noise (10 dB). (a) Spectrogram and (b) Rassigned spectrogram.

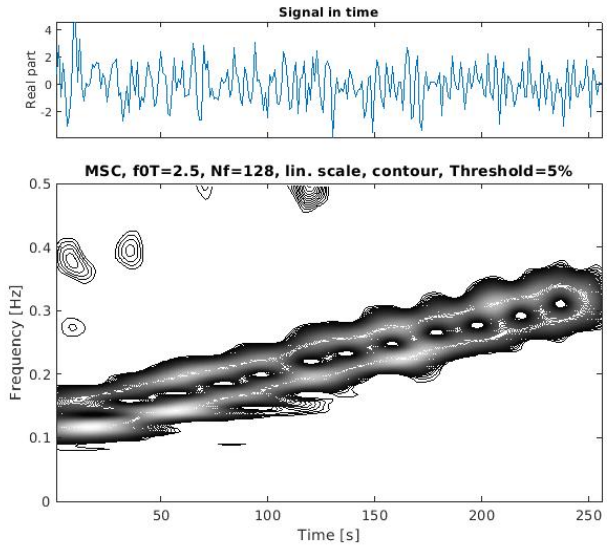

(a)

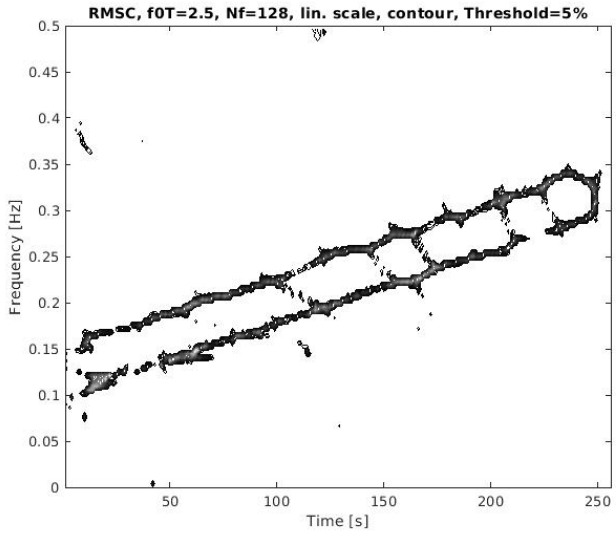

(b)

FIGURE 3.4: Time-frequency representations of parallel LFM embedded in additive noise (10 dB). (a) Scalogram and (b) Rassigned scalogram.

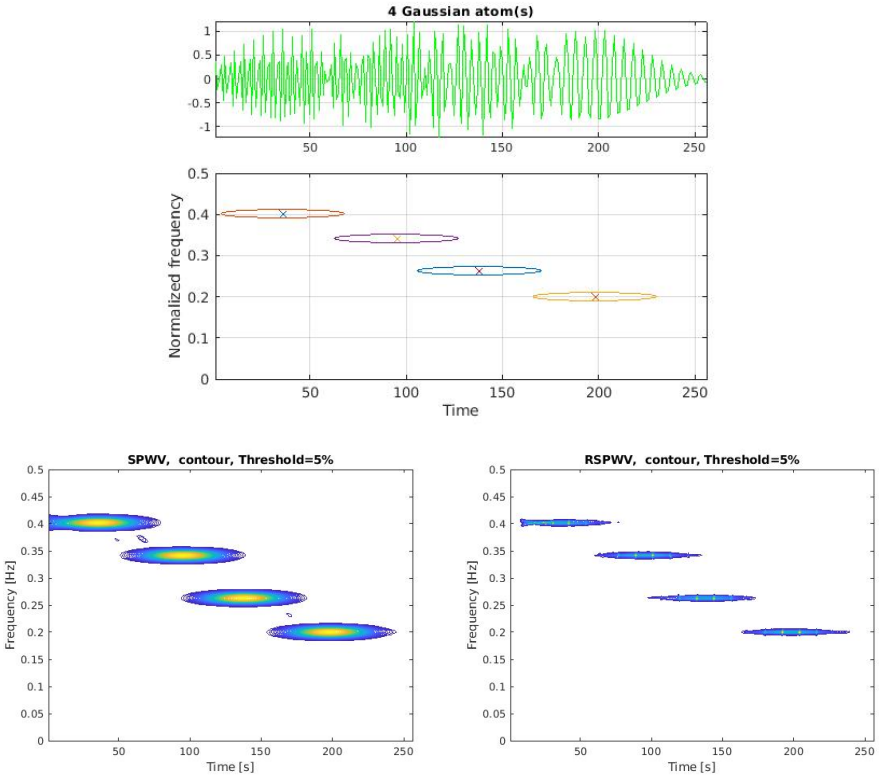

FIGURE 3.5: Time-frequency representations of four atoms. True TFR (top), SPWVD (bottom left), and reassigned SPWVD (bottom right).

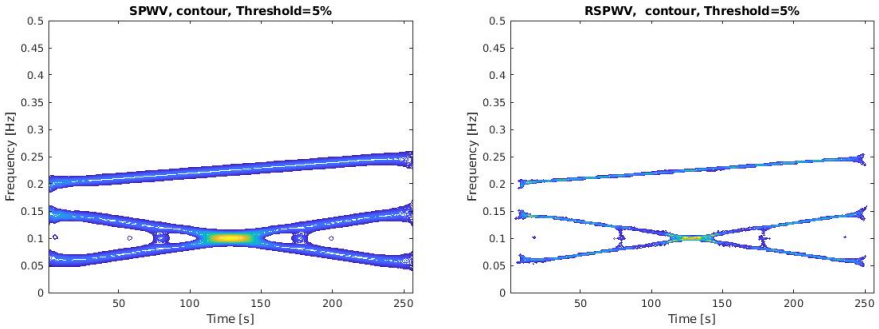

FIGURE 3.6: Time-frequency representations of sum of two crossing LFMs and one non-crossing FM . SPWVD (left) and reassigned SPWVD (right).

3.2.2.3 Other reassigned TFRs

The reassigned method has been also applied to pseudo Page distribution (Section 2.6.4) and pseudo-Margenau-Hill distribution (Section 2.6.5). Figure 3.7 and Figure 3.8 show the PPD and PHMD, and their reassigned versions using the same signal as Figure 3.1. However, these TFRs are better enhanced but the T-F quality very much depends on the original representation quality.

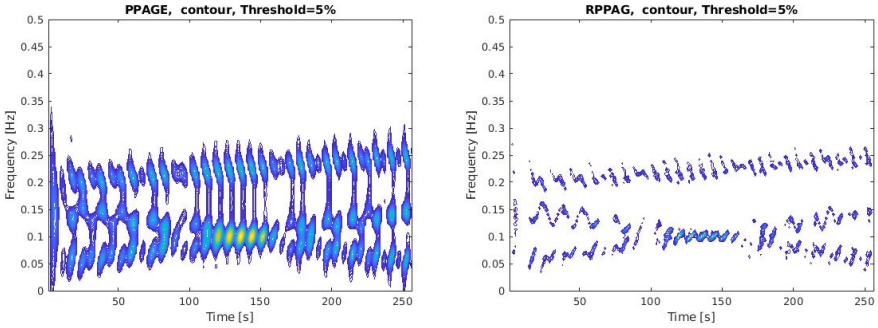

FIGURE 3.7: Time-frequency representations of sum of two crossing LFMs and one non-crossing FM. PPD (left) and reassigned PPD (right).

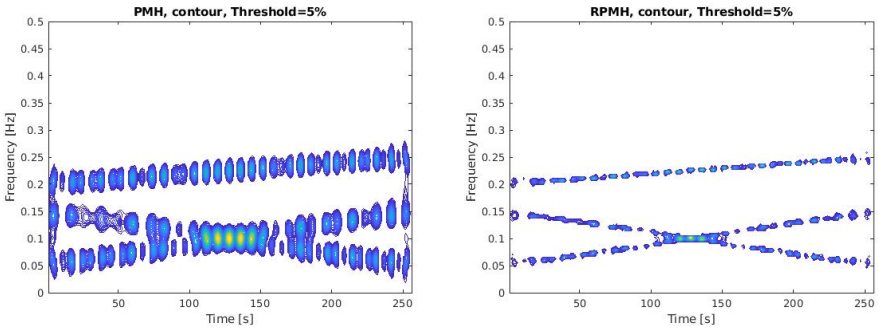

FIGURE 3.8: Time-frequency representations of sum of two crossing LFMs and one non-crossing FM. PMHD (left) and reassigned PMHD (right).

3.3 Synchrosqueezing transformation

To solve problems invertible of the reassigned spectrogram (RSP) and other reassigned TFRs, posterior processing schemes such as the synchrosqueezing method [30, 31, 32, 33] have been proposed. Initially introduced for the continuous wavelet transform and later extended to the STFT [25, 34, 35, 36]. The main limitation of these approaches is that they require the computation of several STFTs using non-causal windows which prevent their use in

real-time applications. Moreover, it is worth noting that the aforementioned techniques mostly reassign the time-frequency energy in the frequency direction, so that the strongly modulated multicomponent signal with fast varying instantaneous frequency (IF) may not be satisfactorily dealt with [31, 37, 38]. However, synchrosqueezing transform (SST) is yet another approach whose initial goal was to enhance the readability of the TFR. The SST is a special case of time–frequency reassignment method [31, 32]. In such a way that the reassigned transform was still invertible. The SST proved to be an efficient tool to obtain improved TFRs while allowing for mode retrieval. However, the SST suppresses the time–frequency blur by squeezing TF representation in a proper scale range, thus achieving a better time–frequency resolution [31, 38].

To suppress the blur along the scale dimension, the SST reallocates the time-scale distribution to the IF at any time-scale location (t, a) [38]

$$\widehat{f}(t,a) = \mathrm{Re}\left[-\mathrm{j}\frac{1}{2\pi \mathrm{CWT_x(t,a)}}\frac{\partial \mathrm{CWT}_x(t,a)}{\partial t}\right] \tag{3.7}$$

where CWT is the continuous wavelet transform (Section 2.5.2). If $\mathrm{CWT}_x(t,a) \neq 0$, yielding a Wavelet-based synchrosqueezing transform (WSST)

$$\mathrm{WSST}_x\left(t', f'\right) = \int_0^{+\infty} \mathrm{CWT}_x(t,a) a^{-3/2} \delta\left[f' - \widehat{f}(t,a)\right] \mathrm{d}a \tag{3.8}$$

WSST consists in vertically moving the coefficients according to the map $(t, \widehat{f}(t,a))$. The SST was then adapted to STFT in [39, 25, 38]. STFT based synchrosqueezing (denoted by FSST) defined as

$$\mathrm{FSST}_x\left(t', f'\right) = \frac{1}{h(0)} \int_0^{+\infty} \mathrm{STFT}_x(t,f) \delta\left[f' - \widehat{f}(t,f)\right] \mathrm{d}f \tag{3.9}$$

with

$$\widehat{f}(t,f) = \frac{1}{2\pi}\left[\frac{\partial\left[arg(\mathrm{STFT}_x(t,f))\right]}{\partial t}\right] \tag{3.10}$$

where $arg()$ is the argument of a complex number.

The effect of synchrosqueezing enhancement on the time–frequency representation can be demonstrated using a signal such as a waveform shown in Figure 3.9. The synchrosqueezing transformation produces a sharper T-F plot compared to the original TFRs. The resolution of FSST being the same whatever the frequency, the representation becomes less sharp when the modulation increases. For WSST, the representation is sharper when the frequency increases. However, SST assumes the constituent components are well separable in the frequency domain and the signal is weak frequency modulated [40].

To overcome SST drawback, many improvements have been proposed

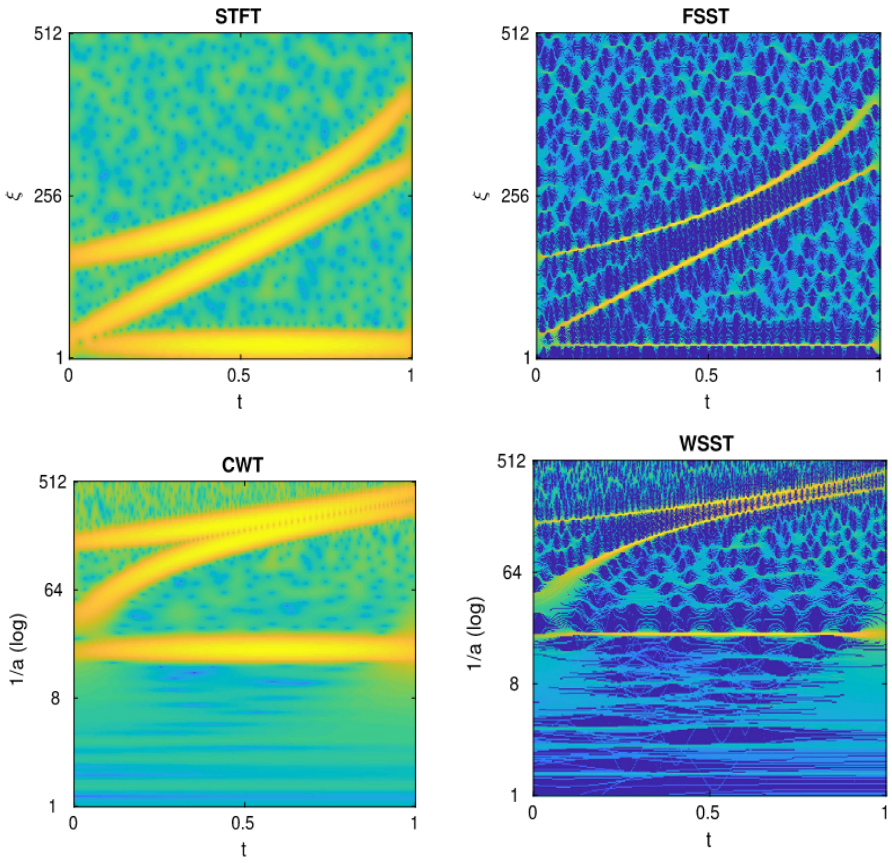

FIGURE 3.9: Illustration of STFT, CWT, FSST and WSST on a synthetic signal [41].

involving second-order synchrosqueezing transform and high-order synchrosqueezing transform [38, 37]. However, these methods are plagued by internal limitation that they operate on a linear TF representation, associated with a fixed TF resolution given by a global window or wavelet.

3.4 Other enhancement methods

3.4.0.1 Multi-taper

In a statistical sense, different attempts have been made to take advantage of the idea of multitapering [42, 43]. This is a technique originally proposed to deal with stationary signals. It is used to reduce the variance and hence stabilize power spectrum estimation in the spectral analysis. However, the classical method of multitapering still suffers from the TF localization trade-off.

3.4.0.2 S-method

To produce a T-F representation that does not suffer from a cross-term problem and has a high-energy concentration for auto-terms (close to that of the WVD), S-method was proposed. It aims to combine the advantages of both the WVD and the spectrogram. The S-method is based on the principle that the WVD can be represented as the convolution of the STFT with its conjugate along the frequency axis [1]. The enhanced spectrogram (S-method) achieves better results than the spectrogram (see Figure 3.10). However, the S-method gives high energy concentration for tones but fails to concentrate energy for the spikes [1].

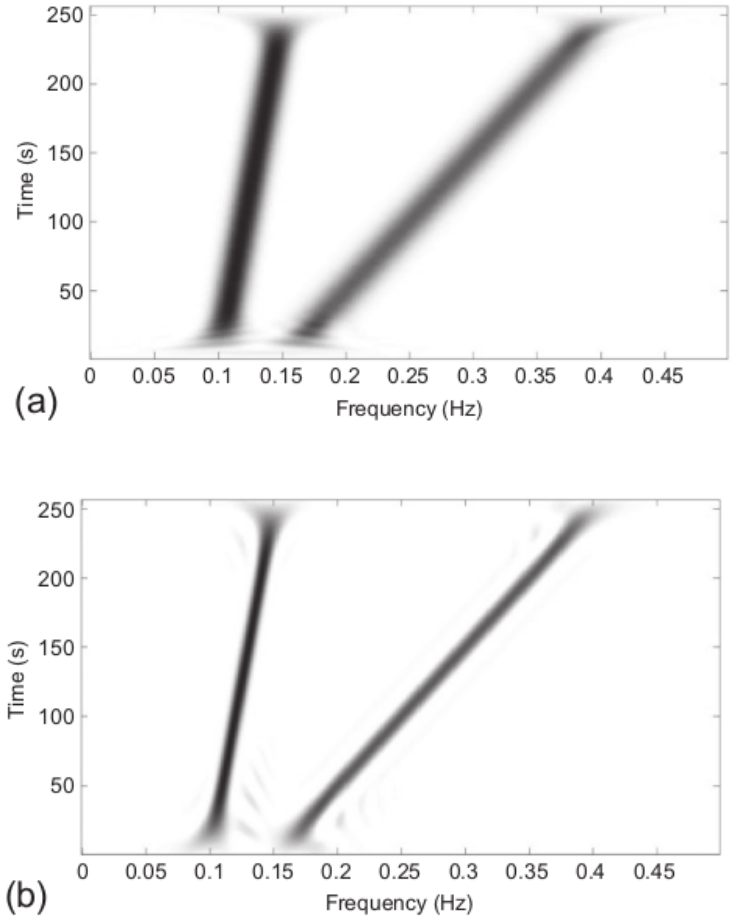

FIGURE 3.10: TFRs of a two-component signal [1]. (a) spectrogram; (b) S-method.

3.4.0.3 Image enhancement

In other sense, several studies have shown that image processing techniques can be applied to the images produced by time-frequency representations of one-dimensional signals, so that to allow IF estimation and crossterm reduction [44, 45, 46, 47]. To resolve the problem of discontinuity of IF trajectories, the peaks in [44] were tracked and their local connectivity was exploited. Like the pixels connection in images, the discrete peak points were linked to form individual components. In fact, a peak extraction is directly performed on the TFR by finding the local maxima of the distribution over time. This is

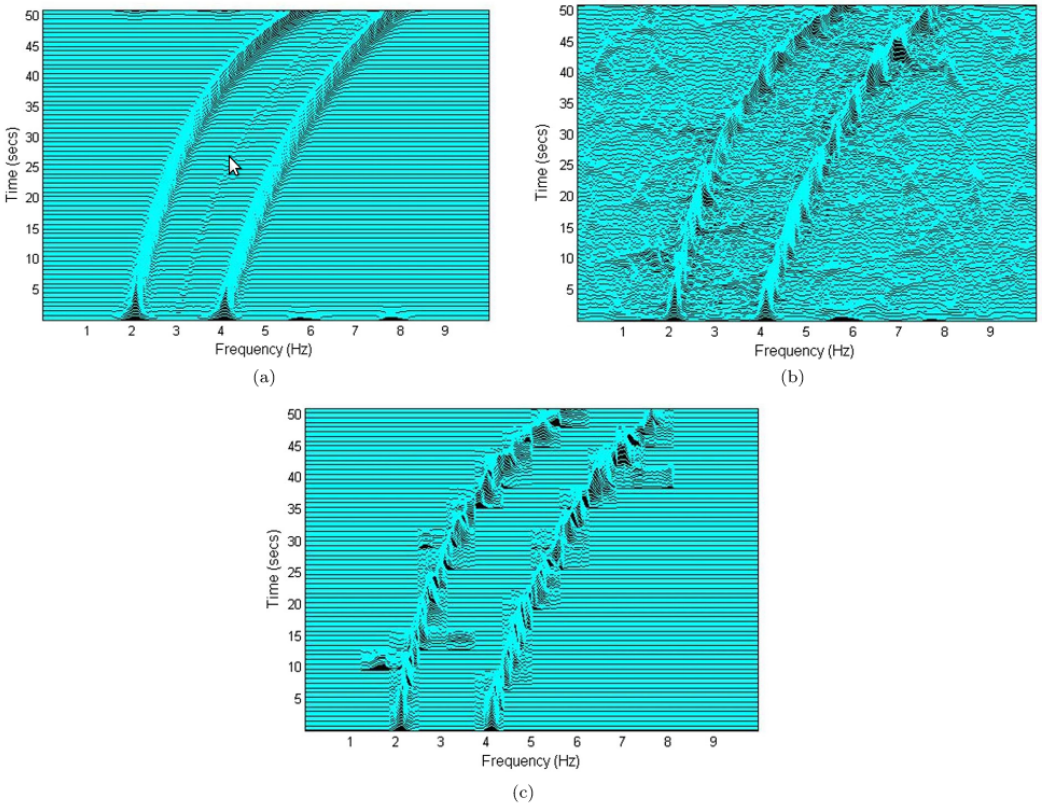

FIGURE 3.11: Illustration of the (t, f) image denoising algorithm [48]. (a) The MBD of a two-component quadratic FM signal. (b) The MBD of the same signal corrupted by additive white Gaussian noise (SNR = 0 dB). (c) The denoised MBD.

done by locating the TF points where the first derivative along the frequency axis is 0 and the second derivative is negative. This operation is followed by an image processing technique called component linking (connecting two peaks that are in a neighborhood) [44]. Denoising and enhancement [49, 50, 51], as well as classification [52, 53] were also considered. In [54], the image's histogram obtained from a time-frequency image based on the Hilbert-Huang transform was used as an input to a classifier. This method has been used to interpret a frequency response analysis of a power transformer. Other

authors even proposed segmentation for this purpose [55, 56, 57, 58, 59]. However, for the context of readability enhancement time–frequency image de-blurring and de-noising methods are used [48]. Image de-convolution techniques have been applied to estimate an original high-resolution TFD from the Spectrogram [48]. Another method used singular value decomposition to reduce noise by applying low-pass filtering to singular vectors [48]. Other image processing tools for the improvement of TFDs readability and energy concentration are described in [48, 1].

The proposed image processing methods are useful tools for readability enhancement. However, many of these methods cannot overcome the fundamental resolution limit of TFRs in dealing with closely spaced signal components [48, 1].

3.5 Conclusion

In practical applications, nonstationarity signals with the multi-components feature are close to each other, and may even have spectral overlapping or crossings when frequency varies over time, particularly under low levels of noise. Therefore, excellent time-frequency readability is in need to pinpoint the frequency contents and time variability of such signals. To address this issue, we have presented the most useful tools introduced for this propose. The enhanced representations provide considerable improvement in concentration compared to the original representations. On the other hand, the enhanced TFRs using post-processing provide clean plots compared to their original versions.

Chapter 4

Time-frequency readability enhancement of compact support kernel-based distributions using image post-processing : Application to instantaneous frequency estimation of M-ary frequency shift keying signals

4.1 Introduction

Quadratic time-frequency distributions (QTFDs) have been successfully applied to various real-life problems such as neurosciences, fault detection, communications, radar, sonar and acoustics, just to name a few [1]. These distributions constitute powerful tools to process and analyze nonstationary signals accurately and efficiently by performing a mapping from the one-dimensional input signal $x(t)$ into a two-dimensional function of time and frequency $\mathrm{TFD}_x(t,f)$ so that [60, 61, 62]

$$\mathrm{TFD}_x(t,f) = \int\int\int_{-\infty}^{+\infty} e^{j2\pi\eta(s-t)}\phi(\eta,\tau)x\left(s+\frac{\tau}{2}\right)x^*\left(s-\frac{\tau}{2}\right)e^{-j2\pi f\tau}d\eta ds d\tau \quad (4.1)$$

where $\phi(\eta,\tau)$ is the Doppler-lag kernel that can be thought of as a 2D filter that smooths interferences. Another interesting formulation can be obtained by introducing the concept of the time-lag kernel $G(t,\tau)$ defined as the Fourier transform of $\phi(\eta,\tau)$ with respect to η

$$G(t,\tau) = \int_{-\infty}^{+\infty}\phi(\eta,\tau)e^{-j2\pi\eta t}d\eta \quad (4.2)$$

Hence, any kernel-based TFD associated to the analytic signal $x_a(t)$ can be rewritten in a more compact form as follows

$$\mathrm{TFD}_{x_a}(t,f) = \int_{-\infty}^{+\infty}\int_{-\infty}^{+\infty} G(t-s,\tau)\, x_a\left(s+\frac{\tau}{2}\right) x_a^*\left(s-\frac{\tau}{2}\right) e^{-j2\pi f\tau} ds d\tau \qquad (4.3)$$

In this form, QTFDs induce various crossterms geometries. While analyzing nonstationary signals, kernel-based TFDs are expected to be crossterm free and provide the highest energy concentration of the autoterms around their respective IF laws. Unfortunately, although these TFDs that are smoothed versions of the Wigner-Ville distribution (WVD) reduce interferences, concentration performance is systematically degraded. The situation becomes more complex for noisy multicomponent signals with closely spaced components while visual inspection remains difficult and very subjective.

This chapter proposes to improve time-frequency concentration of Kernel with Compact Support (KCS)-based TFDs [63, 64], referred to as KCSDs, by using image processing tools. Herein, the use of the latter are motivated by the particular features provided by the aforementioned TFDs compared to the best-known traditional TFDs. Kernels with compact support, originally derived from the Gaussian kernel, are found to recover information loss and improve processing time and, at the same time, retain the most important properties of the Gaussian kernel [65]. Moreover, no external windows are needed to cut off the kernel. This is due to the analytical property of this type of kernels that vanish themselves outside a given set [66, 67].

The published work in [63] shows that, defining a family of compact support kernels in the time-lag domain, permits to obtain Doppler-lag KCS that are much better concentrated around the origin of the ambiguity plane. As a result, a more efficient filtering of the crossterms is performed while the signal proper terms are better preserved.

The most important characteristic of the induced TFDs, namely the Cheriet-Belouchrani distribution (CBD), the separable CB distribution (SCBD) and the polynomial CB distribution (PCBD) is that they are tuned using a single parameter that controls the kernel's bandwidth.

The following contributions are in order: The first contribution concerns the readability enhancement of the TF diagrams obtained from the optimized time-lag KCSDs. The idea is to use concentration measure to automatically select the sole optimal parameter that controls the related kernel's spread in the ambiguity domain [63]. This tuning permits to get the best concentration, resolution, interference and noise reduction. These performances are then significantly improved by introducing a low-complexity post-processing that includes a 2D Wiener filter, automatic binarization and morphological image processing techniques. It is important to be careful here and do not confuse between post-processing readability enhancement and resolution improvement which realistically cannot be achieved in the post-processing. In fact, the frequency and time resolutions are already set up while generating the

time-frequency representation used in the first place; what comes later is just interpolations. However, reducing interference and noise levels and enhancing the autoterms concentration allow improving the characteristics that affect the components resolution in the TF plane namely: energy concentration around the true IF laws, instantaneous bandwidths as well as sidelobes and crossterms amplitudes. Herein, our previously mentioned image post-processing is applied to the time-lag KCSDs to overcome the smoothing effect of the compact support kernel in the ambiguity domain and eliminate interfering terms. In order to provide an objective assessment for quantifying concentration and interference rejection, we introduce a comparative study between the proposed method and the original TFDs based on the energy concentration measure [68, 69, 70], the ratio of norms [71], the Rényi entropy [72], the stankovic measure [73], the normalized instantaneous resolution [74] and the Reinhold measure [75]. Supported by a deep analysis of time slices, extraction of the most important signal characteristics is also investigated. The proposed method is used to generate the enhanced KCS-based distributions referred to as the ECBD, the ESCBD and the EPCBD, respectively. The latter are compared to the best performing post-processing time-frequency analysis methods namely, the reassignment SP (RSP), the reassignment Stankovic distribution (RSD), the reassignment PWVD (RPWVD), the reassignment SPWVD (RSPWVD), the reassignment PPD (RPPD), and the reassignment PMHD (RPMHD) using the aforementioned performance evaluation measures. The second contribution concerns the application of the proposed method to IF estimation of multicomponent nonstationary signals embedded in noise. In particular, the enhanced PCBD plots are used to extract the IF laws of M-ary frequency shift keying (MFSK) real-life signals. Our proposed approach is compared to those results obtained from SPWVD and the best-known reassignment TFRs in terms of the mainlobe width (MLW) and the variance, respectively. Among the KCS-based TFDs, the polynomial CB distribution is herein preferred because the adjusting parameter that controls its kernel's bandwidth is an integer. This provides two practical advantages: 1) easier automatic optimization procedure and 2) possibility of real-time implementation of an IF estimator. Various Monte Carlo simulation-based comparisons confirm that the proposed approach considerably enhances the concentration of the signal proper terms and the artifacts' suppression while the accuracy of IF laws' estimation is significantly improved for both real-life and synthetic MFSK signals embedded in noise. Two radar signals are also analyzed so that to extract their main time and frequency features.

The remainder of this chapter is organized as follows. The next section introduces the quadratic TFDs derived from time-lag kernels with compact support. Section 4.3 presents the most used objective performance measures that serve to assess time-frequency representations and select their optimal smoothing parameters. Then, the proposed time-frequency readability enhancement method is described in Section 4.4. In Section 4.5, the overall performances based on concentration and interference mitigation are evaluated

using several tests involving real-life and synthetic examples. Both linear and nonlinear frequency modulated signals including very closely spaced and noisy multicomponent signals are considered. IF estimation of MFSK signals is investigated in details in Section 4.6. The results of analysis of the two CW-LFM and PLFM radar signals are presented in Section 4.7 while the computational complexity of the enhanced KCSDs is discussed in Section 4.8. Finally, Section 4.9 concludes the chapter.

4.2 KCS-based time-frequency distributions

The kernel with compact support is derived from the Gaussian kernel by transforming the space into a unit ball through a change of variables so that the Gaussian is defined on the unit ball and vanishes on the unit sphere. Then, the kernel is extended over all $\mathbb{R}^2$ by taking zero values outside the unit ball to make the convolution product possible [65]. In [76], a separable kernel with compact support (SKCS) applied to image processing was introduced while the authors in [77] proposed a new formulation of a polynomial kernel family with compact support, called PKCS, for scale-space image processing.

Table 4.1: Mathematical expressions and tuning parameters of time-lag kernels with compact support [63].

KCS-TFDs	Time-lag KCS kernels	Tuning parameters
CBD	$G_{CB}(t,\tau) = \begin{cases} e^{e_{CB}(t,\tau)} & \text{if } \frac{t^2+\tau^2}{D^2} < 1 \\ 0 & \text{otherwise.} \end{cases}$ and $e_{CB}(t,\tau) = C + \frac{CD^2}{t^2+\tau^2-D^2}$	C : a real positive parameter that adjusts the kernel's bandwidth as σ does for the Gaussian function. However, C is inversely proportional to the compact support spread. D is a predetermined parameter.
SCBD	$G_{SCB}(t,\tau) = \begin{cases} e^{e_{SCB}(t,0)e_{SCB}(0,\tau)} & \text{if } \begin{cases} t^2 < D^2 \\ \text{and} \\ \tau^2 < D^2 \end{cases} \\ 0 & \text{otherwise.} \end{cases}$ where $e_{SCB}(t,0) = C + \frac{CD^2}{t^2-D^2}$ $e_{SCB}(0,\tau) = C + \frac{CD^2}{\tau^2-D^2}$	
PCBD	$G_{PCB}(t,\tau) = \begin{cases} \frac{\gamma+1}{\pi\lambda^{2\gamma+2}}\left(\lambda^2-(t^2+\tau^2)\right)^{\gamma} & \text{if } t^2+\tau^2 < \lambda^2 \\ 0 & \text{otherwise.} \end{cases}$	γ : an integer that controls the bandwidth of the kernel's smoothing window. This results on much easier optimization of the PCBD. Here again, the kernel support is narrowed as γ increases. λ is a predetermined parameter.

Applied to time-frequency signal analysis (TFSA), the compact support

kernels namely, the G_{CB}, the G_{SCB} and the G_{PCB} are expressed in the time-lag domain as reported in Table 4.1 together with their respective smoothing parameters. We see that the induced distributions from (4.3), referred to as the CBD, the SCBD and the PCBD, are simply tuned using a single parameter that controls the bandwidth extent. This tuning is much finer using the CB and the SCB kernels since C is a real positive number.

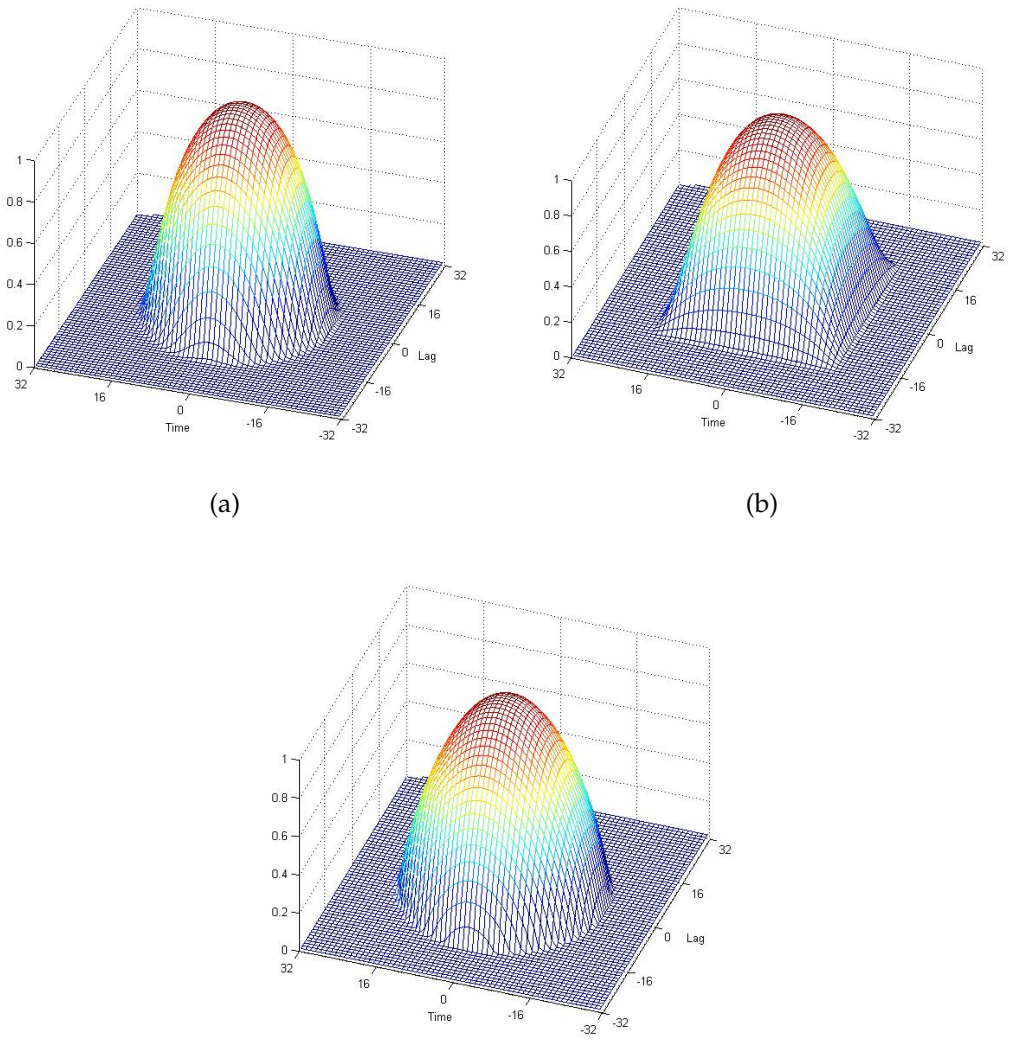

(a) (b)

(c)

FIG. 4.1: The 2D plots of the KCS kernels in the time-lag domain ($D = \lambda = 2.5$): (a) G_{CB} ($C = 0.8$), (b) G_{SCB} ($C = 0.8$) and (c) G_{PCB} normalized with respect to its peak located at the origin ($t = 0, \tau = 0$) ($\gamma = 1$).

Fig. 4.1 shows the plots of the CB, SCB and PCB kernels in the time-lag plane. The smoothing parameters C and γ are set to 0.8 and 1, respectively,

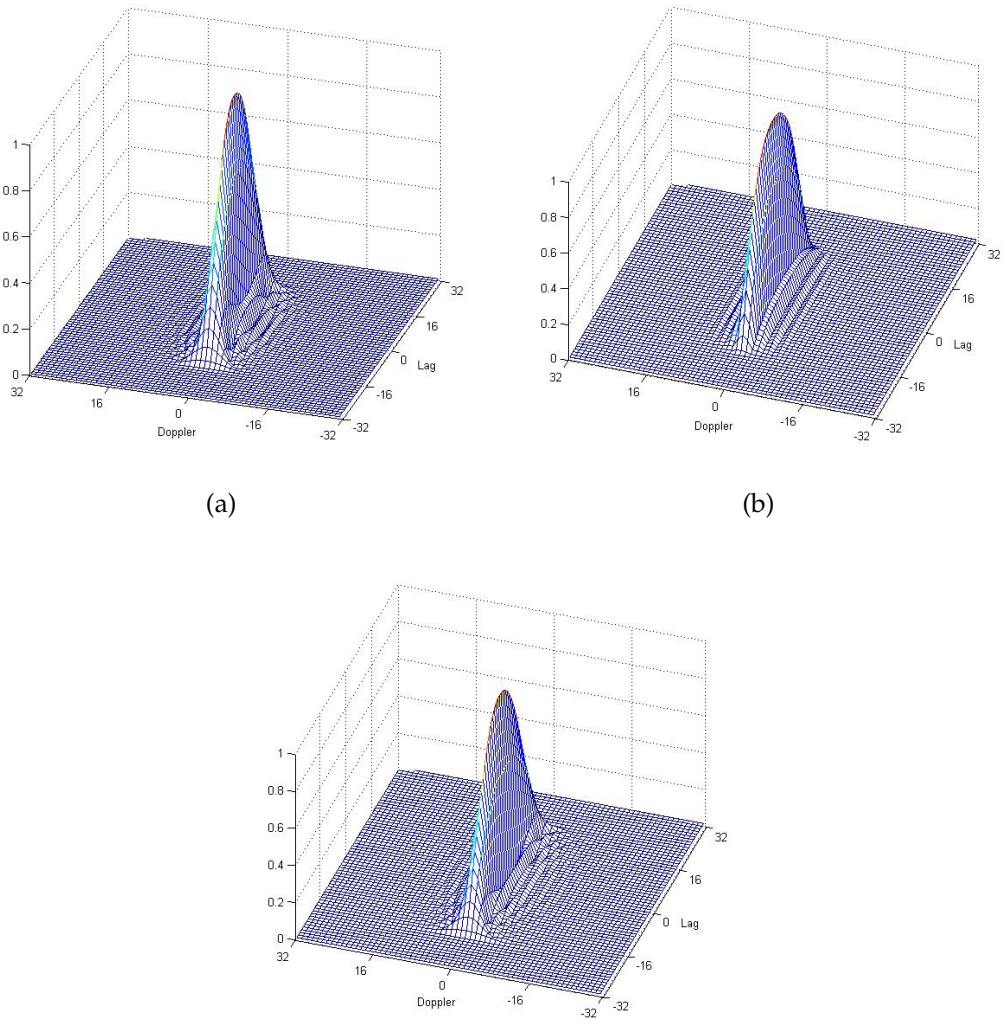

(a) (b)

(c)

FIG. 4.2: The 2D plots of the KCS kernels in the ambiguity domain normalized with respect to their peaks located at the origin ($\eta = 0$, $\tau = 0$) ($D = \lambda = 2.5$): (a) $\phi_{CB}(C = 0.8)$, (b) ϕ_{SCB} ($C = 0.8$) and (c) ϕ_{PCB} ($\gamma = 1$).

while $D = \lambda = 2.5$. The corresponding 2D profiles in the Doppler-lag plane are displayed in Fig. 4.2.

The CBD, SCBD and PCBD quadratic TFDs are real-valued, since $G_{KCS}(t, \tau) = G^*_{KCS}(t, -\tau)$, and are generated as follows: After adjusting the smoothing parameters according to the optimization procedure explained in Section 4.3, the convolutions of the compact support kernels reported in Table 4.1 and the instantaneous autocorrelation function $U_{x_a}(t, \tau) = x_a(t + \frac{\tau}{2})x^*_a(t - \frac{\tau}{2})$ are computed and then a Fourier transform is applied to determine information related to the energy of the signal $x(t)$ with respect to time and frequency.

From TFSA point of view, the most important is that, thanks to the specific forms of the three time-lag KCS, no sidelobes are generated by their inverse Fourier transforms with respect to t; the Doppler-lag kernels ϕ_{CB}, ϕ_{SCB} and ϕ_{PCB}. Centered around the origin in the ambiguity domain, the latter show a great ability of crossterms' suppression while preserving the signal proper components yielding to a notable improvement of TF resolution and energy concentration of the autoterms.

4.3 Objective performance measures of TFDs

Visual inspection of the best performing TFDs consists on looking for the most appealing TF diagrams. This corresponds to "cleaner" plots that provide better concentration of the signal's proper terms around their respective bandwidths, more accurate time-frequency localization and reduced interference and noise levels. However, the decision made is subjective and not straightforward at all. This justifies the need for quantitative performance measures to evaluate the goodness of a given joint time-frequency representation. Table 4.2 presents a selection of the most commonly used performance evaluation methods that serve to objectively assess TFDs and/or to set their optimal parameters.

Table 4.2: Objective performance measures used to assess TFDs and set their optimal smoothing parameters.

Objective measure	Mathematical expression	Optimal TFD's criterion
Ratio of norms [71, 78, 79]	$RN = \dfrac{\sum_n \sum_k \mathrm{TFD}_x^4(n,k)}{\left(\sum_n \sum_k \mathrm{TFD}_x^2(n,k)\right)^2}$	Maximize RN
Rényi entropy normalized by signal energy [72, 79, 80, 81]	$R_{NSE_\alpha} = \dfrac{1}{1-\alpha} \log_2 \left(\dfrac{\sum_n \sum_k \mathrm{TFD}_x^\alpha(n,k)}{\sum_n \sum_k \mathrm{TFD}_x(n,k)} \right)$ where α is the order of the information with $\alpha \geq 2$.	Minimize R_{NSE_α}

Continued on next page

Table 4.2: Objective performance measures used to assess TFDs and set their optimal smoothing parameters. (Continued)

Rényi entropy normalized by distribution volume [72, 79, 80, 81]	$R_{NDV_\alpha} = \frac{1}{1-\alpha}\log_2\left(\frac{\sum_n\sum_k \mathrm{TFD}_x^\alpha(n,k)}{\sum_n\sum_k \lvert\mathrm{TFD}_x(n,k)\rvert}\right)$ where α is the order of the information with $\alpha \geq 2$.	Minimize R_{NDV_α}
Energy concentration [68, 69, 70]	$CM = \frac{1}{\sum_n\sum_k \lvert\overline{\mathrm{TFD}_x(n,k)}\rvert}$ where $\overline{\mathrm{TFD}_x(n,k)} = \frac{\mathrm{TFD}_x(n,k)}{\sqrt{\sum_n\sum_k \lvert\mathrm{TFD}_x(n,k)\rvert^2}}$	Maximize CM
Stankovic measure [73]	$S_\beta = \left(\sum_n\sum_k \lvert\mathrm{TFD}_x(n,k)\rvert^{\frac{1}{\beta}}\right)^\beta$ $\beta = 4$: the smallest integer providing useful informative measure for the large class of the investigated signals	Minimize S_β

Continued on next page

Table 4.2: Objective performance measures used to assess TFDs and set their optimal smoothing parameters. (Continued)

The normalized instantaneous resolution [74, 66, 67]	$$NIR(t) = 1 - \frac{1}{3}\left(\frac{A_S(t)}{A_M(t)} + \frac{1}{2}\frac{A_X(t)}{A_M(t)} + \left(1 - D(t)\right)\right)$$ where $$D(t) = 1 - \frac{V_{i_1}(t) + V_{i_2}(t)}{2\left(f_{i_2}(t) - f_{i_1}(t)\right)}$$ Fig. 4.3 that displays the TFD of a signal $z(t)$ at the instant $(t = t_0)$. Two criteria are inspected. First, the average crossterms amplitude $A_X(t_0)$ and the average sidelobes amplitude $A_S(t_0)$=$\left(A_{S_1}(t_0) + A_{S_2}(t_0)\right)/2$ should be much smaller than the average mainlobes amplitude $A_M(t_0)$=$\left(A_{M_1}(t_0) + A_{M_2}(t_0)\right)/2$. Second, the instantaneous bandwidths $V_{i_1}(t_0)$ and $V_{i_2}(t_0)$ around the IFs $f_{i_1}(t_0)$ and $f_{i_2}(t_0)$ should be as narrow as possible. An overall measure NIR is taken to be the median of the instantaneous measures $NIR(t)$ corresponding to different time slices in the relevant sections of the signals.	The value of the NIR will be close to one for good performing TFDs and zero for poor performing ones (TFDs with large interference terms and components poorly resolved).
Reinhold measure [75]	NIR demands accurate detection for the signal components and a maximum of two components at any time instant with approximately equal amplitudes. The Reinhold measure extends the NIR by relaxing the equal amplitudes restriction. It employs an adaptive detection algorithm to identify the signal components regardless of their IF complexity and amplitude differences.	The value of the RM will be close to one for good performing TFDs and zero for poor performing ones.

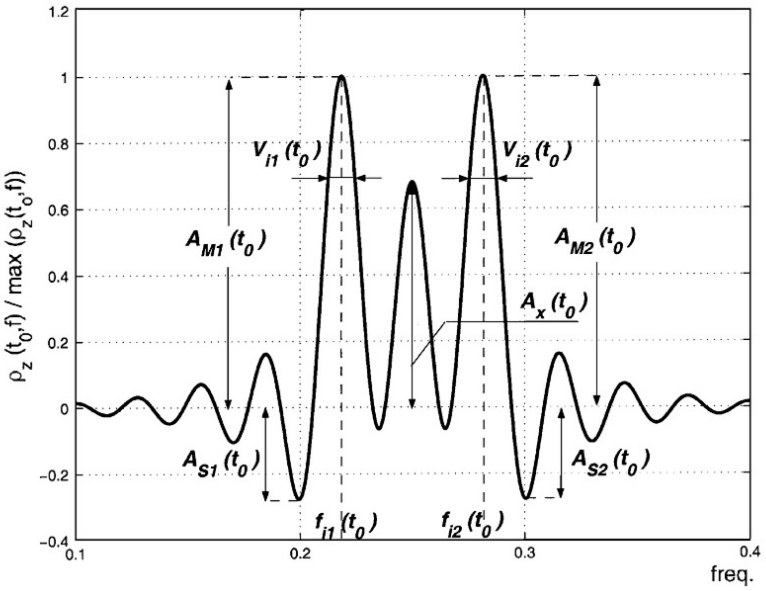

FIG. 4.3: Slice of a TFD of a two-component FM signal taken at time instant $t = t_0$ (adopted from [74]).

4.4 The proposed TF readability enhancement method

Our main interest is to improve concentration performances of the KCS TFDs that are already recognized by their high resolution and crossterms' rejection [63, 66, 67]. For this purpose, we propose a low-complexity enhancement method that includes eight steps as reported in Fig. 4.4.

4.4.1 Optimized KCS-TFDs (OKCSDs)

First, a Hilbert transform is applied so that to provide the analytic signal from the real-valued samples of the input signal. This is a common operation in time-frequency signal analysis that allows to suppress components with negative frequencies and interferences between positive and negative frequencies as well.

Then, the time-lag KCS TFDs are generated with their optimal tuning parameters being automatically selected using the energy concentration measure that does not require any setting. Applied to a large class of real-life and synthetic signals, the CM and the Stankovic measure with a parameter β have proved their ability to classify the different time-frequency representations in the right order of increasing performance. This constitutes a simple, fast and valuable quantitative tool for TFRs optimization especially for the KCSDs that have an extremely interesting practical advantage since their adjustment is performed by simply changing a single parameter. However, the seven metrics reported in Table 4.2 are all used throughout this paper for

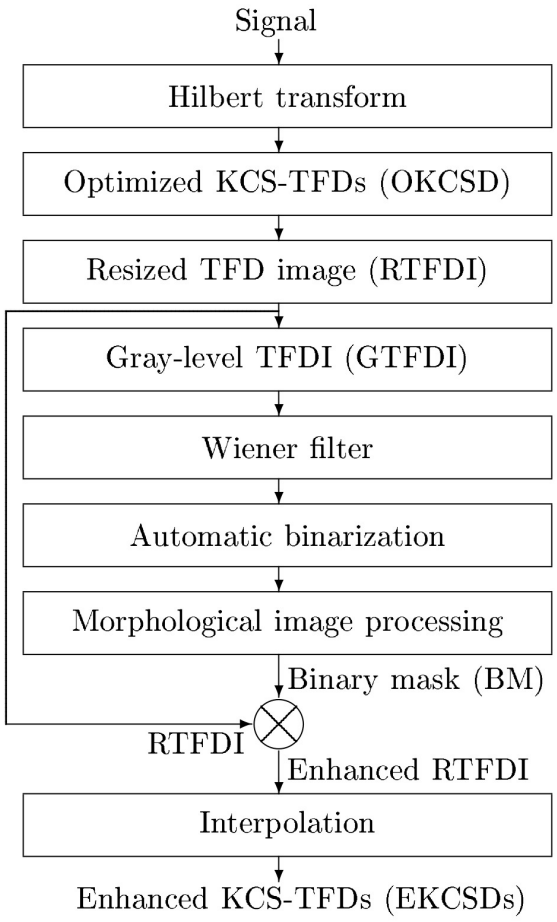

FIG. 4.4: Block diagram of the proposed method for enhanced KCS-based distributions.

performance comparison purposes. More precisely, by controlling the volume under the optimal KCS kernel, the parameter C for the CBD and the SCBD, and γ for the PCBD controls the tradeoff between crossterms suppresion and autoterms smearing while the most convenient value of kernel volume is application specific.

In order to reduce the processing complexity and improve the processing speed without loosing the main information from the original TFDs, the optimized KCS-TFDs, denoted by OKCSD, are resized by a scale S ($0<S\leq 1$) using simply nearest neighbor interpolation. Then, the resized TFD image (RTFDI) is converted into a grayscale image, denoted by GTFDI, while color information is partially recovered at the end by a simple masking.

4.4.2 Wiener filtering

The next step consists of Wiener filtering [82, 83] that is applied to the gray-level TFDI (GTFDI). Commonly used for image enhancement, the purpose of this last operation is to reduce the noise, typically assumed to be additive, without destroying the image's details. Wiener uses a pixel-wise adaptive technique based on statistics approximate from a local neighborhood of every pixel. In other words, it minimizes the overall mean square error in the process of inverse filtering and noise smoothing. The Wiener filtering is a linear estimation of the original image. The approach is based on a stochastic framework. The orthogonality principle implies that the Wiener filter in Fourier domain can be expressed as follows [83]

$$W(f_1,f_2) = \frac{H^*(f_1,f_2)S_{xx}(f_1,f_2)}{|H(f_1,f_2)|^2 S_{xx}(f_1,f_2)+S_{\eta\eta}(f_1,f_2)} \tag{4.4}$$

or equivalently

$$W(f_1,f_2) = \frac{H^*(f_1,f_2)}{|H(f_1,f_2)|^2+\frac{S_{\eta\eta}(f_1,f_2)}{S_{xx}(f_1,f_2)}} \tag{4.5}$$

where $S_{xx}(f_1,f_2)$ and $S_{\eta\eta}(f_1,f_2)$ are respectively power spectra of the original image and the additive noise, and $H(f_1,f_2)$ is the blurring filter. For practical applications, the power spectrum of the undegraded image and the power spectrum of the noise are not typically available. So, the power spectrum ratio is replaced by a parameter K whose optimal value must be experimentally determined [84]

$$W(f_1,f_2) = \frac{H^*(f_1,f_2)}{|H(f_1,f_2)|^2+K} \tag{4.6}$$

If K is too high, the restored image is very smoothed. If K is too small, the effect of the correction term in the denominator of the filter is insignificant. Using Wiener filter provides superior denoising results compared to the traditional filters.

4.4.3 Binarization and morphological processing

The filtered GTFDI is converted into a binary image. The latter is the simplest type of images and has only two intensity values, "0" (background) and "1" (signal component). In order to create a binary image from a gray-level image, a thresholding operation must be performed. For the purpose of this paper, we use the so-called Otsu method [85]. It can be summarized as follows

Step 1: Compute the histogram of the filtered GTFDI. Recall that a histogram is a probability distribution of the observed gray values $i = 1, ..., l$ (l is the image maximum gray level):

$p(i) = \frac{n_i}{n}$

That is, the number of pixels n_i having greyscale intensity i as a fraction of the total number of pixels n.

Step 2: Calculate the foreground and background variances for a single threshold (T),

- Calculate the weights of the foreground pixels and background pixels:

$$W_F(T) = \sum_{i=T+1}^{l} p(i) \text{ and } W_B(T) = \sum_{i=1}^{T} p(i)$$

- Calculate the mean of the foreground pixels and background pixels:

$$\mu_F(T) = \sum_{i=T+1}^{l} \frac{i\ p(i)}{W_F(T)} \text{ and } \mu_B(T) = \sum_{i=1}^{T} \frac{i\ p(i)}{W_B(T)}$$

$\mu_F(T)$ be the mean of all pixels greater than the threshold and $\mu_B(T)$ be the mean of all pixels less than the threshold.

Step 3: Calculate the "Between-class variance": $\sigma^2(T) = W_B(T)W_F(T)\left[\mu_B(T) - \mu_F(T)\right]^2$

The optimal threshold T is the one that maximizes the between-class variance.

The Otsu threshold is a number in the range [0, 1]. It is automatically calculated from the filtered GTFDI to be used as a sensitivity factor for adaptive thresholding using the local mean intensity around the neighborhood of the pixel [86]. A high value leads to thresholding more pixels as foreground (signal component). The goal of this method is to create a binary representation of the filtered GTFD image such that to classify each pixel into one of two categories: "signal component" or "background". In the context of our enhancement approach, the background category corresponds to the sidelobes, crossterms and background noise. Other methods for automatic thresholding can be used [84, 87].

After binarization, we perform the morphological image processing. The latter deals with tools for extracting image components that are useful in shape representation and description. In this study, the selected methodology of morphological processing is as follows

1) In order to resolve the loss of connectivity, we set "0" valued pixels to "1" if they have two nonzero neighbors that are not connected.

2) As a result of the thresholding, some unwanted pixels would appear as noise in the resulting image. To remove these unwanted objects, we used area open (bwareaopen) operation [88].

3) We apply the morphological thinning algorithm [89] (also called skeletonizing). Thinning can convert the object (the component) to an archetypical stick figure, preserve the connectivity, respect the topological properties of the shape and simplify the shape [89, 90].

The result of the morphological operations is a binary image, called BM for binary mask, where the IF of the component is indicated as a white line ("1" valued pixels), while the rest of the area appears in black (zero-valued pixels).

4.4.4 Enhanced KCSDs

The resized TFD-based image RTFDI is masked by the generated mask BM so that

$$\text{Enhanced RTFDI} = \text{BM} \times \text{RTFDI} \tag{4.7}$$

It is important to note that, since the last four operations in Fig. 4.4 are applied to the resized image, much lower computational cost is required. On the other hand, the multiplication in (4.7) is done pointwise. However, since the binary mask generated from the original compact support KCSD is already zero-valued outside the compact set, the number of multiplication points that need computation is considerably reduced. This feature makes the proposed enhancement method more suitable for the KCS-based distributions rather than the other best-known time-frequency representations. At the end, the size of the original TFD is recovered by a simple interpolation using the same scale S and the enhanced distributions, referred to as EKCSDs, are obtained.

It is shown in the next section that by considering as images the KCSDs of a signal corrupted by noise, the proposed method overcomes the original TFDs' drawbacks while preserving their useful properties. In particular, the time-lag KCS-TFDs provide the best tradeoff between highest autoterm resolution and interference rejection [63]. This feature allows to select the best threshold that separates the signal components from the background and crossterms, and so to perform the best automatic binarization, which is a very important step in our approach. In the case of noisy signals, the Wiener filter helps as well in convenient threshold selection. On another hand, the

width and shape of components produced by the KCSDs are more appropriate for the morphological image processing proposed in this paper.

4.5 Performance evaluation based on concentration and resolution measures

4.5.1 Example 1: Sum of two linear and nonlinear FM components

In the first example, we deal with a multicomponent synthetic signal of duration T=256 sec composed of a linear FM and a sinusoidal FM such that $f(t=1)=0.4$ Hz; $f(t=256)=0.3$ Hz for the linear chirp component and $f(t=1)=f(t=256)=0.1$ Hz; $f(t=128)=0.3$ Hz for the nonlinear FM component. Fig. 4.5 shows the obtained TF diagrams using the original CBD, SCBD, PCBD and their enhanced versions namely, ECBD, ESCBD and EPCBD using the proposed image processing-based method. It is obvious that the enhanced KCSDs produce more peaky plots that are practically interference-free and are characterized by much better concentration and more separation of components.

TABLE 4.3: Objective performance measures obtained from the original KCSDs and the enhanced ones of the signal of example 1.

TFD	R_{NSE_3}	R_{NDV_3}	$RN(\times 10^{-4})$	$S_4(\times 10^{-14})$	$CM(\times 10^{-3})$	NIR	RM
CBD (C=55.98)	-7.8782	-7.8782	1.427	415145	9.13	0.9213	0.9314
ECBD (S=0.5)	-8.3421	-8.3421	24	0.39697	45.88	0.9972	0.9872
SCBD (C=55.07)	-7.9032	-7.9031	1.448	406344	9.17	0.9217	0.9342
ESCBD (S=0.5)	-8.3687	-8.3687	24.445	0.41331	45.99	0.9972	0.9872
PCBD (γ=19)	-8.9664	-8.9664	2.326	956762	9.83	0.9214	0.9247
EPCBD (S=0.5)	-9.5464	-9.5464	30.744	0.75173	48.94	0.9983	0.9862
Percentage (%) of increase or decrease	> 5	> 5	> 12×10^2	> 99	> 397	> 7.6	> 5.3

In order to provide an objective assessment, we record in Table 4.3 the R_{NSE_3}, R_{NDV_3}, RN, S_4, CM, NIR and RM values realized by the investigated distributions. As expected, the enhanced KCSDs result on lower values of the R_{NSE_3}, R_{NDV_3} and the Stankovic measures and higher values of the RN, CM, NIR and RM measures compared to the original distributions. On the other hand, from concentration and interference suppression point of view, the enhanced PCBD with a tuning parameter $\gamma = 19$ and $S = 0.5$ is selected as the optimal representation of the signal of example 1 yielding to the best time-frequency localization.

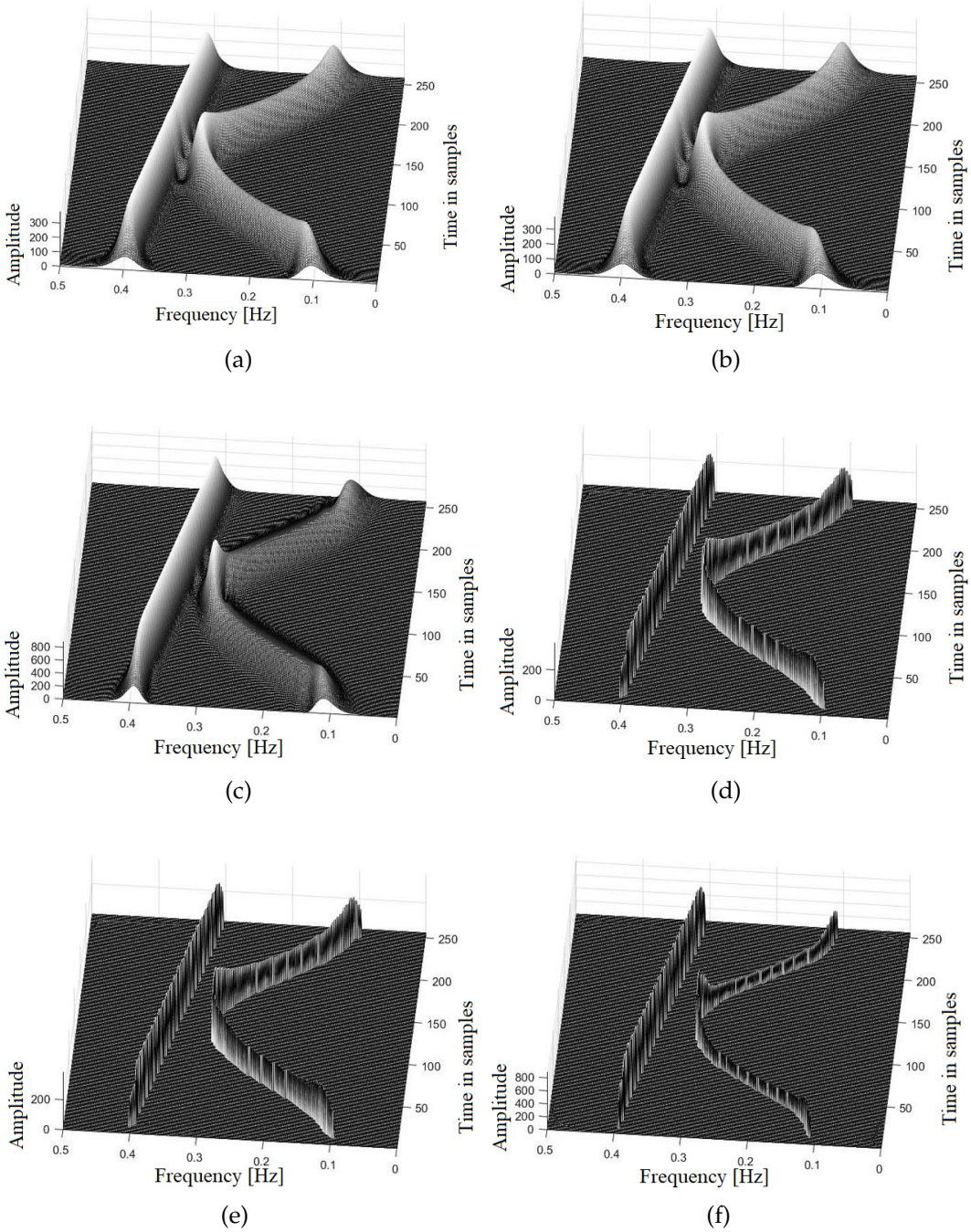

FIG. 4.5: The original KCSDs and the enhanced ones of a signal composed of a linear and a nonlinear chirps. (a) CBD (C=55.98), (b) SCBD (C=55.07), (c) PCBD (γ=19), (d) ECBD (S=0.5), (e) ES-CBD (S=0.5) and (f) EPCBD (S=0.5).

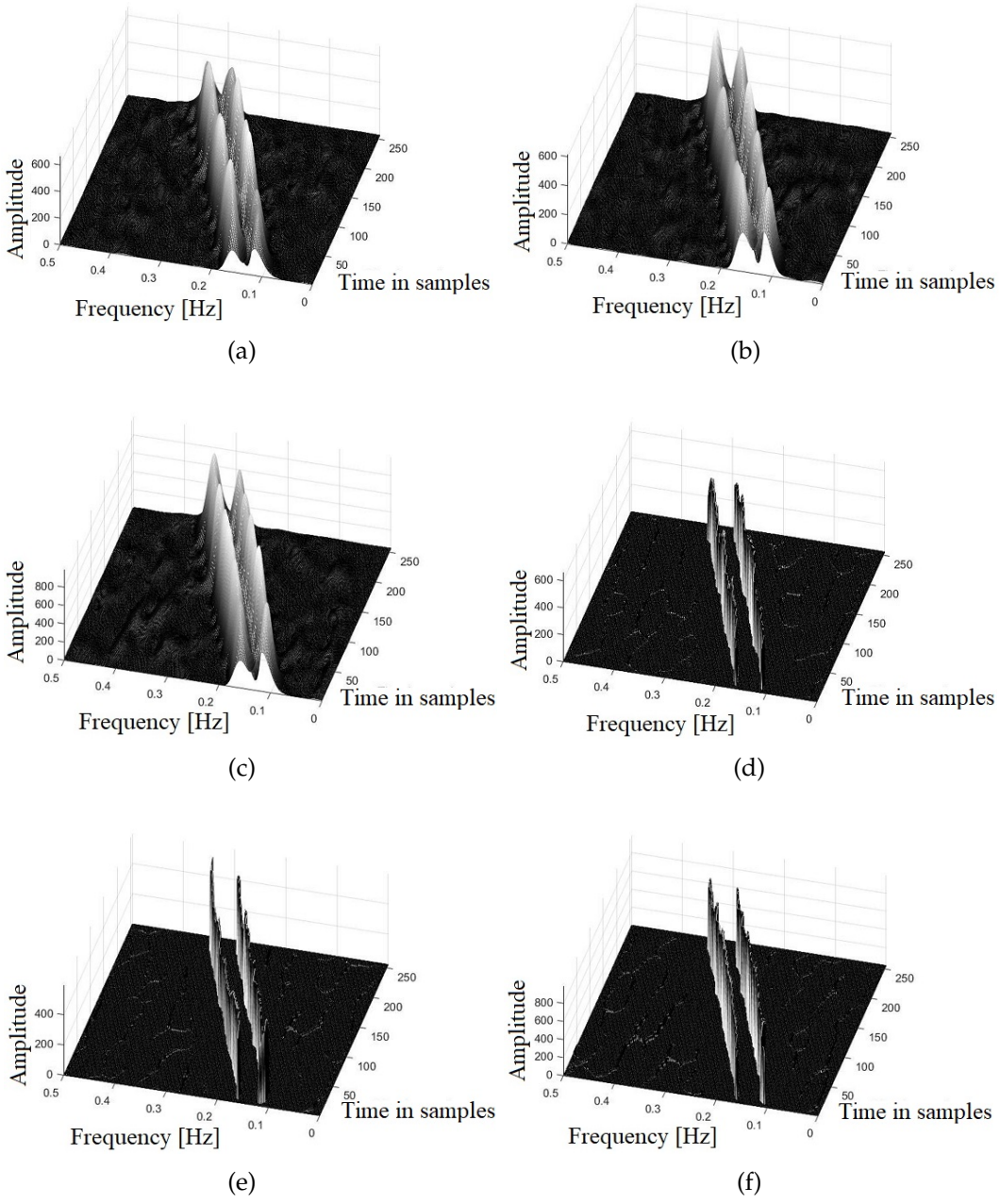

FIG. 4.6: The original KCSDs and their enhanced versions of a signal composed of two very closely spaced parallel linear chirps; embedded in 10 dB AWGN. (a) CBD (C=30.48), (b) SCBD (C=29.60), (c) PCBD (γ=32), (d) ECBD (S=0.5), (e) ESCBD (S=0.5) and (f) EPCBD (S=0.5).

4.5.2 Example 2: Sum of two very closely spaced parallel linear FMs embedded in noise

In order to check the effect of additive noise, we consider a multicomponent signal of length 256 that consists of two very closely spaced parallel linear FMs with frequencies increasing from 0.1 to 0.3 Hz and from 0.15 to 0.35 Hz, respectively. Then, we embed the signal in an additive white Gaussian noise (AWGN) with signal-to-noise ratio (SNR) of 10 dB. The time-frequency plots of Fig. 4.6 indicate that the enhanced CBD, SCBD and PCBD produce much cleaner TF diagrams compared to the original distributions. The two time-varying FM components are best concentrated in their respective frequency ranges while the background noise is greatly reduced.

TABLE 4.4: Parameters of the time slices of the original and enhanced KCSDs of the signal of example 2 computed at t_0=128 sec (SNR=10 dB).

TFD	A_{M_1}	A_{M_2}	A_X	A_{S_1}	A_{S_2}	f_{i_1}	f_{i_2}	V_{i_1}	V_{i_2}
CBD (C=30.48)	1	0.9552	0.2455	0.0172	0.0167	0.1988	0.2500	0.0165	0.0151
ECBD (S=0.5)	1	0.9350	0	0	0	0.1988	0.2520	0.0012	0.0009
SCBD (C=29.60)	1	0.7890	0.3089	0.0054	0.0034	0.1988	0.2520	0.0171	0.0120
ESCBD (S=0.5)	1	0.7308	0	0	0	0.1988	0.2559	0.0012	0.0001
PCBD (γ=32)	0.9456	1	0.2764	0.0078	0.0104	0.1988	0.2500	0.0170	0.0168
EPCBD (S=0.5)	1	0.9995	0	0	0	0.1988	0.2520	0.0011	0.0011
Percentage of minimum improvement (%)	/	/	100	100	100	/	/	> 92	> 93

When analyzing multicomponent signals, the TFD's performance does not depend on energy concentration solely but those parameters that affect resolution as well, reflecting how much the induced distribution is able to separate two closely spaced signal's autoterms when visualized in the time-frequency plane. This property requires analysis of time slices as shown in the plot of Fig. 4.3 that displays the TFD of a signal $z(t)$ at the instant $(t = t_0)$. It follows that readability enhancement allows more accurate estimation of the exact number of components and their true instantaneous frequency laws.

In order to evaluate more deeply the performance of the enhanced KCSDs, we inspect the time slice plots of Fig. 4.7 obtained at the time instant t_0=128 sec; the middle of the signal duration. The most important parameters extracted from these plots are recorded in Table 4.4. As expected, the obtained results indicate that the enhanced distributions have the narrowest instantaneous bandwidths V_{i_1} and V_{i_2}, which means that the energy of each component is highly concentrated close to the path of its instantaneous frequency. This provides the best performance of the recovered representations thanks to the Wiener filtering, binarization and morphological image processing applied to the TF images generated from the original time-lag KCSDs. On the other hand, even if the two components are very closely spaced in presence of noise, the EKCSDs are able to distinguish between the two linear chirps by reducing to the best the crossterms, the sidelobes and the noise levels as well.

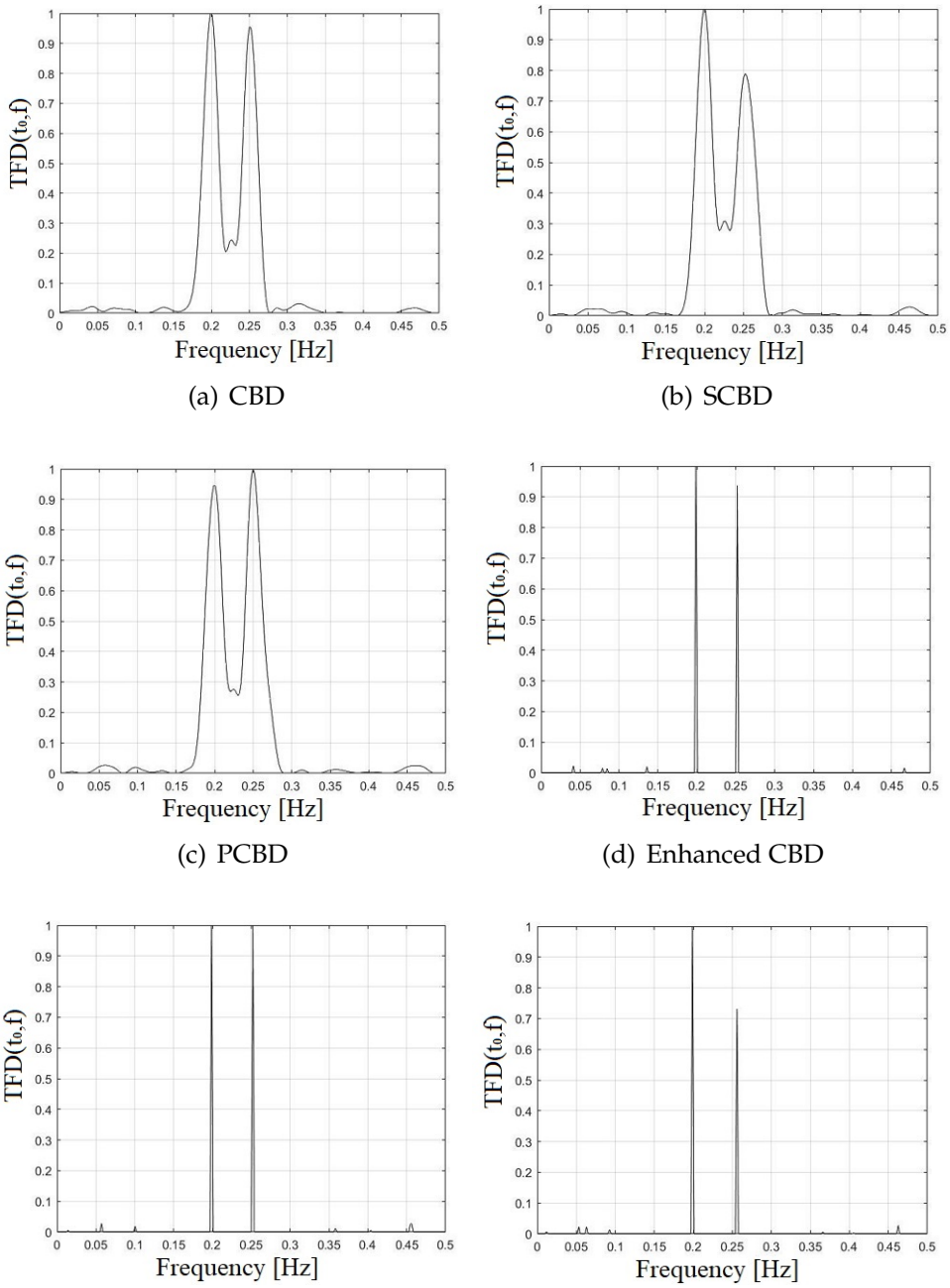

(a) CBD (b) SCBD

(c) PCBD (d) Enhanced CBD

(e) Enhanced SCBD (f) Enhanced PCBD

FIG. 4.7: Normalized slices of the original and enhanced KCSDs plotted at t_0=128 sec of two closely spaced linear chirps embedded in 10 dB AWGN (example 2).

Another important overall performance indicator concerns the accuracy of instantaneous frequency estimation from the TF plots. Fig. 4.8 shows that the actual IF laws are still been best estimated from the enhanced KCSDs peaks even with a scale S=0.5 reducing considerably the processing time.

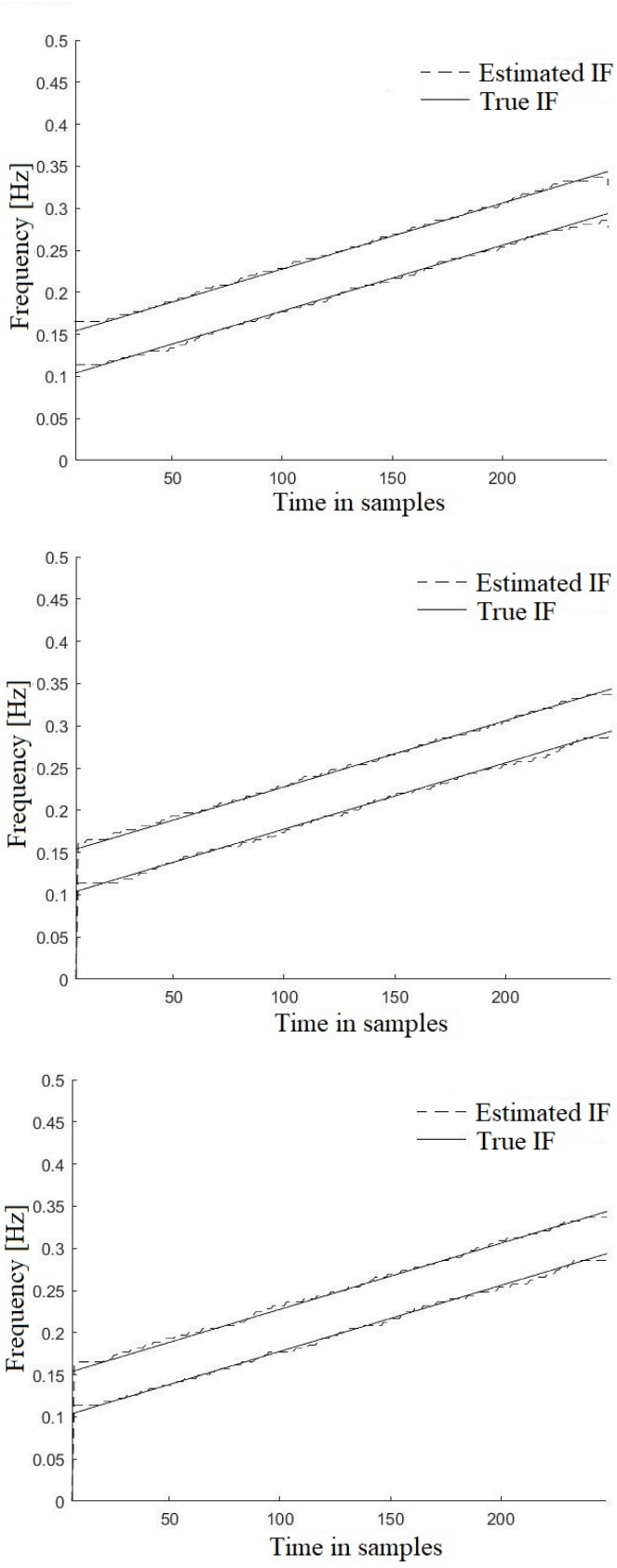

FIG. 4.8: Comparison of the estimated IF from the enhanced KCSDs and the true IF laws of two closely spaced linear chirps embedded in 10 dB AWGN (example 2). ECBD (S=0.5), ESCBD (S=0.5), and EPCBD (S=0.5) from top to bottom figure, respectively.

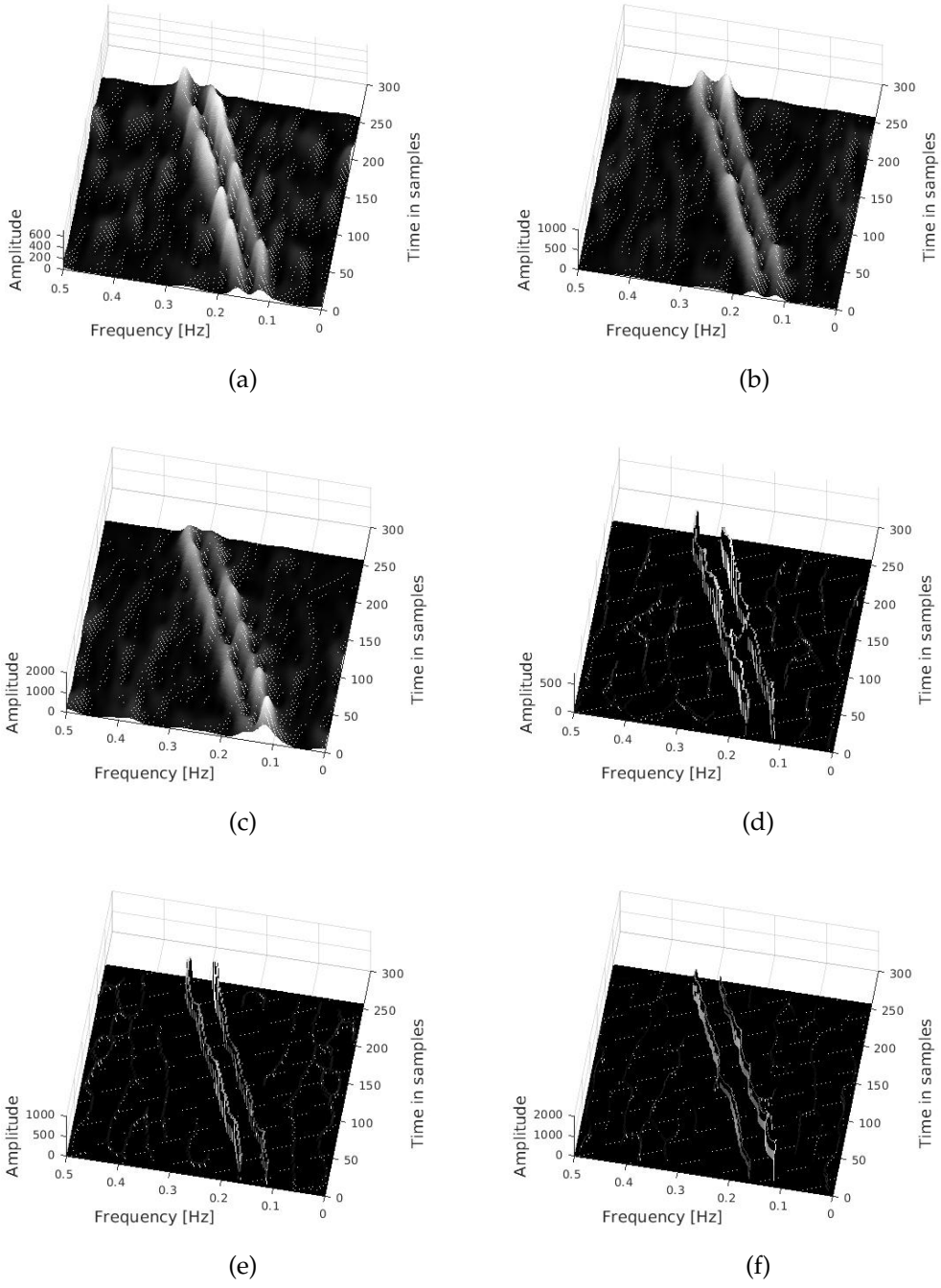

FIG. 4.9: The original KCSDs and their enhanced versions of a signal composed of two very closely spaced parallel linear chirps; embedded in -2 dB AWGN. (a) CBD (C=30.03), (b) SCBD (C=31.03), (c) PCBD (γ=33), (d) ECBD (S=0.5), (e) ESCBD (S=0.5) and (f) EPCBD (S=0.5).

In the same context, we inspect again the previous signal at bad transmission conditions (SNR = -2 dB). This means that the signal is buried under the

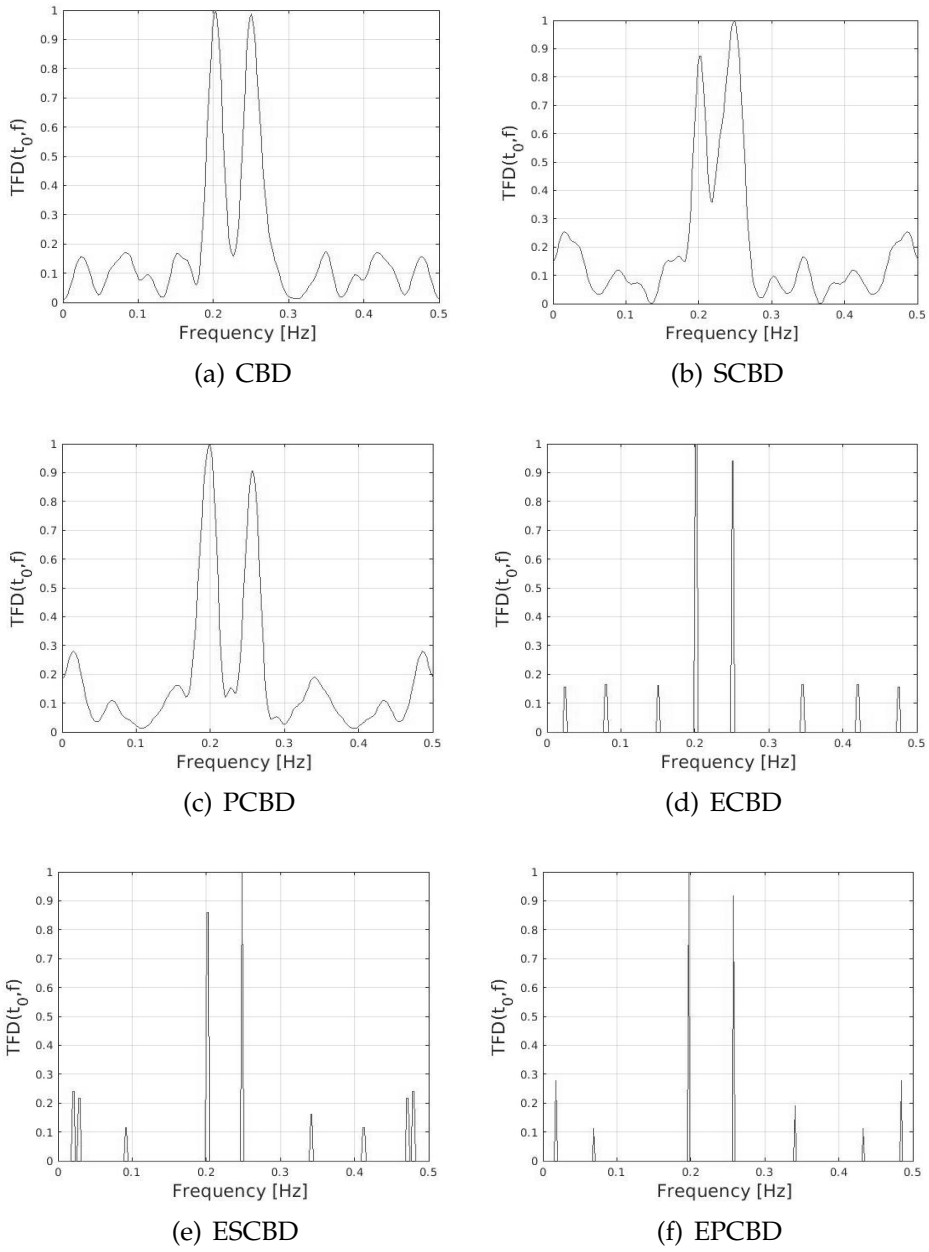

(a) CBD (b) SCBD

(c) PCBD (d) ECBD

(e) ESCBD (f) EPCBD

FIG. 4.10: Normalized slices of the original and enhanced KCSDs plotted at t_0=128 sec of two closely spaced linear chirps embedded in -2 dB AWGN.

noise and cannot be recovered by the narrow-band receiver. Fig. 4.9 shows the obtained TF diagrams using the original and enhanced KCSDs. The time slice plots at $t_0 = 128$ sec are depicted in Fig. 4.10 with their main parameters been recorded in Table 4.5.

From Fig. 4.9, we see clearly that the EKCSDs generate the most appealing plots and provide the best components separation even at negative SNR. This is a direct result of the high decrease in the instantaneous bandwidths,

TABLE 4.5: Parameters of the time slices of the original and enhanced KCSDs of the signal of example 2 computed at t_0=128 sec (SNR= -2 dB).

TFD	A_M	A_X	A_S	f_{i_1}	f_{i_2}	V_{i_1}	V_{i_2}	RM
CBD (C=30.03)	0.9939	-0.1598	0.1722	0.2039	0.2510	0.0157	0.0196	0.8440
ECBD (S=0.5)	0.9703	0	0.1652	0.2020	0.2510	0.0039	0.0039	0.9166
SCBD (C=31.03)	0.9362	0.4812	0.2548	0.2020	0.2490	0.0196	0.0235	0.6708
ESCBD (S=0.5)	0.9294	0	0.2409	0.2020	0.2490	<0.0020	<0.0020	0.8997
PCBD (γ=33)	0.9535	0.1538	0.2801	0.2000	0.2588	0.0235	0.0196	0.7530
EPCBD (S=0.5)	0.9579	0	0.2783	0.1980	0.2588	<0.0020	<0.0020	0.9371
Percentage of minimum improvement (%)	/	100	> 0.5	/	/	> 80	> 80	> 8.6

the crossterms, sidelobes and noise amplitudes. The achieved readability enhancement is better seen from the normalized slices of Fig. 4.10 and the achieved RM measures reported in Table 4.5 revealing that the EPCBD is the best performing TFD at the time instant $t_0 = 128$ sec.

Fig. 4.11 displays the TF contour plots of the enhanced PCBD, the original one and a selection of reassignment TFRs. It is obvious that the signal components are the best resolved using the EPCBD thanks to the high achieved concentration and crossterms suppression. The RSP and the RSD, however, results on the best reduction of the sidelobes generated by the background noise.

4.5.3 Example 3: Sum of two crossing nonlinear FMs

In order to check the effect of crossing, we consider a multicomponent signal of length 256 that is composed of two intersecting sinusoidal FMs. The nonlinear components consist of an increasing and decreasing sinusoidal frequency modulated signals such that $f_1(0) = 0.2$ Hz and $f_2(0) = 0.45$ Hz, having both a period $T = 256$ sec with smallest and highest frequencies equal to 0.2 Hz and 0.45 Hz, respectively. Fig. 4.13 shows the obtained TF diagrams using the original and enhanced KCSDs using the proposed image processing-based method.

The latter are compared to the most popular reassignment TFRs as plotted in Fig. 4.12, namely, the RPWVD, the RSPWVD, the RPPD, the RSP, the RSD and the RPMHD. From visual inspection, one can see that the enhanced KCSDs produce the most appealing plots followed by the RSD and the RSP. This corresponds to better components concentration and less interference than the other distributions.

In order to provide an objective assessment, we record and plot in Fig 4.14 the R_{NSE_3}, RN, S_4, CM, NIR and RM values achieved by the investigated representations. We observe that the energy normalized Rényi entropy measure R_{NSE_3} defines the RSD and the EPCBD as the best-performing TFRs, as expected from the plots of Figs. 4.12-4.13. However, the PCBD is classified as the signal third best representation better than the ESCBD, the ECBD and the RSP.

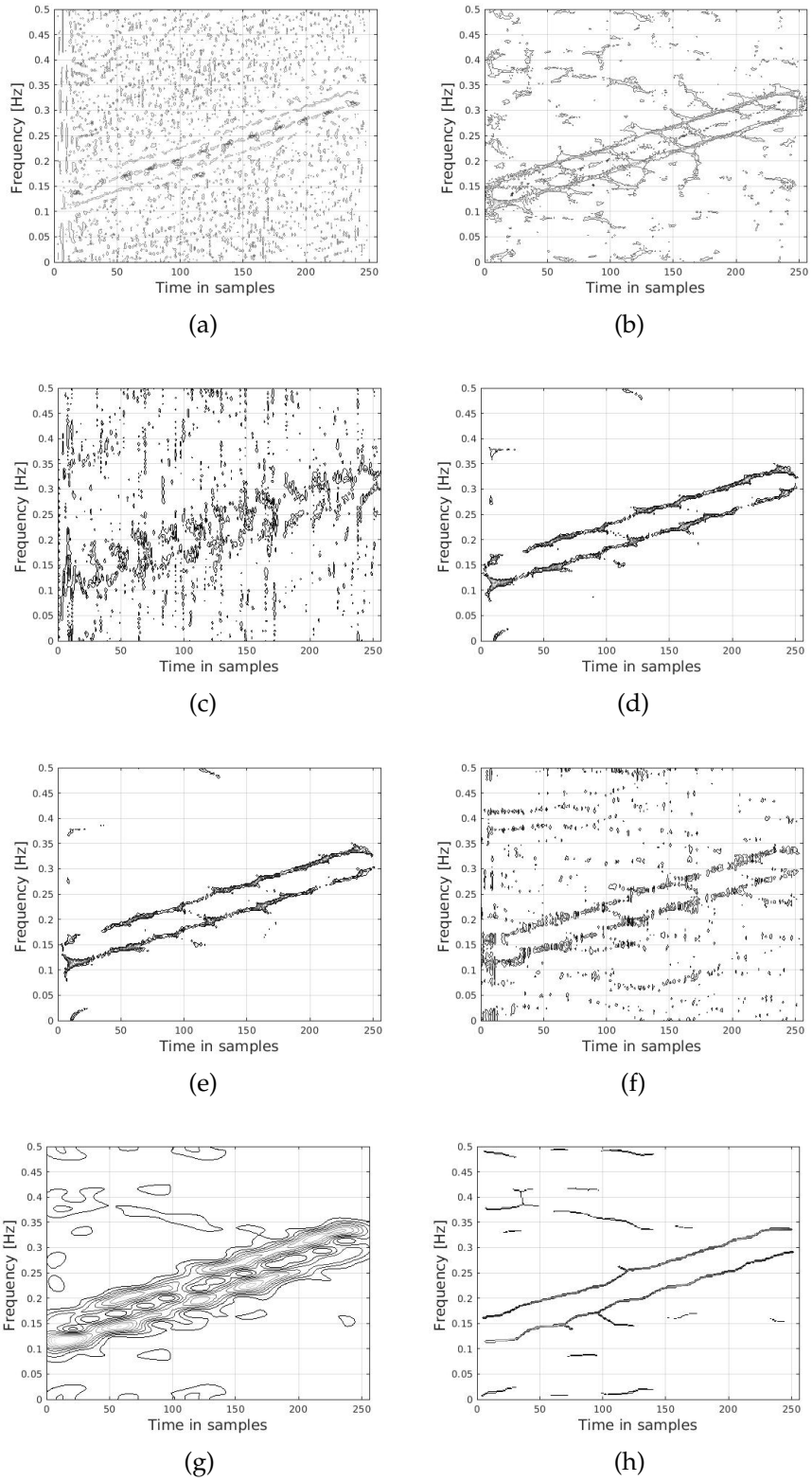

FIG. 4.11: The original PCBD, its enhanced version and a selection of reassignment TF representations of a signal composed of two very closely spaced parallel linear chirps; embedded in -2 dB AWGN. (a) RPWVD (Hamming(65)), (b) RSPWVD (Hamming(25), Hamming(65)), (c) RPPD (Hamming(65)), (d) RSP (Hamming(65)), (e) RSD (Hamming(65)), (f) RPMHD (Hamming(65)), (g) PCBD ($C = 33$) and (h) EPCBD ($S = 1$).

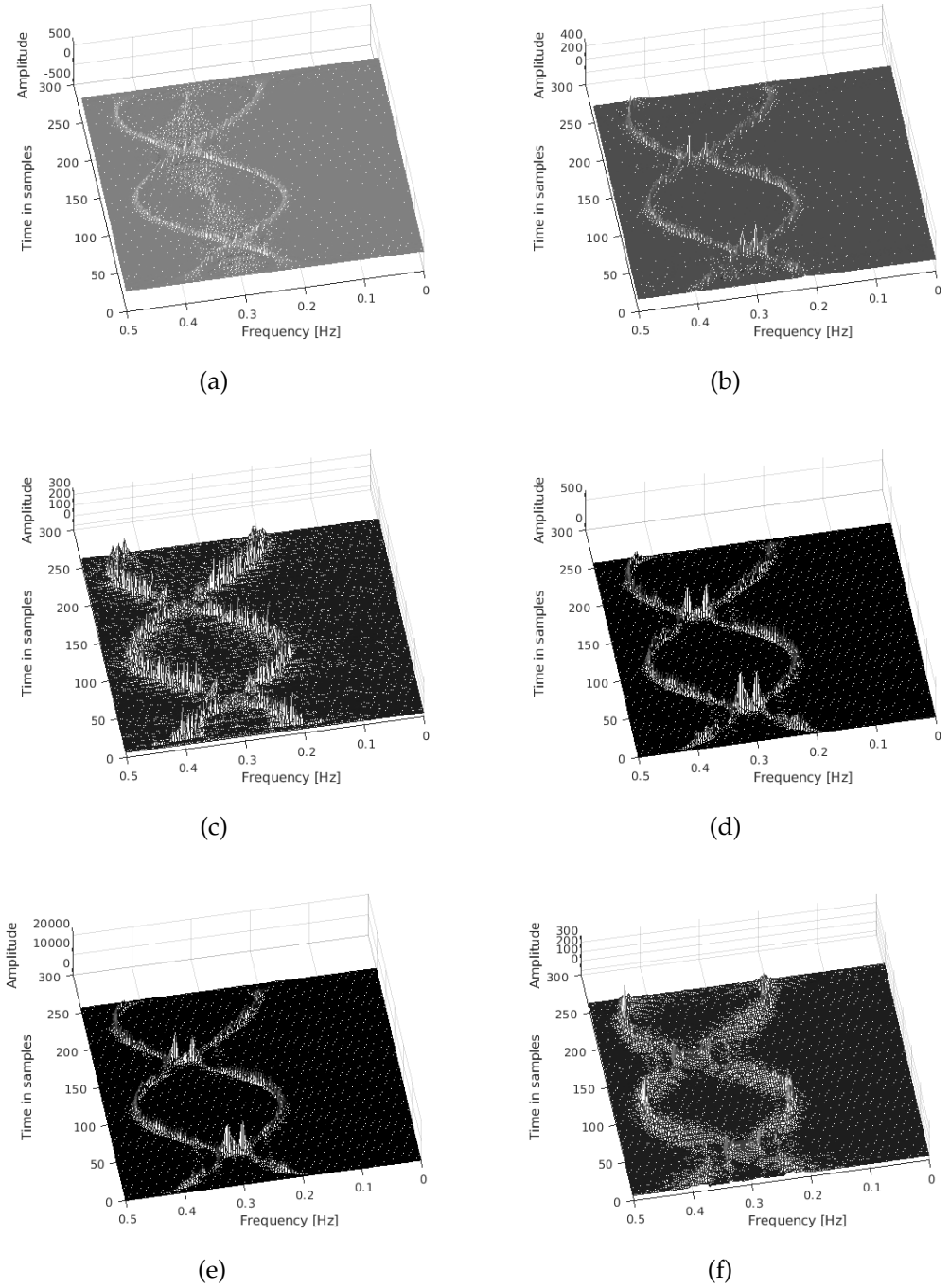

FIG. 4.12: The reassigned TFRs of the signal of example 3 (two crossing nonlinear FMs). (a) RPWVD (Hamming(65)), (b) RSPWVD (Hamming(25), Hamming(65)), (c) RPPD (Hamming(65)), (d) RSP (Hamming(65)), (e) RSD (Hamming(65)), and (f) RPMHD (Hamming(65)).

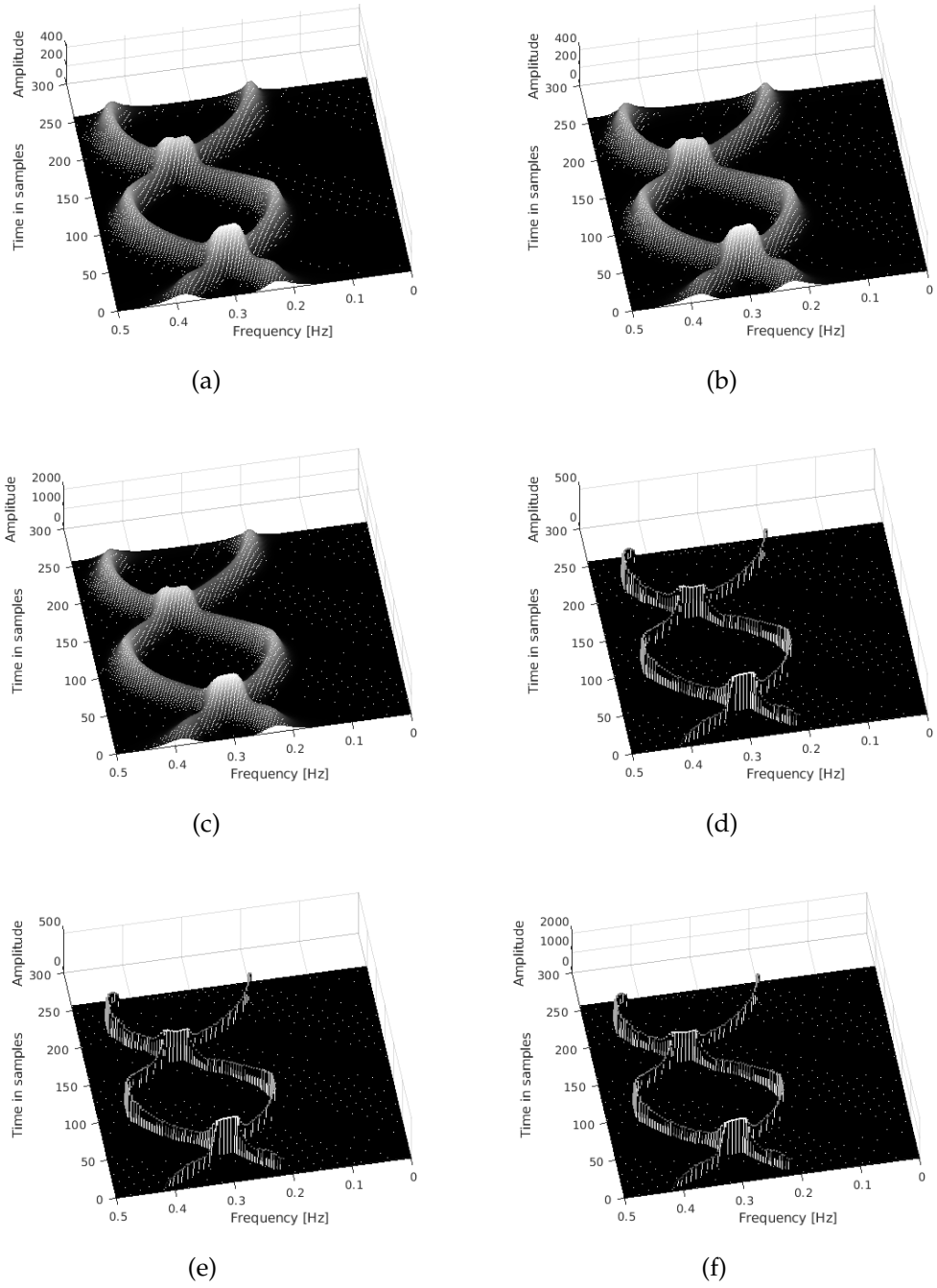

FIG. 4.13: The original KCSDs, the enhanced ones of the signal of example 3 (two crossing nonlinear FMs). (a) CBD ($C = 73.86$), (b) SCBD ($C = 72.57$), (c) PCBD ($\gamma = 74$), (d) ECBD ($S = 0.5$), (e) ESCBD ($S = 0.5$) and (f) EPCBD ($S = 0.5$).

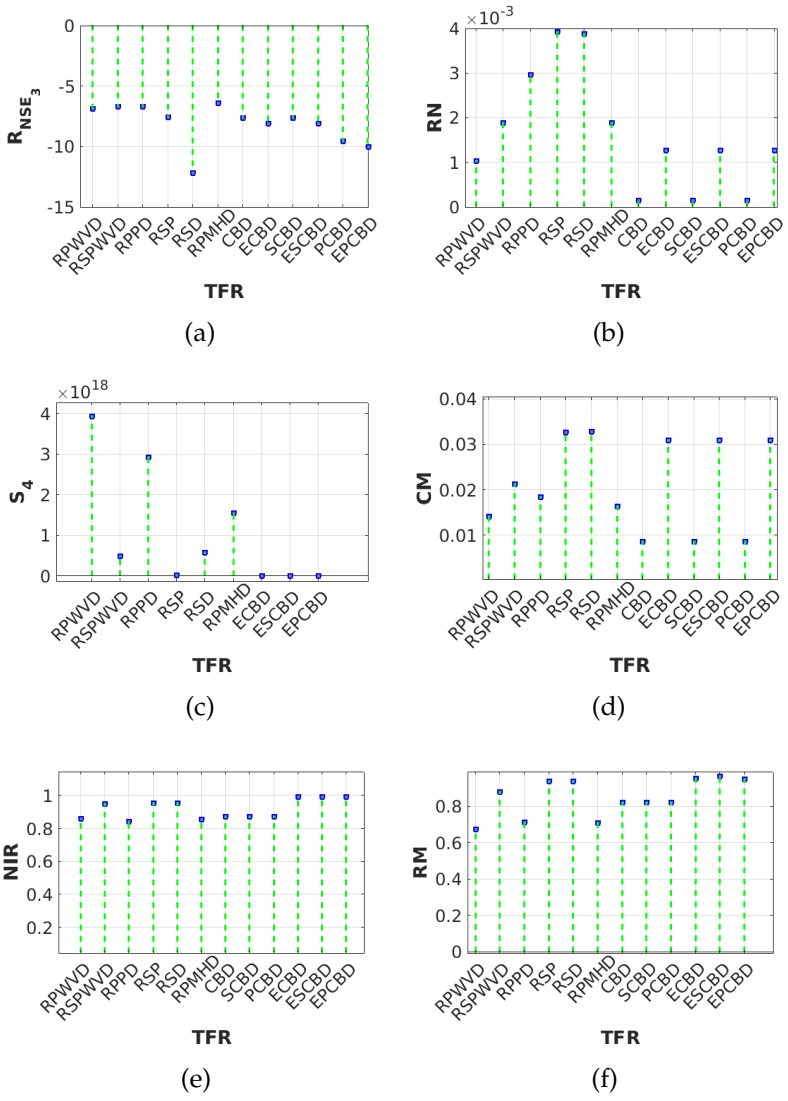

FIG. 4.14: Comparison between a selection of TFRs in representing the signal of example 3 (two crossing nonlinear FMs) using several popular objective performance measures. (a) R_{NSE_3}, (b) RN, (c) S_4, (d) CM, (e) NIR and (f) RM.

The ratio of norms measure RN is optimized using the RSP and the RSD followed by the RPPD, the RSPWVD and the RPMHD whose concentrations are better than the enhanced KCSDs. It is obvious that neither R_{NSE_3} nor RN can exactly match the foreseen results of TFRs' performances in accordance to the visual inspection of the t-f diagrams.

The CM, S_4, NIR and RM measures identify the ECBD, the ESCBD and the EPCBD as the signal best representations followed by the RSP and the RSD. The latter perform better than the RPWVD, the RPDD and the RPMHD. Hence, these measures are, in this case, the best informative ones in terms

of accurate concentration performances and interference reduction indications. This has been confirmed by a wide variety of tests involving a large class of real-life and synthetic signals as discussed in the present work and the previously conducted studies in [63, 66, 67, 91].

4.5.4 Example 4: Sum of two signals with time-varying amplitudes

In order to check the effect of time-varying amplitude, we consider a multi-component signal of length 256 that is composed of linear FM and sinusoidal FM with time-varying amplitudes. The nonlinear component consist of an increasing sinusoidal frequency modulated signal such that $f_1(1) = 0.3$ Hz and have a period $T = 135$ sec with smallest and highest frequencies equal to 0.2 Hz and 0.4 Hz, respectively, and $f(t = 1) = 0.025$ Hz; $f(t = 256) = 0.125$ Hz for the linear chirp component. Fig. 4.15 shows the obtained TF diagrams using the original and enhanced KCSDs using the proposed image processing-based method.

The latter are compared to an optimal TFD as plotted in Fig. 4.15, namely the piece-wise spline Wigner-Ville distribution (PW-WVD) [11]. The PW-WVD formulate by decomposing a standard non-stationary signal model using piece-wise linear frequency modulated (LFM) basis and by exploiting the Wigner-Ville distribution optimality for LFM signals [11]. It is more suitable to serve as a reference TFD. However, from visual inspection, one can see that the enhanced KCSDs produce the most appealing plots and are most similar to the optimal TFD.

4.5.5 Example 5: The bat echolocation signal

The third evaluation example is shown in Fig. 4.16 where the bat echolocation real-life signal [92] is represented in the time-frequency plane using the time-lag KCSDs and the enhanced ones. The parameters D and λ are both set to 2.5. The time-lag kernel's length L is set to 256. The results illustrated in Fig. 4.16 show that the proposed enhancement method provides cleaner plots. This reflects a significant improvement in the readability of the KCS distributions. Table 4.6 reports comparisons between several popular concentration-based performance measures of TFDs in representing the investigated signal.

From resulting R_{NSE_3} and R_{NDV_3} values recorded in Table 4.6, one observes that, from concentration point of view, the enhanced distributions outperform the original TFDs. We also see a significant increase in the RN and CM measures and decrease in the S_4 measure. This confirms the effectiveness of the proposed method in improving concentration of the time-lag KCS distributions. In addition, from Fig. 4.16 and Table 4.6, one can see that the proposed method with a resize scale S=0.5 achieves the best performance.

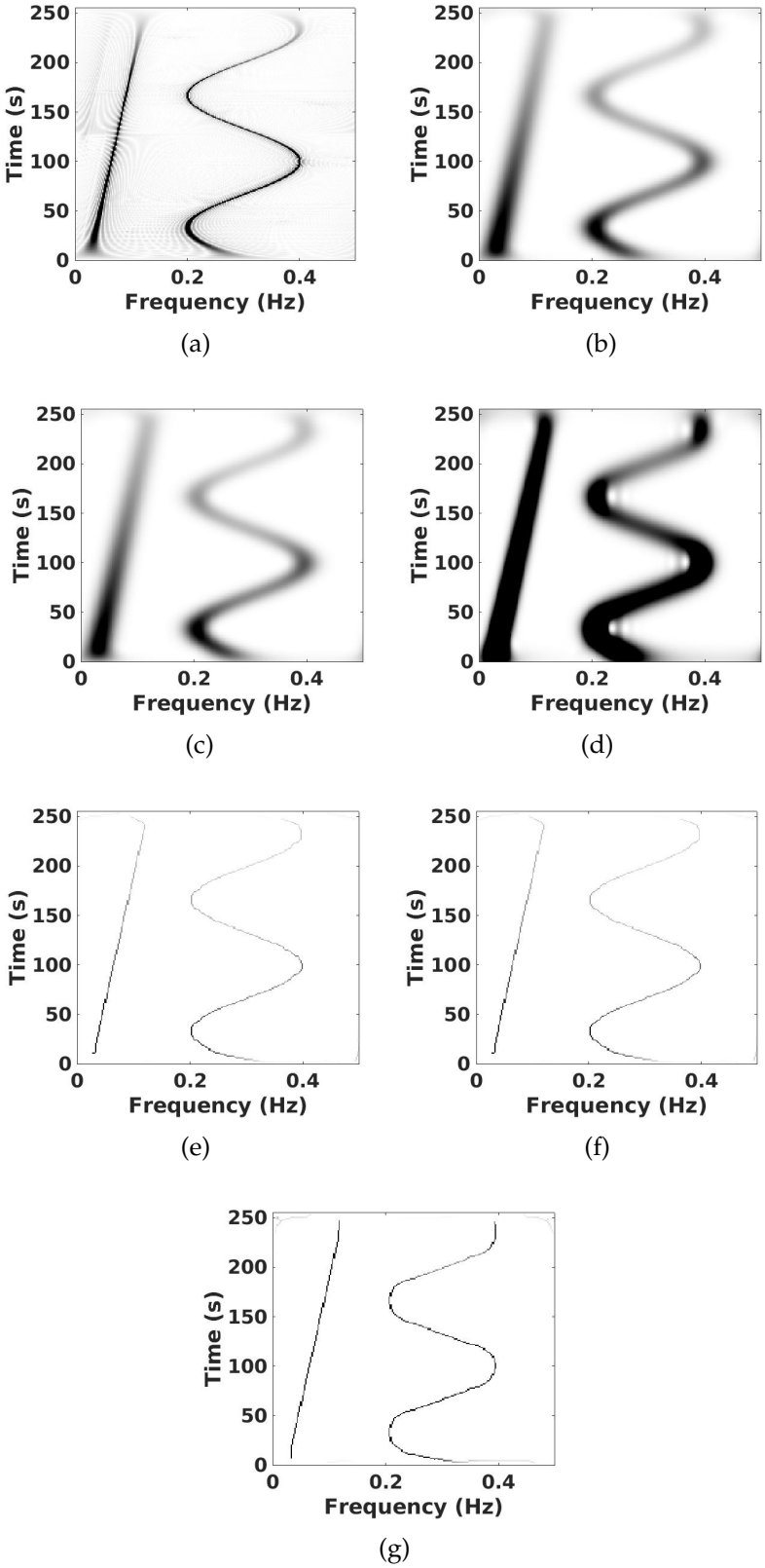

FIG. 4.15: The original KCSDs and the enhanced ones of sum of two signals with time-varying amplitudes (example 4). (a) PWWVD, (b) CBD (C=120), (c) SCBD (C=120.25), (d) PCBD (γ=50), (e) ECBD (S=0.9), (f) ESCBD (S=0.9) and (g) EPCBD (S=0.9).

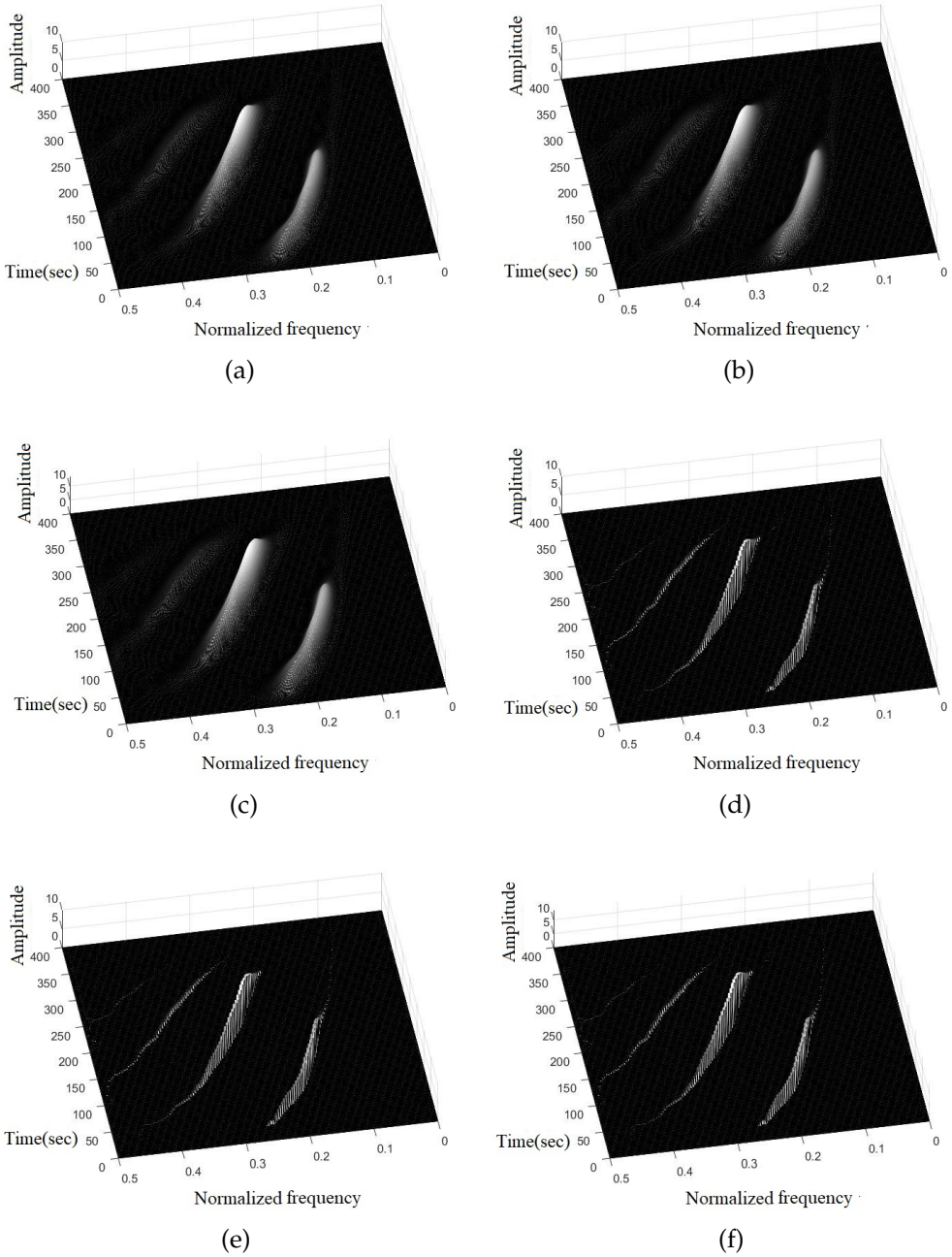

FIG. 4.16: The original KCSDs and the enhanced ones of the bat echolocation real-life signal (example 5). (a) CBD (C=25.95), (b) SCBD (C=26.27), (c) PCBD (γ=27), (d) ECBD (S=0.5), (e) ESCBD (S=0.5) and (f) EPCBD (S=0.5).

TABLE 4.6: Concentration-based performance measures obtained from the original KCSDs and the enhanced ones of the bat echolocation signal (example 5).

TFD	R_{NSE_3}	R_{NDV_3}	$RN(\times 10^{-4})$	$S_4(\times 10^{-14})$	$CM(\times 10^{-3})$
CBD (C=25.95)	-2.2161	-2.2161	3.175	23713	11.26
ECBD (S=1)	-2.6575	-2.6575	41.621	0.03922	50.48
ECBD (S=0.5)	-2.6484	-2.6484	41.627	0.03326	50.53
SCBD (C=26.27)	-2.2089	-2.2088	3.154	22988	11.27
ESCBD (S=1)	-2.6440	-2.6440	41.565	0.03861	50.46
ESCBD (S=0.5)	-2.6351	-2.6351	41.580	0.03349	50.48
PCBD (γ=27)	-2.7079	-2.7079	3.149	34125	11.22
EPCBD (S=1)	-3.1487	-3.1487	41.559	0.05628	50.45
EPCBD (S=0.5)	-3.1405	-3.1405	41.586	0.04681	50.51
Percentage (%) of increase or decrease	> 15	> 15	> 12×10^2	> 99	> 354

4.6 Application to IF estimation of MFSK signals

The objective of this section is to compare the enhanced PCBD and a selection of time-frequency representations in estimating the true IF laws of MFSK signals. The PCBD is chosen because its tuning is the simplest and the fastest since the time-lag PCB needs the setting of a single integer parameter rather than a real parameter as for the CBD and the SCBD. The established comparisons are in terms of visual inspection of the estimated IF plot and the slice of the time-frequency representation. Then, an objective study is performed based of the main-lobe width (MLW) and the performance of the IF estimator obtained from several measures. Finally, two real-life MFSK high-frequency radio communications signals are analyzed.

4.6.1 Performance evaluation of IF estimation

MFSK signals are widely used in digital communications [93, 94], radar systems [94, 95], and acoustic communications systems [96, 97, 98]. MFSK signals have constant amplitude and time-varying frequencies that change abruptly between symbols. This instantaneous variation can be described by their IF estimates. In this paper, we consider 2FSK, 4FSK, 8FSK, and 16FSK signals. The IF is estimated as the frequency with the maximum energy content in the TFD of the MFSK signal at each time instant, so that [1]

$$\widehat{f}(n) = \arg\{\max_k \mathrm{TFD}_x(n,k)\} \tag{4.8}$$

where $\widehat{f}(n)$ are the estimated IFs which correspond to the subcarrier frequencies of the signal. For discussion purposes, the IF of the enhanced PCBD for a 4FSK signal embedded in 4 dB AWGN is estimated and compared. Fig. 4.17 shows the estimated IF and the TFR slice of the corresponding signal obtained from the enhanced PCBD and the SPWVD, respectively. It is seen that the enhanced PCBD provides better accuracy of the IF estimate. For the SPWVD, distortion is observed in the IF estimate plots at some of the

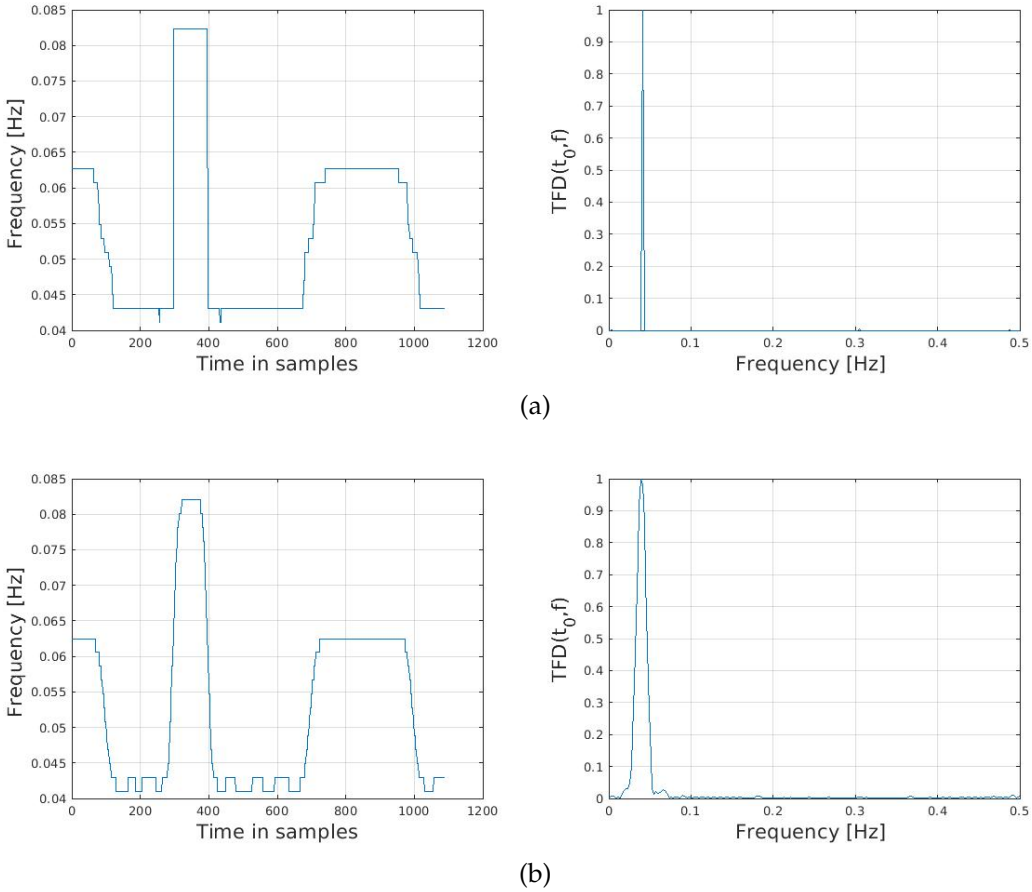

FIG. 4.17: IF and TFR slice at t_0=500 sec of a 4FSK signal using the enhanced PCBD and SPWVD at SNR of 4 dB. (a) EPCBD (γ=3, S=1): IF (left) and TFR slice (right), (b) SPWVD: IF (left) and TFR slice (right).

signal samples due to the influence of noise. The enhanced PCB distribution, however, is constantly distortion-free. Moreover, the TFR slices at t_0 = 500 sec clearly indicate that the MLW obtained from the enhanced PCBD is the narrowest. Hence, the image postprocessor improves significantly the concentration around the instantaneous frequency laws of MFSK symbols. Results confirming this statement are presented in Table 4.7 where the MLW estimates are recorded for SNR values of 4 and 10 dB.

Generally, the SNR and the signal modulation level have no significant effect on the MLW related to the enhanced PCBD. This is because the use of thinning produces the same component shape for all signals. However, it is observed that the MLW values for the enhanced PCBD are smaller than those obtained from SPWVD. Besides the MLW of the TFR slices, there is also a difference in the average sidelobe level that is much lower for the enhanced PCBD compared to SPWVD. These numerical results reveal that the proposed enhancement method improves concentration and eliminates the

TABLE 4.7: MLW values obtained from the enhanced PCBD and SPWVD at different modulation levels and SNRs.

		MLW	
SNR	Signals	Enhanced PCBD	SPWVD
4 dB	2FSK	0.0023	0.0101
	4FSK	0.0025	0.0105
	8FSK	0.0023	0.0222
	16FSK	0.0023	0.0135
10 dB	2FSK	0.0023	0.0120
	4FSK	0.0023	0.0110
	8FSK	0.0023	0.0200
	16FSK	0.0024	0.0118

best the sidelobs and crossterms and then enhances time-frequency localization of the different signal's events.

In the same context, Fig. 4.18 represents the energy density spectrum of a

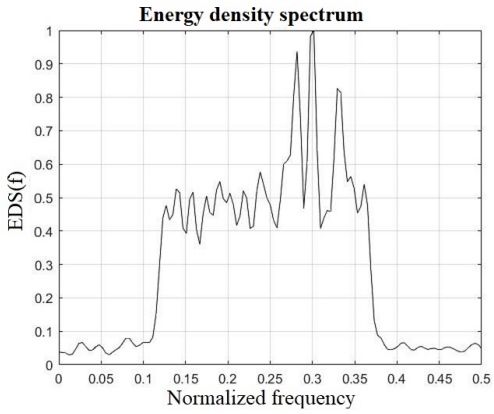

(a)

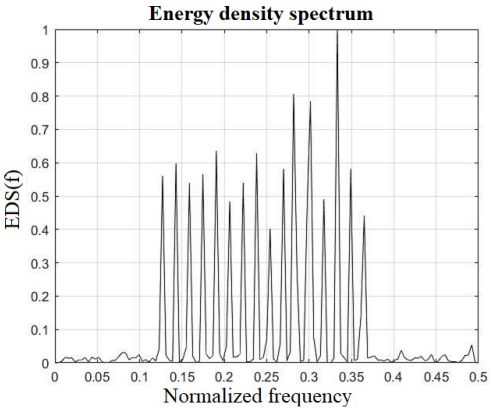

(b)

FIG. 4.18: Energy density spectrum of a 16FSK signal at SNR=10 dB. (a) PCBD (γ=4) and (b) EPCBD (S=0.8).

16FSK signal at SNR of 10 dB using the PCBD and the EPCBD. Once again, a clear and significant improvement is seen in components concentration and interference rejection. Hence, the proposed method is able to resolve very closely-spaced sinusoids confirming the results presented in Section 4.5.2.

4.6.2 Variance comparison

In order to objectively assess the performance of the enhanced PCBD and a selection of the most-used reassignment time-frequency representations in estimating the IF laws, Monte Carlo (MC) simulation-based comparisons are performed. The MFSK signals are evaluated in a zero mean and σ^2 variance AWGN channel. It is assumed that the signal components and noise are independent from each other. The mean-square error (MSE) is employed to evaluate performances by running 300 MC simulations while the SNR is varied from -1 to 12 dB with a 1 dB step. Assuming the actual instantaneous frequency for all signals been known, the MSE for the IF estimate is given by

$$\text{MSE} = \frac{1}{MN} \sum_{m=1}^{M} \sum_{n=0}^{N-1} \left(\widehat{f}(n) - f(n) \right)^2 \tag{4.9}$$

where $f(n)$ and $\widehat{f}(n)$ are the true and estimated frequencies at n^{th} instant, N is the length of the analyzed signal, and M is the total number of MC simulations. Fig. 4.19 shows the plots of IF estimate MSE with respect to SNR for 2FSK, 4FSK, 8FSK and 16FSK signals. The results indicate that the RPPD has the highest MSE while the EPCBD and the RPMHD provide the smallest MSE values. It can also be seen that, the enhanced PCBD provides, for all investigated MFSK signals, a much lower overall MSE compared to the RSD, the RSP, the RPWVD, and the RSPWVD. In addition, the EPCBD outperforms the RPMHD. In general, the MC simulation-based results reveal that the EPCBD performs the best as a blind IF estimator. The most remarkable advantage of the EPCBD is that, unlike the other best performing TFRs, there is no need of additional settings of external windows. This is done thanks to the special form of the auto-windowed time-lag KCS kernels that vanish themselves outside the compact support yielding, at the same time, to a very low computational cost. Particularly, the PCBD is recognized by its lowest numerical complexity and simplest tuning since its kernel is polynomial [63].

In order to show the enhancement on IF estimation Fig. 4.20, represent the originals TFDs and the enhanced ones using 300 MC. We can clearly see the enhancement on IF estimation of MFSK signals.

4.6.3 IF estimation of a real-life MFSK signals

In order to illustrate the practical effectiveness of the proposed method, the enhanced PCBD is applied to the analysis of two real-life communications signals in the HF band. The first signal's carrier frequency is 8.180 MHz.

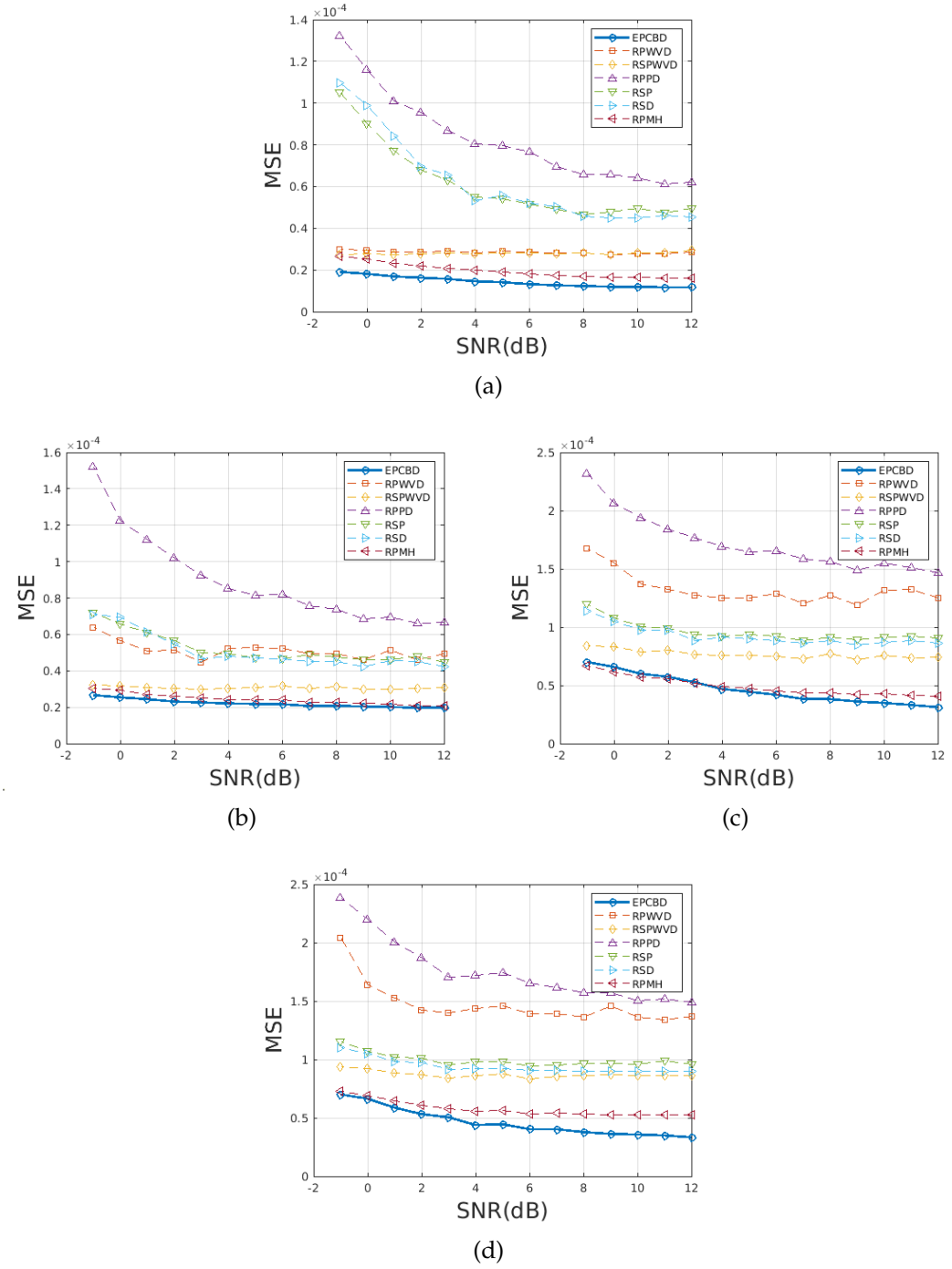

FIG. 4.19: Comparison of MSE values corresponding to IF estimates from the enhanced PCBD and a selection of reassignment TFRs with 300 MC simulations. (a) 2FSK, (b) 4FSK, (c) 8FSK, and (d) 16FSK.

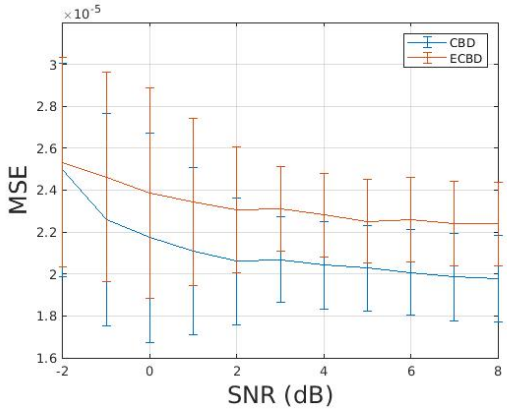

(a)

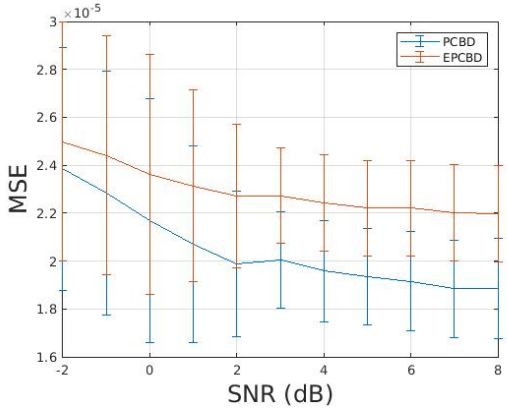

(b)

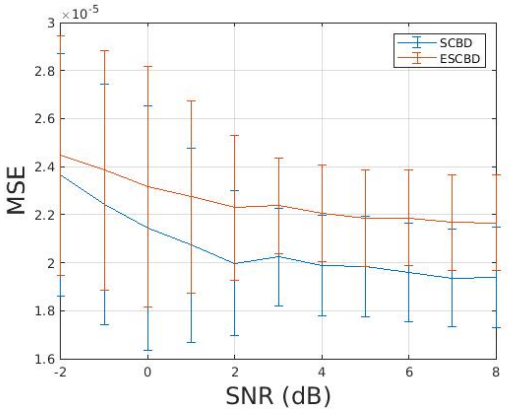

(c)

FIG. 4.20: Comparison of MSE values corresponding to IF estimates from the enhanced TFDs and the original ones with 300 MC simulations with the standard deviation displayed as well.

The time representation of this signal is depicted in Fig. 4.21(a). Fig. 4.22(a) shows the enhanced PCBD and the estimated IF. It can be seen that the signal has four normalized frequencies at 0.08065, 0.129, 0.1855 and 0.2339. The symbol duration corresponds to 68 samples as derived from the minimum time interval in the observed IF. Since the sampling frequency is 8000 Hz, the signal's subcarrier frequencies are then 645.2 Hz, 1032 Hz, 1484 Hz and 1871.2 Hz, with symbol duration equal to 8.5 ms.

Fig. 4.21(b) displays the time representation of the second real-life MFSK signal that is sampled at 8 KHz. From the estimated IF laws depicted in Fig. 4.22(b), we find that $M = 8$ and the estimated subcarrier frequencies are: 720, 800, 940, 960, 980, 1064, 1120 and 1140 Hz while the symbol duration is 250 ms corresponding to 2000 samples.

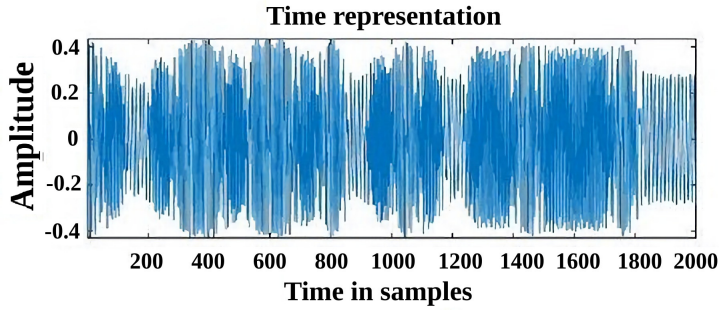

(a)

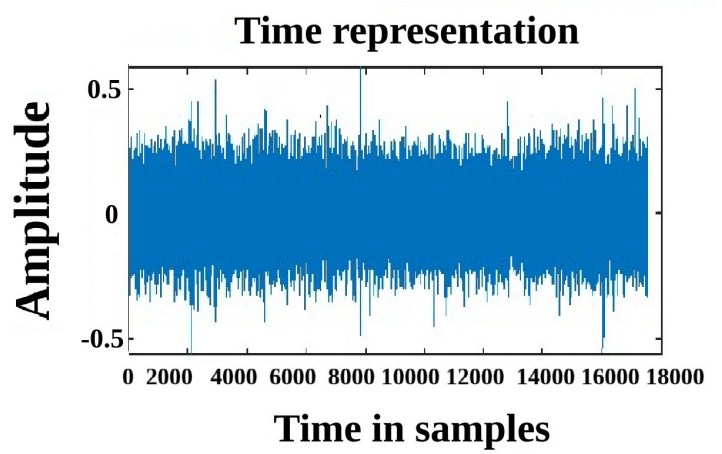

(b)

FIG. 4.21: Time representation of a real-life MFSK radio communications signals in the HF band. (a) The first signal and (b) The second signal.

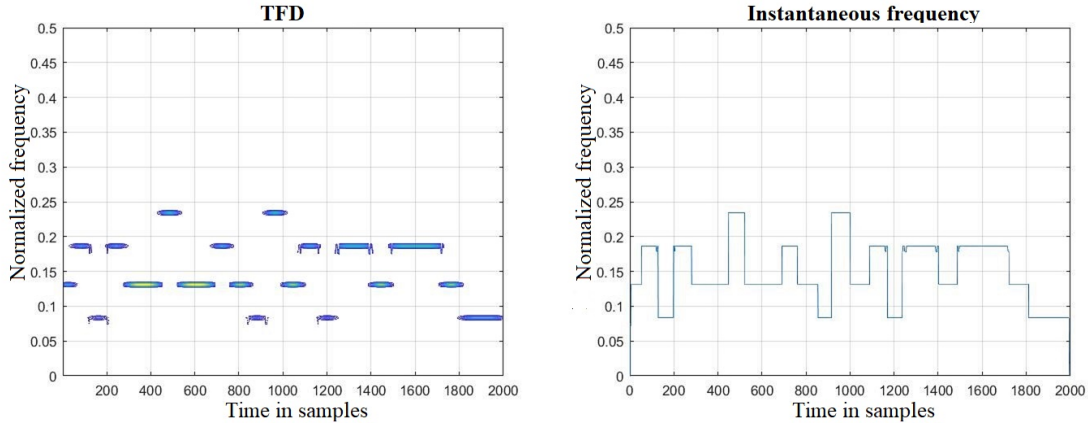

(a)

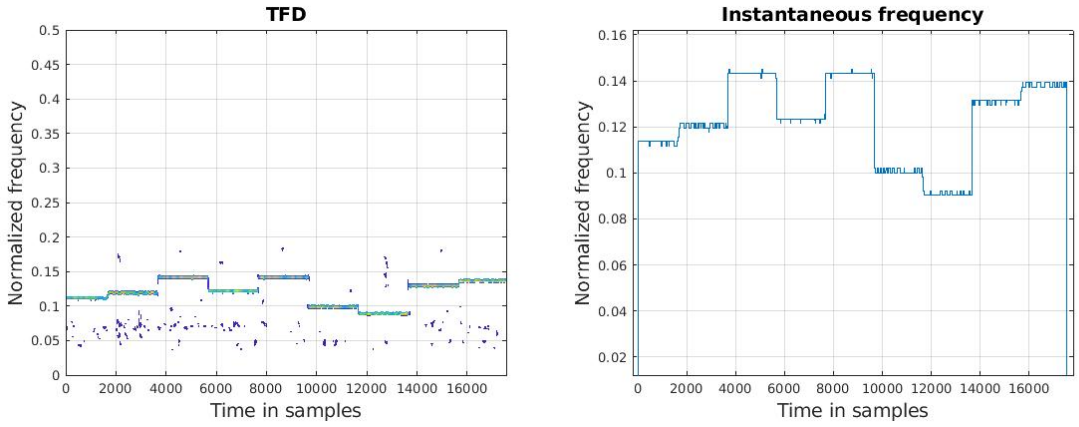

(b)

FIG. 4.22: Time-frequency characteristics of real-life MFSK radio communications signals in the HF band: EPCBD (left) and IF estimate (right). (a) The first signal and (b) The second signal.

4.7 Application to radar signals

Radar is widely used both in military and non-military applications such as tracking missiles, aircraft, flight control systems, and geological observations, just to name a few. By definition, to avoid detection or interception by non-cooperative intercept receiver, low probability of intercept (LPI) radars utilize special emitted waveform that has been specifically designed for this propose [99]. A time-varying signal such as LPI radar signals, the spectral description of which depends on time, is best analyzed with time-frequency representations. In this framework, two commonly used radar signal types are analyzed using the enhanced PCBD. The two signals are: Continuous wave linear frequency modulation (CW-LFM) and pulse linear FM (PLFM). These signals can be categorized as LPI radar signal waveforms [99] with their parameters recorded in Table 4.8. The actual radar signals parameters,

however, may vary according to the applications. The time representation

TABLE 4.8: Signal parameters of the two investigated radar signals. Pulse repetition period (T), pulse width (T_p), highest frequency (f_{max}) and bandwidth BW [100].

Signals	PLFM	CW-LFM
Time parameters	$T = 2$ s	$T = 0.4$ ms
	$T_p = 1$ s	$T_p = 0.2$ ms
Frequency parameters	$f_{max} = 10$ Hz	$f_{max} = 10$ MHz
	$BW = 10$ Hz	$BW = 10$ MHz

of a two-pulses PLFM signal is depicted in Fig. 4.23(a). The EPCBD and IF estimate are shown in Fig. 4.23(b). The estimated parametres are: Pulse repetition period ($T = 2.04$ s), pulse width ($T_p = 1.02$ s), maximum frequency ($f_{max} = 10.2$ Hz) and bandwidth ($BW = 9.5$ Hz). The estimation error is about 2% for f_{max}, 5% for BW, 2% for T and 1% for T_p.

Fig. 4.24 shows the TF analysis results related to a two-pulses CW-LFM signal. The maximum frequency of the signal is estimated at 9.9 MHz while the occupied bandwidth is about 9.7 MHz. The pulse width and the pulse repetition period are found to be equal to $T_p = 199.7\mu$s and $T = 399.4\mu$s, respectively. The estimation error is 1% for f_{max}, 3% for BW and only 0.15% for the time parameters. As a conclusion, the performed enhancement allows providing precise information about both when and at what frequencies a radar signal event occurs.

Typically, electronic support deals with a non-cooperative environment where prior knowledge of the true signal characteristics are unknown. In this context, the obtained results show that the enhanced KCSD provide an accurate low-complexity analysis tool for a broad class of signals. The estimated parameters can be used for further complex tasks such as features extraction and classification even at bad transmission conditions (low SNR values and high interference).

4.8 Computational complexity

The complexity of each enhanced KCSD is measured in terms of the processing time. The enhanced TFD computational complexity is estimated by running Monte-Carlo simulations where the processing time is evaluated through generation of the TFDs of 400 test signals and repeating the process 20 times. The test signals are multicomponent nonstationary signals with linear and nonlinear components. The sampling frequency is set to 1 Hz, the time duration is $T = 256$ sec while the number of components is randomly chosen from 1 to 4. The time supports of components are also arbitrary selected within the interval]0,255]. Table 4.9 presents the average processing time of each enhanced TFD including: (1) the TFD computation

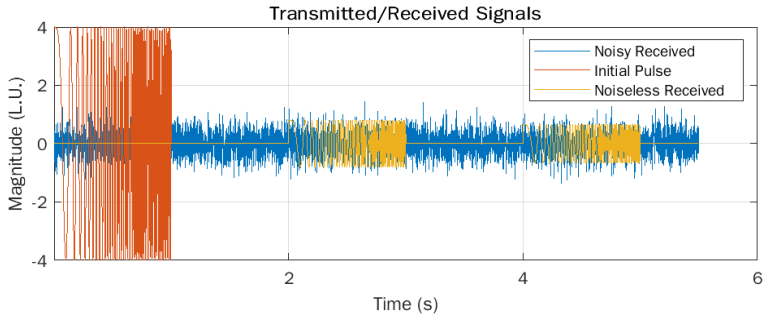

(a)

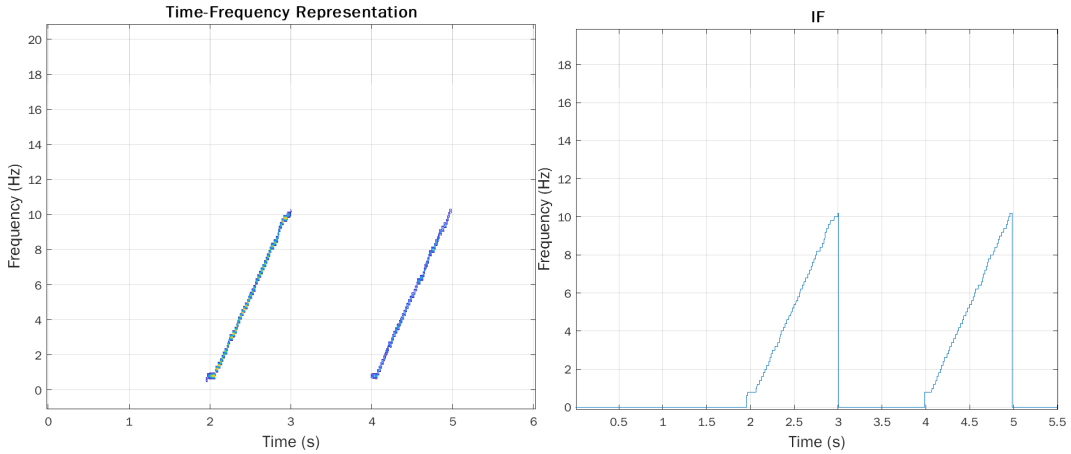

(b)

FIG. 4.23: Time and TF characteristics of a two-pulses PLFM signal at 20 dB. a) Time representation and b) EPCBD (left) and estimated IF (right).

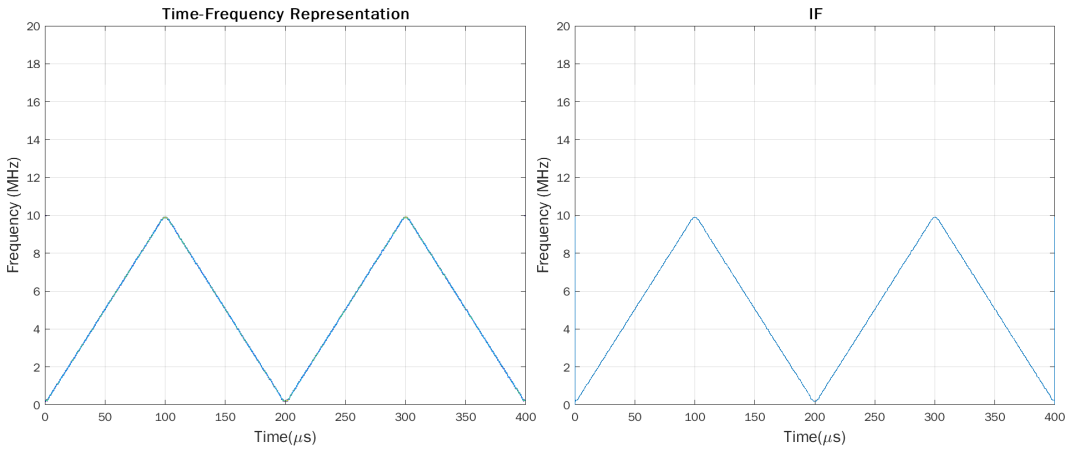

FIG. 4.24: EPCBD (left) and IF estimate (right) of a two-pulses CW-LFM signal at 15 dB.

and optimization and (2) the proposed image-based post-processing. This table shows that the enhanced SCBD is the most computationally demanding technique while the CBD and the PCBD are comparable in terms of the

required processing time. On the other hand, we see that the proposed post-processing is of very low numerical complexity and does not depend on the input TFD that is simply considered as an image of a fixed dimension.

TABLE 4.9: Computational time (s) required by the proposed method estimated from MC simulations (CPU Intel Core 15-6200U, 2.3 GHZ).

KCSD	Optimized TFD (OKCSD)	Image-based post-processing	EKCSD
CBD	0.4006 ± 0.0023	0.0121 ± 0.00057	0.4127
SCBD	5.0183 ± 0.0234	0.0083 ± 0.00039	5.0266
PCBD	0.4575 ± 0.0026	0.0105 ± 0.00051	0.4680

4.9 Conclusion

This chapter shows that, by considering the resulting TFD diagrams as images, it is possible to enhance readability and so improve both concentration and interfering terms suppression of the original representations. This is done through the use of convenient image processing tools. Within this framework, we have proposed a new method that is applied to the optimized time-lag KCS-based TFDs. The image-based post-processing employs two-dimensional Wiener filter, automatic binarization and morphological image processing in enhancing the original CBD, SCBD and PCBD distributions. Several experimental tests on synthetic and real-life signals were performed in order to extract the exact time-frequency characteristics. Supported by objective assessments, the obtained results show that the enhanced KCSDs provide significant improvement in concentration and time-frequency localization compared to the original distributions. Furthermore, a great reduction of crossterms, sidelobes and noise levels is observed even in the hard case of very closely spaced linear chirps embedded in noise. For practical applications, we have considered the use of the enhanced PCBD in estimating the instantaneous frequency of MFSK signals. The PCBD is preferred because its numerical complexity is the lowest and its tuning is the simplest and the fastest since the time-lag PCB requires the selection of a single integer parameter rather than a real smoothing parameter as for the CB and SCB kernels. We have seen that the enhanced PCBD produces precise time–frequency representations of MFSK signals at different modulation levels, leading to accurate extraction of the IF laws from the TFR's peaks even at low SNRs. In addition, comparisons were made with SPWVD and a selection of the most powerful reassignment TFRs in terms of the mainlobe width and the achieved IF estimation MSE, respectively. The numerical results show that the proposed method outperforms the other investigated representations. Furthermore, the enhanced PCBD allows precise determination of other important parameters such as subcarrier frequencies and symbol duration. Thus, the

modulation parameters of unknown MFSK signals can be directly estimated from the IF laws and be used as input to a classifier network. Another extremely interesting property of the KCSDs is that the powerful smoothing is performed without any need of external windows. This is the most constraining drawback when using the best-performing reassignment TFRs discussed in this paper namely, the RPWVD, the RSPWVD, the RSP, the RPPD, the RSD and the RPMHD as well as the SPWVD. In this case, it is very hard to set the optimal window's type and length from the large offered choices.

The main drawback of our proposed approach is that its overall performance depends on the goodness of the original TFD that must be optimized and also on the automatic thresholding. Hence, if the kernel's smoothing parameter and the threshold are not properly selected, discontinuities of the signal components will appear. These limitations were particularly seen when the noise power is greater than the signal power (negative SNRs). Concerning optimization of TFDs, the used concentration-based measures are not computationally demanding especially with the current speed of processors while the automatic threshold selection can be bettered using other thresholding techniques. Another drawback appears at small energies of TFDs that result on suppression of some signal details that are considered as background. This situation is particularly observed at the beginning and the end of the components frequency events. This loss affects the accurate estimation of the IF laws at these two regions and can be recovered by simple interpolation.

Note that our approach is generic and may be applied to any TFR. Future work will include the application of the proposed method to enhance results related to EEG signals' classification [64, 101], motors' diagnosis [91], frequency-hopping spread spectrum (FHSS) systems and blind source separation.

Chapter 5

Conclusions

In essence, the main message and findings of this manuscript are as follows. The time-domain representation tends to obscure information about frequency because it assumes that the two variables t and f are mutually exclusive. In Fourier analysis, all temporal aspects (beginning, end, duration of an event), although present in the phase, become unreadable in the spectrum. This requires us to use other mixed time-frequency representations which make it possible to locate them or to locate these variations over time. Characteristic features of non-stationary signals in the T-F domain can be enhanced by using data-dependent representations. In particular, linear-based time-frequency representations such as STFT and CWT are powerful tools for time-varying signals analysis. The main drawback of these methods is their limited resolution. Indeed, it is impossible to have perfect localization both in time and frequency. For a monocomponent linear frequency modulation signal, the WVD is optimal for energy concentration about the instantaneous frequency. It has received much attention because of its mathematical properties. However, if a signal has nonlinear frequency modulation and/or multiple components, the WVD suffers from cross-terms and/or inner artifacts, respectively; in either case, quadratic time-frequency distribution should be preferred over the WVD in most applications. The design of QTFDs is best undertaken by designing the desired kernel smoother in the ambiguity domain and using FTs to see the effects in the TF domain. To be a useful tool for practical applications, QTFDs are expected to resolve auto-terms components while reflecting the components IF laws through the peaks of their dominant ridges in the (t, f) plane. Each QTFD can be written as a smoothed version of the WVD using a specific time-lag kernel filter. Kernels are designed as low-pass filters in the ambiguity domain to eliminate and suppress the cross-terms. Some members of the quadratic TFDs are pseudo Wigner-Ville distribution (PWVD), smooth-pseudo Wigner-Ville distribution (SPWVD), B-distribution (BD), Choi-Williams distribution (CWD), and modified B-distribution (MBD).

One of the best-designed kernels is the compact support kernel family. Applied to time-frequency signal analysis (TFSA), the compact support kernels namely, the CB, the SCB, and the PCB are simply tuned using a single parameter that controls the bandwidth extent. This tuning is much finer using the CB and the SCB kernels since C is a real positive number. The induced

distributions referred to as the CBD, the SCBD, and the PCBD show a great ability for cross-term suppression while preserving the signal proper components yielding to a notable improvement of TF resolution and energy concentration of the auto terms. Unfortunately, although QTFDs that are smoothed versions of the Wigner-Ville distribution (WVD) reduce interferences, concentration performance is systematically degraded. The situation becomes more complex for noisy multicomponent signals with closely spaced components and may even have spectral overlapping or crossings when frequency varies over time, while visual inspection remains difficult and very subjective. Therefore, excellent time-frequency readability is in need to pinpoint the frequency contents and time variability of such signals. To address this issue, many post-processing enhancement methods were introduced. The reassignment method was one of the early introduced. It performs well only when the signal components are not too close in the time-frequency domain and the signal is embedded in a moderate level of noise. To solve problems invertible of the reassigned TFRs, posterior processing schemes such as the synchrosqueezing method were proposed. Initially introduced for the continuous wavelet transform and later extended to the STFT. In the context of readability enhancement, many other methods were proposed such that multi-taper, S-method, time–frequency image de-blurring, and de-noising. These methods are useful tools for readability enhancement. However, many of these methods cannot overcome the fundamental concentration limit of TFRs in dealing with closely spaced signal components. To improve time-frequency readability of Kernel with Compact Support (KCS)-based TFDs, a new approach was proposed that employs a two-dimensional filter, automatic binarization, and morphological image processing. The obtained results show that the enhanced representations provide considerable improvement in concentration compared to the original representations. On the other hand, the enhanced TFRs using image post-processing provide clean plots compared to their original versions. In addition, advanced procedures for the design and enhancement of high-resolution distributions can allow the extraction of more precise information defining discriminatory features such as the instantaneous frequency.

Bibliography

[1] B. Boashash. *Time-frequency signal analysis and processing: a comprehensive reference*. Second. United Kingdom: Elsevier, 2015.

[2] G. D IDIER. *Modélisation et diagnostic de la machine asynchrone en présence dedéfaillances . Thèse de doctorat, Université Henry Poincaré, Nancy, France. 2004*. Second. United Kingdom: Elsevier, 2015.

[3] *Kumar, P., and Foufoula-Georgiou, E. (1997), Wavelet analysis for geophysical applications, Rev. Geophys., 35(4), 385– 412, doi:10.1029/97RG00427.*

[4] Daubechies I. *Ten lectures on wavelets. Philadelphia, PA: Society for Industrial and Applied Mathematics.* 1992.

[5] Azita Mayeli. *Discrete and Continuous Wavelet Transformations on the Heisenberg Group*. 2005.

[6] J. B. Tary et al. *Spectral estimation-What is new? What is next?Rev. Geophys. 52, 723–749. (doi:10.1002/2014RG000461).*

[7] O. Rioul and M. Vetterli. *Wavelets and signal processing. IEEE. Signal. Process. Mag. 8, 14–38. (doi:10.1109/79.91217).*

[8] Ren Huorong, Ren An, and Li Zhiwu. "A new strategy for the suppression of cross-terms in pseudo Wigner–Ville distribution". In: (). DOI: 10.1007/s11760-014-0713-9.

[9] Savino M. Andria G. "Interpolated smoothed pseudo Wigner–Ville distribution for accurate spectrum analysis. IEEE Trans.Instrum. Meas". In: 5 (1997), pp. 292 –294. DOI: 10.1007/s11760-014-0713-9.

[10] Stanislav Pikula and Petr Benes. "A new method for interference reduction in the smoothed pseudo wigner-ville distribution". In: *International Journal on Smart Sensing and Intelligent Systems* 7.5 (2014).

[11] Mohammad Al-Sa'd, Boualem Boashash, and Moncef Gabbouj. "Design of an Optimal Piece-Wise Spline Wigner-Ville Distribution for TFD Performance Evaluation and Comparison". In: *IEEE Transactions on Signal Processing* 69 (2021), pp. 3963–3976. DOI: 10.1109/TSP.2021.3089291.

[12] *Zeng, Xiaodong (2018). [ACM Press the 2018 10th International Conference - Brisbane, Australia (2018.02.24-2018.02.26)] Proceedings of the 2018 10th International Conference on Computer and Automation Engineering - ICCAE 2018 - Automatic Modulation Classification of Radar Signals Using the Pseudo Margenau-Hill Distribution. 120–123. doi:10.1145/3192975.3192977.*

[13] F. Auger N. Ouwayed A. Belaıd. “formuaire estimation de l’inclinaison d’un document arabe manuscrit numérisé par analyse temps-fréquence des histogrammes de projection”. In: 5 (1997), pp. 292 –294. DOI: 10.1007/s11760-014-0713-9.

[14] Andrzej Katunin. “Application of time-frequency distributions in diagnostic signal processing problems: a case study”. In: *Diagnostyka* 17.2 (2016), pp. 95–103.

[15] M. G. Tsipouras and D. I. Fotiadis. “Time and time-frequency methods dm the analysis of heart rate variability”. In: *Scattering and Biomedical Engineering: Modeling and Applications: Corfu, Greece, 18-19 October 2001* (2002), p. 433.

[16] Francois Auger et al. “Time-frequency toolbox”. In: *CNRS France-Rice University* 46 (1996).

[17] P.A. Karthick and S. Ramakrishnan. “Surface electromyography based muscle fatigue progression analysis using modified B distribution time–frequency features”. In: (2016). DOI: https://doi.org/10.1016/j.bspc.2015.12.007.

[18] *Barkat, B. Boashash, B. A high-resolution quadratic time-frequency distribution for multicomponent signals analysis. IEEE Trans. Signal Proc. 2001, 49, 2232–2239*. Vol. 5. 1997, pp. 292 –294. DOI: 10.1007/s11760-014-0713-9.

[19] *Barkat, B. Boashash, Introduction to Time-Frequency Signal Analysis*. Vol. 5. 1997, pp. 292 –294. DOI: 10.1007/s11760-014-0713-9.

[20] *Z.M. Hussain, B. Boashash, The T-class of time–frequency distributions: time-only kernels with amplitude estimation, J. Franklin Inst. 343 (2006) 661–675*. Vol. 5. 1997, pp. 292 –294. DOI: 10.1007/s11760-014-0713-9.

[21] Kunihiko Kodera, Claude de Villedary, and Roger Gendrin. “A new method for the numerical analysis of nonstationary signals”. In: *Physics of the Earth and Planetary Interiors* (1976).

[22] F. Auger and P. Flandrin. “Improving the readability of time-frequency and time-scale representations by the reassignment method”. In: *IEEE Transactions on Signal Processing* 43.5 (1995), pp. 1068–1089. DOI: 10.1109/78.382394.

[23] Patrick Flandrin, François Auger, and Eric Chassande-Mottin. “Time-frequency reassignment: from principles to algorithms”. In: 2002.

[24] F. Auger, E. Chassande-Mottin, and P. Flandrin. “Making reassignment adjustable: The Levenberg-Marquardt approach”. In: *2012 IEEE International Conference on Acoustics, Speech and Signal Processing (ICASSP)*. 2012, pp. 3889–3892. DOI: 10.1109/ICASSP.2012.6288767.

[25] Francois Auger et al. "Time-Frequency Reassignment and Synchrosqueezing: An Overview". In: *IEEE Signal Processing Magazine* 30.6 (2013), pp. 32–41. DOI: 10.1109/MSP.2013.2265316.

[26] Sean A. Fulop and Kelly Fitz. "Algorithms for computing the time-corrected instantaneous frequency (reassigned) spectrogram, with applications". In: *The Journal of the Acoustical Society of America* 119.1 (2006), pp. 360–371. DOI: 10.1121/1.2133000.

[27] Andrzej Katunin. "Application of time-frequency distributions in diagnostic signal processing problems: A case study". In: *Diagnostyka* 17.2 (2016), pp. 95–103.

[28] Said Agounad et al. "Investigation into the bistatic evolution of the acoustic scattering from a cylindrical shell using time-frequency analysis". In: *Journal of Sound and Vibration* 412 (2018), pp. 148–165. ISSN: 0022-460X. DOI: https://doi.org/10.1016/j.jsv.2017.09.036. URL: https://www.sciencedirect.com/science/article/pii/S0022460X17306995.

[29] Aassif E.H. Khandouch Y. et al. Agounad S. "Signal Processing Techniques of Circumferential Waves for Characterization of Bilaminated Cylindrical Shells." In: (2020).

[30] Gaurav Thakur et al. "The Synchrosqueezing algorithm for time-varying spectral analysis: Robustness properties and new paleoclimate applications". In: *Signal Processing* 93.5 (2013), pp. 1079–1094. ISSN: 0165-1684. DOI: https://doi.org/10.1016/j.sigpro.2012.11.029.

[31] Ingrid Daubechies, Jianfeng Lu, and Hau-Tieng Wu. "Synchrosqueezed wavelet transforms: An empirical mode decomposition-like tool". In: *Applied and Computational Harmonic Analysis* 30.2 (2011), pp. 243–261. ISSN: 1063-5203. DOI: https://doi.org/10.1016/j.acha.2010.08.002.

[32] Hau-Tieng Wu, Patrick Flandrin, and Ingrid Daubechies. "One or Two frequencies? The Synchrosqueezing Answers". In: *Adv. Data Sci. Adapt. Anal.* 3 (2011), pp. 29–39.

[33] Dong He et al. "Time-reassigned synchrosqueezing transform: The algorithm and its applications in mechanical signal processing". In: *Mechanical Systems and Signal Processing* 117 (2019), pp. 255–279.

[34] Sylvain Meignen, Thomas Oberlin, and Stephen McLaughlin. "A New Algorithm for Multicomponent Signals Analysis Based on SynchroSqueezing: With an Application to Signal Sampling and Denoising". In: *IEEE Transactions on Signal Processing* 60.11 (2012), pp. 5787–5798. DOI: 10.1109/TSP.2012.2212891.

[35] Yanjie Guo, Zuowei Fang, and Xuefeng Chen. "A new improved Synchrosqueezing Transform based on adaptive short time fourier transform". In: *2014 IEEE Far East Forum on Nondestructive Evaluation/Testing*. 2014, pp. 329–334. DOI: 10.1109/FENDT.2014.6928290.

[36] Gaurav Singh Thakur and Hau-Tieng Wu. "Synchrosqueezing-Based Recovery of Instantaneous Frequency from Nonuniform Samples". In: *SIAM J. Math. Anal.* 43 (2011), pp. 2078–2095.

[37] Duong-Hung Pham and Sylvain Meignen. "High-Order Synchrosqueezing Transform for Multicomponent Signals Analysis—With an Application to Gravitational-Wave Signal". In: *IEEE Transactions on Signal Processing* 65.12 (2017), pp. 3168–3178. DOI: 10.1109/TSP.2017.2686355.

[38] Thomas Oberlin, Sylvain Meignen, and Valérie Perrier. "Second-Order Synchrosqueezing Transform or Invertible Reassignment? Towards Ideal Time-Frequency Representations". In: *IEEE Transactions on Signal Processing* 63.5 (2015), pp. 1335–1344. DOI: 10.1109/TSP.2015.2391077.

[39] H.-T. Wu. *Adaptive Analysis of Complex Data Sets, PhD thesis, Princeton, NJ, USA, 2011.*

[40] D. Zhang and Z Feng. "Enhancement of time-frequency post-processing readability for nonstationary signal analysis of rotating machinery: Principle and validation. Mechanical Systems and Signal Processing". In: *Applied and Computational Harmonic Analysis* ().

[41] Sylvain Meignen, Thomas Oberlin, and Duong-Hung Pham. "Synchrosqueezing transforms: From low- to high-frequency modulations and perspectives". In: *Comptes Rendus Physique* 20.5 (2019). Fourier and the science of today / Fourier et la science d'aujourd'hui, pp. 449–460. ISSN: 1631-0705. DOI: https://doi.org/10.1016/j.crhy.2019.07.001. URL: https://www.sciencedirect.com/science/article/pii/S163107051930101X.

[42] David Thomson. "Multitaper analysis of nonstationary and nonlinear time series data". In: *Nonlinear and Nonstationary Signal Processing* (Jan. 2000).

[43] Jun Xiao and Patrick Flandrin. "Multitaper time-frequency reassignment". In: *2006 14th European Signal Processing Conference*. 2006, pp. 1–5.

[44] L. Rankine, M. Mesbah, and B. Boashash. "IF estimation for multicomponent signals using image processing techniques in the time-frequency domain". In: *Signal Process.* 87 (2007), 1234–1250.

[45] L. Tao and Y. Shao-Quan. "Improvement on joint time-frequency representation with application of image processing technique". In: *Proc. ICCIMA 5th Int. Conf. on Comput. Intell. and Multimedia Applications (ICCIMA' 2003)*. Xi'an, China, 2003, 243–248.

[46] S. Gomez, V. Naranjo, and R. Miralles. "Removing interference components in time-frequency representations using morphological operators". In: *J. of Vis. Commun. and Image Representation* 22 (2011), 401–410.

[47] M. Sun et al. "Elimination of cross-components of the discrete pseudo Wigner distribution via image processing". In: *Int. Conf. on Acoustics, Speech, and Signal Process.* Vol. 4. 1989, pp. 2231–2233. DOI: 10.1109/ICASSP.1989.266908.

[48] Boualem Boashash, Nabeel Ali Khan, and Taoufik Ben-Jabeur. "Time–frequency features for pattern recognition using high-resolution TFDs: A tutorial review". In: *Digital Signal Processing* 40 (2015), pp. 1–30. ISSN: 1051-2004. DOI: https://doi.org/10.1016/j.dsp.2014.12.015. URL: https://www.sciencedirect.com/science/article/pii/S1051200414003571.

[49] D. J. Nelson et al. "Denoising using time-frequency and image processing methods". In: *Proc. SPIE 3807 Adv. Signal Process. Algorithms, Architectures, and Implementations IX*. 1999.

[50] S. Parolai. "Denoising of seismograms using the S-transform". In: *Bull. of the Seismological Soc. of Amer.* 99 (2009), 226–234.

[51] L. Boubchir and B. Boashash. "Wavelet denoising based on the MAP estimation using the BKF prior with application to images and EEG signals". In: *IEEE Trans. on Signal Process.* 61 (2013), pp. 1880–1894.

[52] E. Sejdić and J. Jiang. "Pattern recognition in time-frequency domain: selective regional correlation and its applications". In: ed. by Peng-Yeng Yin. Vienna, Austria: IntechOpen, 2008. Chap. 27, 613–626.

[53] G. Yu and J. Slotine. "Audio classification from time-frequency texture". In: *IEEE Int. Conf. on Acoust., Speech and Signal Process. (ICASSP 2009)*. 2009, pp. 1677–1680. DOI: 10.1109/ICASSP.2009.4959924.

[54] Alireza Shamlou, Mohammad Reza Feyzi, and Vahid Behjat. "Winding deformation classification in a power transformer based on the time-frequency image of frequency response analysis using Hilbert-Huang transform and evidence theory". In: *International Journal of Electrical Power and Energy Systems* 129 (2021), p. 106854. ISSN: 0142-0615.

[55] B. Leprette and N. Martin. "Extraction of pertinent subsets from time-frequency representations for detection and recognition purposes". In: *Signal Process.* 82 (2002), 229–238. DOI: 10.1016/S0165-1684(01)00181-5.

[56] A. Loza, N. Canagarajah, and D. Bull. "Region feature-based segmentation of time-frequency images". In: *11th Int. Work shop on Syst., Signals and Image Process. (IWSSIP 2004)*. 2004, 375–378.

[57] F. Millioz, J. Huillery, and N. Martin. "Short time Fourier transform probability distribution for time-frequency segmentation". In: *IEEE Int. Conf. on Acoust., Speech and Signal Process. (ICASSP' 2006)*. Toulouse, France, 2006, 448–451.

[58] F. Millioz and N. Martin. "Reassignment vector field for time-frequency segmentation". In: *Proc. of Int. Congr. on Sound and Vib. (ICSV14)* (2007).

[59] C. Tantibundhit, F. Pernkopf, and G. Kubin. "Joint time-frequency segmentation algorithm for transient speech decomposition and speech enhancement". In: *IEEE Trans. on Audio, Speech, and Lang. Process.* 18 (2010), 1417–1428.

[60] P. Flandrin. *Time-frequency/time-scale analysis*. First. Vol. 10. San Diego, USA: Elsevier, 1993.

[61] T. D. Popescu. "Time-frequency analysis: By Leon Cohen". In: *Control Eng. Pract.* 5 (1997), pp. 292 –294. DOI: https://doi.org/10.1016/S0967-0661(97)90028-9.

[62] R. L. Allen and D. W. Mills. *Signal analysis: time, frequency, scale and structure*. IEEE-Wiley, 2004.

[63] M. Abed and A. Belouchrani. "Performance analysis and computational cost evaluation of high-resolution time-frequency distributions derived from compact support time-lag kernels". In: *Digit. Signal Process.* 78 (2018), pp. 1–19.

[64] A. Larbi, M. Abed, and A. Ouahabi. "Newborn's EEG seizure detection using compact kernel time-frequency distributions and Doppler-lag domain features". In: *Proc. IEEE Sixth Int. Conf. on Image and Signal Process. and their Applications (ISPA '2019)*. Mostaganem, Algeria, 2019.

[65] L. Remaki and M. Cheriet. "KCS-new kernel family with compact support in scale space: formulation and impact". In: *IEEE Trans. on Image Process.* 9 (2000), pp. 970–981. DOI: 10.1109/83.846240.

[66] M. Abed et al. "Compact support kernels based time-frequency distributions: performance evaluation". In: *Proc. IEEE 36th Int. Conf. on Acoust., Speech and Signal Process. (ICASSP '2011)*. Prague, Czech Republic, 2011, pp. 4180–4183.

[67] M. Abed et al. "Time-frequency distributions based on compact support kernels: properties and performance evaluation". In: *IEEE Trans. on Signal Process.* 60.6 (2012), 2814–2827.

[68] E. Sejdić, I. Djurović, and J. Jiang. "A window width optimized S-transform". In: *J. Adv. Signal Process.* (2007).

[69] A. Moukadem et al. "A robust heart sounds segmentation module based on S-transform". In: *Biomed. Signal Process. and Control* 8.3 (2013), 273–281.

[70] Z. Zidelmal et al. "S-transform based on compact support kernel". In: *Digit. Signal Process.* 62 (2017), pp. 137–149.

[71] D. L. Jones and T. W. Parks. "A high resolution data-adaptive time-frequency representation". In: *Proc. IEEE Int. Conf. on Acoust., Speech and Signal Process. (ICASSP '1990)*. Detroit, 1990, 2127–2135.

[72] P. Flandrin, R. G. Baraniuk, and O. Michel. "Time-frequency complexity and information". In: *Proc. IEEE Int. Conf. on Acoust., Speech and Signal Process. (ICASSP '1994)*. Adelaide, Australia, 1994, 329–332.

[73] L. Stankovic. "A measure of some time-frequency distributions concentration". In: *Signal Process.* 81.3 (2001), 621–631.

[74] B. Boashash and V. Sucic. "Resolution measure criteria for the objective assessment of the performance of quadratic time-frequency distributions". In: *IEEE Trans. on Signal Process.* 51.5 (2003), 1253–1263.

[75] Isabella Reinhold and Maria Sandsten. "Optimal time–frequency distributions using a novel signal adaptive method for automatic component detection". In: *Signal Processing* 133 (2017), pp. 250–259. ISSN: 0165-1684. DOI: https://doi.org/10.1016/j.sigpro.2016.11.028. URL: https://www.sciencedirect.com/science/article/pii/S0165168416303425.

[76] Ezzedine Braiek, Ali Meghoufel, and Mohamed Cheriet. "SKCS - New kernel family with compact support". In: vol. 2. Jan. 2004, pp. 1181–1184. DOI: 10.1109/ICIP.2004.1419515.

[77] Saeid Saryazdi and Mohamed Cheriet. "PKCS: A Polynomial Kernel Family With Compact Support for Scale- Space Image Processing". In: *IEEE transactions on image processing : a publication of the IEEE Signal Processing Society* 16 (Oct. 2007), pp. 2299–308. DOI: 10.1109/TIP.2007.903900.

[78] Imran Shafi et al. "Quantitative evaluation of concentrated time-frequency distributions". In: *2009 17th European Signal Processing Conference*. IEEE. 2009, pp. 1176–1180.

[79] Muhammad Ajab et al. "A new form of Gabor Wigner Transform by adaptive thresholding in Gabor Transform and Wigner Distribution and the power of signal synthesis techniques to enhance the strengths of GWT". In: *Metrology and Measurement Systems* 20.1 (2013), pp. 99–106.

[80] Imran Shafi et al. "High-resolution time-frequency methods' performance analysis". In: *EURASIP Journal on Advances in Signal Processing* 2010 (2010), pp. 1–7.

[81] Nicoletta Saulig. "Entropy Based Information Measures in the Joint Time-Frequency Plane". In: (2010).

[82] N. Mahmood, M. Razif, and M. Gany. "Comparison between median, unsharp and Wiener filter and its effect on ultra sound stomach tissue image segmentation for Pyloric Stenosis". In: *Int. J. of Appl. Sci. and Technol.* 1.5 (2011), pp. 218–258.

[83] Owlnet.rice.edu. *Wiener filtering*. 2021. URL: https://www.owlnet.rice.edu/~elec539/Projects99/BACH/proj2/wiener.html.

[84] S. E. Umbaugh. *Digital image processing and analysis: Applications with MATLAB and CVIPtools*. 3rd. 2017.

[85] N. Otsu. "A threshold selection method from gray-level histograms". In: *IEEE Trans. on Syst., Man, and Cybernetics* 9.1 (1979), 62–66.

[86] Derek Bradley and Gerhard Roth. "Adaptive Thresholding using the Integral Image". In: *J. Graphics Tools* 12 (Jan. 2007), pp. 13–21. DOI: 10.1080/2151237X.2007.10129236.

[87] S. Donya, C. Eswaran, and A. Mueen. "An automated blood vessel segmentation algorithm using histogram equalization and automatic threshold selection". In: *J. of Digit. Imag.* 24 (2011), 564–572.

[88] Mathworks.com. *Remove small objects from binary image - MATLAB bwareaopen*. 2020. URL: https://www.mathworks.com/help/images/ref/bwareaopen.html.

[89] L. Lam, S. W. Lee, and C. Y. Suen. "Thinning methodologies a comprehensive survey". In: *IEEE Trans. on Pattern Anal. and Mach. Intell.* 14.9 (1992), pp. 869–885.

[90] T. Vipin. *Understanding digital image processing*. 1st. 2018.

[91] S. Seninete et al. "On the use of high-resolution time-frequency distribution based on a polynomial compact support kernel for fault detection in a two-level inverter". In: *Periodica Polytechnica Electrical Engineering and Computer Science* 64.4 (2020), pp. 352–365. DOI: https://doi.org/10.3311/PPee.15469.

[92] DSP group of Rice University. *Bat echolocation chirp*. 2009. URL: https://www.ece.rice.edu/dsp/software/bat.shtml.

[93] *The ARRL handbook for radio communications*. Ninety-Fourth. The Amer. Radio Relay League, 2017. URL: http://www.arrl.org/.

[94] G. Al-Juboori et al. "A Comparison of OFDM and GFDM-Based MFSK Modulation Schemes for Robust IoT Applications". In: *IEEE 85th Veh. Technol. Conf. (VTC Spring)*. 2017, pp. 1–5. DOI: 10.1109/VTCSpring.2017.8108191.

[95] Q. N.Nguyen et al. "A 77 GHz waveform generator with MFSK modulation for automotive radar applications". In: *IEEE Int. Wireless Symp. (IWS 2015)*. 2015, pp. 1–4. DOI: 10.1109/IEEE-IWS.2015.7164548.

[96] Y. K. Song, Y. Liu, and Z. L. Song. "The design and implementation of automotive radar system based on MFSK waveform". In: *E3S Web Conf.* 38 (2018), p. 01049.

[97] D. Garrood. "Applications of the Acoustic Communications System". In: *OCEANS 81*. 1981, pp. 67–71. DOI: 10.1109/OCEANS.1981.1151697.

[98] T. Xu and L. Xu. *Digital underwater acoustic communications*. Academic Press, 2017.

[99] G. RAVIPRAKASH, P. TRIPATHI, and B. RAVI. "Generation of Low Probability of Intercept Signals". In: *International Journal of Scientific Engineering and Technology* 2 (2013), pp. 835–839.

[100] Mathworks.com. *Radar Pulse Compression*. 2021. URL: https://www.mathworks.com/help/phased/ref/phased.linearfmwaveform-system-object.html.

[101] Kaveh Samiee, Peter Kovacs, and Moncef Gabbouj. "Epileptic seizure classification of EEG time-series using rational discrete short-time Fourier transform". In: *IEEE transactions on Biomedical Engineering* 62.2 (2014), pp. 541–552.